SISSA  ISAS

SCUOLA INTERNAZIONALE SUPERIORE DI STUDI AVANZATI
INTERNATIONAL SCHOOL FOR ADVANCED STUDIES

High Energy Emission in Relativistic Jets of AGN: Theory predictions and gamma-ray view

Thesis submitted for the degree of
Doctor Philosophiae

PhD Thesis of:
Giulia Migliori

Supervisors:
Prof. Annalisa Celotti
Dr. Aneta Siemiginowska
Dr. Paola Grandi

October 2010

Contents

Abstract

The last decade has been a golden epoch for the observations of extragalactic jets. The extension of the observational window from the radio through infrared and optical up to the high energy band has provided us with a wealth of new data. The study of the jets by modeling their spectral energy distribution has become a very effective approach. Multiband observations are determinant to constrain the model parameters and probe the radiative environment where the jets form and expand. The broadband fitting allows us to infer the main physical parameters of the emitting plasma and to consequently estimate the total jet kinetic power.

In this thesis a simple leptonic synchrotron and inverse Compton model is adopted and generalized by taking into account the main local and external radiative fields which can act as seed photons. The model is used to derive constraints on the jet contribution to the total high energy emission in compact radio sources. These are supposed to be the young counterparts of the giant radio sources. Unveiling the origin of their high energy emission is crucial to understand their subsequent evolution and the nature of the feedback mechanism with the intergalactic medium. First, we discuss the modeled broadband emission of jets in low and high power young radio sources observed at increasing viewing angles. The role of the seed photons is investigated for different jet velocities and linear sizes. We then test the model on the spectral energy distribution of the compact quasar 3C 186.

The presence of a velocity structure internal to the jet appears to be a crucial requirement to ensure its radiative relevance at the high energies. The internal structure of the jet is the subject of a dedicated study carried out on the FR I radio galaxy NGC 6251. The two radiative models used to describe its non-thermal broadband nuclear emission return back two deeply different pictures: a heavy and slow jet for the synchrotron self Compton model while a light but highly dissipative one for the structured jet model (spine-layer).

1 Introduction

1.1 Active Galactic Nuclei

The term Active Galactic Nuclei (AGN) refers to the existence of energetic phenomena in the nuclei or the central regions of galaxies which cannot be related to the normal star activity. AGN luminosities range from about 10^{40} erg s^{-1} for some nearby galaxies to distant quasars emitting more than 10^{47} erg s^{-1} . The power per unit logarithmic frequency interval is constant over several decades in frequency, from the radio band to X-rays, with some quasars being bright even at gamma-ray energies.

Their emission is spatially unresolved except in the radio band, where there is sometimes evidence for collimated outflows at relativistic speeds. The power output of AGN is often variable on time scales of years and sometimes on time scales of days, hours, or even minutes. X-ray observations revealed that the strong variability phenomena characterizing their optical/UV emission can be even more extreme at these energies. A flaring activity able to produce changes in luminosity by factors of $\sim$2 can be detected on time scales of the order of days to minutes (Mushotzky et al., 1993).

Causality implies that an object that varies rapidly in time t must be smaller than the light-crossing time of the object, ct (where c is the speed of light) and thus must be spatially small; if not, the variation would appear smoothed. High luminosities imply high masses such that gravity can contrast radiation pressure, which would

otherwise blow the object apart. AGN therefore must be of very high mass density. Mass estimates for the central object powering the AGN range from $\sim 10^5$ $M_\odot$ to $\sim 10^{9.5}$ $M_\odot$. These arguments led to the currently accepted conclusion that an extremely compact object, such as a Super-massive Black Hole (SMBH), might be responsible for the AGN activity (Rees, 1984).

The so called "AGN paradigm" states that the SMBH located at the dynamical center of the host galaxy is surrounded by orbiting gas, possibly in the form of a disk (e.g. Shakura and Sunyaev, 1973), which spirals inwards as a consequence of angular momentum loss, releasing gravitational energy. This mechanism is highly efficient (i.e. $\sim 6\% - 30\%$ depending on the spin of the black hole; Yu and Tremaine, 2002; Reynolds and Nowak, 2003; Fabian, 2006) and can account, together with the secondary processes triggered by it, for the overall AGN energy budget.

1.2 AGN Classification

AGN terminology is rather complex. The distinctions between different types of AGN often reflect more historical differences in how objects were discovered or initially classified than real physical differences.

In the context of "unified models" (Antonucci, 1993; Urry and Padovani, 1995) the same processes are at work in all AGN and the main differences in their observed properties are rather ascribed to orientation effects. However, there is a fundamental division in the classification scheme based on the radio properties of the AGN which might be related to a fundamental physical difference. A large majority of AGN fall into one of the categories of radio-loud objects or radio-quiet objects. About 10 per cent of AGN are radio loud with the remaining being radio quiet.

Radio loud (RL) nuclei emit collimated, relativistic jets of plasma which feed energy and high-energy particles into an extended halo or lobe (Rees, 1971; Begelman et al., 1984). Both the jets and halo are observed to be sources of continuum radio emission, presumably due to synchrotron emission from relativistic electrons in the jet/halo plasma.

Radio quiet (RQ) AGN do not show large (i.e. kilo-parsec) scale collimated jets, although small, parsec-scale jets have been reported in some radio-quiet nuclei (Ulvestad, 2003; Middelberg et al., 2004, and references therein) . Bi-polar radio emission, typically with an extent less than 0.5 kpc, is often seen and attributed to an outflow from the AGN. A possible explanation is that radio-quiet

AGN also have outflows, which may only be poorly collimated and non relativistic (Falcke and Biermann, 1995).
A more rigorous definition of radio loudness is based on the radio properties of the PG sample of quasars studied by Kellermann et al. (1989). The radio loudness parameter is defined as the ratio between the radio emission at 5 GHz and the flux in the B band of the core ($R = F_5/F_B$). According to this parameter a galaxy is radio loud if $R \geqslant 10$, vice versa is classified as radio quiet. In the following, we will refer only to the class of radio loud AGN.

1.2.1 Radio Loud Classes

The appearance of a radio loud AGN observed in the radio band is not unique. Differences are related to the individual object, the inclination at which is observed and the frequency of observation. However, some main structural radio components can be identified (Figure 1.1):

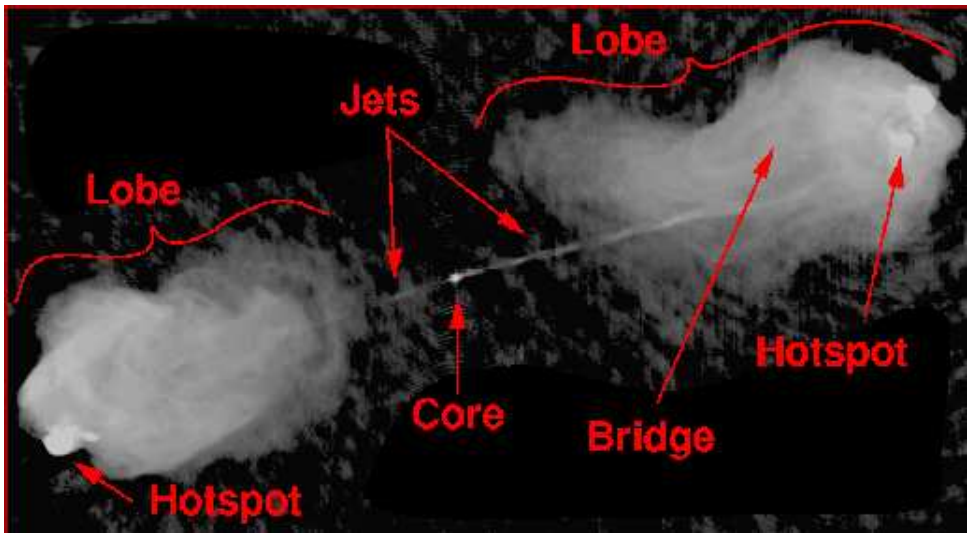

Figure 1.1 Radio image of a radio galaxy showing the main features (Carilli)

- the core: in the radio band, the cores of radio galaxies have a compact flat spectrum (spectral index $\alpha \sim 0$). Since the linear sizes of the cores are small, they are considered the region of jet launching.

- the jets: are the elongated components which emerge from the core and point to the edge of the extended structures. Their brightness can be very faint and even elusive, as also display regions of intense luminosity (knots). Their path can be straight or even strongly bent.

- the lobes: are the extended structures inflated in the intergalactic medium by the jet plasma. Their extension varies from kiloparsec to megaparsec scales. They are particularly visible in the radio band, characterized by a steep spectral index ($\alpha_{radio} \geqslant 0.6$). However, they can produce even high energy emission. X-ray radiation is related to inverse Compton emission of the cosmic microwave background photons. Astonishingly, γ-ray emission associated to the radio lobes of Cen A has been detected by *Fermi* -LAT (Fermi-LAT Collaboration Abdo, 2010).

- the hot-spots: are bright compact regions at the end of the jets, with a typical linear size of ~ 1 kpc. They are interpreted as the site of strong shocks where the jet meets the intergalactic medium and starts filling the lobe.

Additional definitions related to jet and lobe substructures comprise the presence of *plumes* and *bridges*.

Historically, the main division of RL AGNN is based on the radio morphology of the extended structured (Fanaroff and Riley, 1974):

- FR I radio galaxies (Figure 1.2, *right panel*) : have broadening jets feeding diffuse lobes or plumes. The overall jet emission is of high contrast against diffuse radio structures. Also, jets have usually their peak of brightness in a region near to the nucleus and then progressively fade. Hot spots are dim or missing, for this reason, FR I are also indicated as "edge-darkened" sources.

- FR II radio galaxies (Figure 1.2, *left panel*): have narrower jets which are sometimes faint with respect to the surrounding lobe plasma and terminates with bright hot spots ("edge-brightened" morphology). The jets are often knotty and appear embedded in the lobe plasma.

FR II sources are in average more luminous than FR I. A luminosity of $P(408MHz) \sim 10^{25}$ W Hz^{-1} is usually adopted as dividing limit. Differences are also related to the environment (Zirbel, 1997) and the host galaxy luminosities (Govoni et al., 2000). FR I are predominantly found in high density clusters while FR II belong to more isolated fields (Prestage and Peacock, 1988). On average, FR II host galaxies are less luminous with respect to those of FR I, even though selection effects cannot be excluded (Scarpa and Urry, 2001). From the spectral point of view, the optical spectra of FR I sources are characterized by weaker emission lines than in FR II.

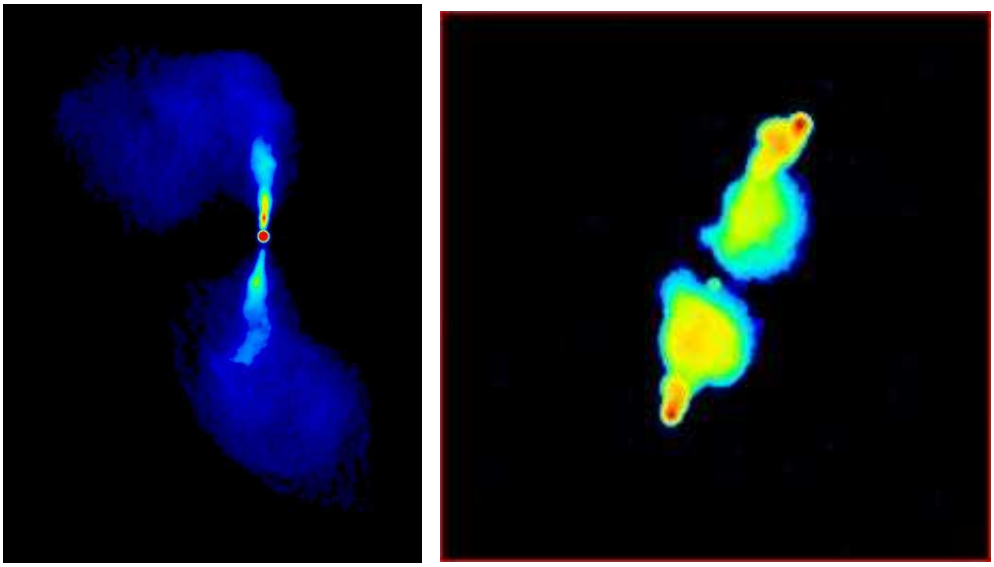

Figure 1.2 *Left Panel:* the FR I radio galaxy 3C 272.1 (Laing and Bridle, 1987). *Right Panel:* the FR II radio galaxy 3C 184.1 (Leahy and Perley, 1991).

However, the classification is often not so sharp and objects with hybrid features have been found (Capetti et al., 1995).

Mainstream explanations for the FR I/FR II separation consider either the jet structure or the physics of the central accretion process.
The morphology could originate from the interactions of the jet with its environment. In FR I the jet is believed to born relativistic but slow down to subrelativistic velocities over kpc scales (Laing et al., 1999) from entrainment of interstellar medium. On the opposite, FR II jet seem to remain supersonic with respect to the external gas out to the hot spots.
The alternative scenario invokes different accretion modes onto the SMBH. In the centre of FR II, there would be a standard Shakura Sunyaev accretion disk (Shakura and Sunyaev, 1973), which has high accretion rates and is radiatively efficient. A disk with a low accretion rate and/or low radiative efficiency (as the Advection Dominated Accretion Flow, ADAF Narayan, 2002, for a review) would reside in the core of FR I sources. Related to this, we mention the possibility that a radio source could evolve from a class to the other after a change in its accretion properties.

1.2.2 Unification Scheme for RL Sources

Much of the effort in AGN research has been focused on explaining the differences between classes of AGN with a small number of simple physical principles. The resulting schematic models are known as 'unified schemes' (US) (Antonucci, 1993; Urry and Padovani, 1995). Two key-parameters should be responsible for the observed anisotropic emission: 1- obscuration of the nuclear region by obscuring matter schematized as a toroidal structure coplanar with the accretion disk; 2- the presence of jets leaving from the black hole poles.

Beside this, RL AGN should have a unique structure. A super-massive black hole ($M_{BH} \sim 10^6 - 10^9$ $M_\odot$) is located at the centre of the AGN. The matter accreted on the BH emits UV up to soft-X-ray radiation. Hard X-ray emission can be produced via Comptonization of soft disk photons by hot corona of electrons above the inner part of the accretion disk (Liang and Price, 1977; Haardt et al., 1994). Within a radius of $2 - 20 \times 10^{16}$ cm several gas clouds form the so-called Broad Line Region (BLR) emitting broad emission lines in the optical-UV band with typical width of the order of several thousands km s^{-1}. Surrounding the BLR is a dusty torus with inner radius of the order of $\sim 10^{17-18}$ cm. Outside the torus, extended (kpc-scale) gas clouds produce narrow emission lines with width of the order of several hundred km s^{-1}, by which the name of Narrow Line Regions (NLR). Then the radio jets expands up to even Mpc scales.

According to the US of radio loud AGN, torus and jet intervene hiding or boosting the different components (Urry and Padovani, 1995). The torus blocks the direct view of the accretion disk and the BLR when the observer line of sight is perpendicular to the jet axis. In that case the optical spectrum of the galaxy shows only the narrow line emission, by this the classification in Narrow Line Radio Galaxy (NLRG). For sources almost lying along the jet axis the emission is dominated by the non-thermal radiation from the jet, strongly boosted by relativistic effects (section 1.3.5). These are the blazar sources, further divided in flat spectrum radio quasars (FSRQ) and BL Lac, whether strong emission lines ($EW > 5$A) are present or absent respectively. For intermediate viewing angles the jet radiation is progressively less boosted and disk and BLR emission emerge. These objects are referred to as steep spectrum radio quasars (SSRQ) and for lower luminosities as broad line radio galaxies (BLRG).

In this scheme, two divides can be individuated. The first depends on the orientation and is between, roughly, radio galaxies and blazars. The second is between high and low power sources: FR II are unified with quasars (FSRQ and SSRQ) while FR I are thought to be the parent population of BL Lac objects (Urry and Shafer, 1984).
Although US explain many aspects of RL AGN, there are still some open issues. Just to mention two examples, there are observational indications that in FR I and BL Lac sources the torus is not present (Chiaberge et al., 1999). Also, FR I and BL Lac are found in different environments (Zirbel, 1997; Owen et al., 1996), which is at odds with the idea of a unique population observed at different angles.

1.3 Extragalactic Jets

Extragalactic jets are the giant collimated plasma outflows through which the central black hole transfers huge amounts of energy, moment and angular momentum over large distances to the ambient medium (Blandford and Rees, 1974; Rees, 1971; Scheuer, 1974). They provide the principal physical and observational link between the central black holes and their cosmic environments, with a huge span in linear scale from the black hole region ($\sim 10^{-4}$ pc) to the hot spots ($\lesssim 10^{10}$ pc).
The origin and evolution of these amazing structures remains still an enigmatic process after more than 30 years of dedicated studies. Unsolved questions accompany the jet from its obscure formation to its end, through the path revealed by the emitted radiation. Answer to these questions would not only mean unravel the secrets of jets, but also achieve a new insight on the machine which power the jet, the central black hole, and on the evolution of the whole system hosting the jet in its expansion, galaxy and environment. We give a general and qualitative overview of this wide topic and refer to some interesting and exhaustive reviews for a detailed treatment Begelman et al. (1984); Ferrari (1998); Harris and Krawczynski (2006); Worrall (2009).

1.3.1 Formation

The origin of relativistic jets is still an open problem in astrophysics. Two most popular mechanism were proposed by Blandford and Payne (1982); Blandford and Znajek (1977). The first considers launching of an outflow from a magnetized disk, the other

extraction of rotational energy from a spinning black hole through magnetic interaction with a surrounding plasma. The essential difference between the two is the energy reservoir, even though both require the presence of the magnetic field, either as energy reservoir or "ambient".
A major problem of jet formation mechanisms is that they predict a Poynting flux-dominated energy transport by a strongly magnetized plasma, while pc-scale observations seem to point to particle dominated plasma (Celotti and Fabian, 1993). The issue is twofold: the initial formation as a possible magnetic dominated outflow and its conversion to a particle dominated jet.

1.3.2 Expansion and Confinement

Astrophysical jets are characterized by a remarkable stability, clearly visible in the ratio between the jet length and its radius, observed to be of the order of 100. The opening angle is also very small. The jets propagate for very long distances (kpc till even Mpc) maintaining a considerable fraction of the initial velocity and without expanding sideways in a drastic manner. This implies some confinement mechanism which acts transversely. Despite detailed informations about the jet structure and emission properties, the mechanism(s) responsible for the collimation, and the acceleration of the plasma is still unknown. Confinement could be due to the static gas pressure of an external medium (Komissarov, 1994), or induced by the presence of winds emanating from the central accretion disk, or internal, related to the presence of a toroidal magnetic field within and around the jet (Sauty et al., 2002).
In some sources, combined radio and X-ray observations have allowed to measure the internal pressure in jet and compare it with the one of the external X-ray medium. While the X-ray emitting medium seems to be able to control the flow of FR I jets at kpc scales, in the inner regions near to the nucleus the jet appears to be highly over-pressured (Worrall et al., 1995; Laing and Bridle, 2002). More difficult is the evaluation in the case of FR II jets. The uncertainties on the X-ray emission mechanism makes direct comparison of internal and external pressures difficult.

1.3.3 Jet Composition and Powers

Observation of polarized radio and optical emission show that at least part of continuum emission can be ascribed to synchrotron emission from relativistic particles (electron/positrons) gyrating in a magnetic field. However, this is just part of the

jet essence and the bulk of the jet medium remains unobserved and unconstrained. There are evidences that much of the energy of jets, in fact, is not radiated but accumulates in the surrounding medium (McNamara and Nulsen, 2007, for a review). Conversely, the radiative losses undergone by emitting particles along the jet path would preclude the flow of high energy electrons all the way to the end of many jets. Therefore, we have to distinguish between the relativistic particles responsible for radiation and the underlying medium, which seems to carry the bulk of jet power.
Jet plasma must be neutral, on average, to remain collimated. However, this result can be obtained by different combinations. The three candidate scenarios are Poynting flux, leptonic (electron/positron) or hadronic (electron/proton) fluid. Atoyan and Dermer (2003) proposed jets powered by collimated beams of ultrahigh energy neutrons.
Radiation drag and observational constraints on Comptonized radiation by cold electrons and positrons seriously hamper electron and positron jets, at least if formed close to the central black hole (Sikora et al., 1996a,b).
A useful quantity that can furnish some constraints on jet composition is the jet kinetic power, which is estimated considering all the particles, relativistic and thermal, combined with magnetic field and bulk Lorentz factor (Celotti and Fabian, 1993):

$$P_{jet} = \pi R^2 \Gamma^2 \beta c U' \tag{1.1}$$

where R is the jet radius, Γ the bulk Lorentz factor and U' is the total energy density in the jet rest frame, including radiation, magnetic field, relativistic particles and eventually protons. Celotti & Fabian (1993) argued in favor of an electron-proton fluid, by comparing the bulk kinetic energy of the parsec scale jet with the kinetic luminosities on extended scales (Rawlings and Saunders, 1991). For high luminous blazars, the proton component is necessary, otherwise the radiated power would exceed that carried by the jet (see Ghisellini, 2010, and references therein). Allowing for an equal number of protons and electrons, the radiative efficiency of the jet at the blazar scale turns out to be of the order of 1-10%.
It is likely that all three media are important. Jet may change from electromagnetic to leptonic, through electromagnetic dissipation, to hadronic, through matter entrainment along the jet path.

1.3.4 Feedback and Entrainment

There are two major modes for the AGN-environment interaction: one is the radiative (or quasar or wind) mode where it is the radiation from the AGN which couples with the gas, the other is the kinetic (or jet or radio) mode where the jet carries the energy from the black hole and deposits it into the ambient gas, e.g. via shocks.
Jets can push matter away if it happens to lie on their path. The best way, however, for a jet-driven interaction to occur is when the galaxy has a hot halo, either of its own or because it is part of a group or cluster of galaxies. Then the relativistic fluid in the jets can displace the hot gas, creating bubbles either side of the nucleus. A significant fraction of the energy in the jets can then transfer to the hot halo. If this prevents the halo from radiatively cooling to form cold clouds and stars, then the feedback terminates the stellar growth of the host galaxy.
Entrainment can play an important role with for the jet dynamics and composition. Mass entrainment can cause the progressive deceleration observed in FR I radio galaxies (Laing et al., 2003) and can explain the formation of transversal velocity structure, with the outer layer moving slower than the internal spine. FR II jets maintain relativistic velocities and a high degree of collimation until they reach the hot spot. This seems to suggest that they suffer less entrainment than FR I sources (Bicknell, 1995). Entrainment could also account for the hadronic component of the jets. Possible mechanisms causing entrainment include velocity shear and Kelvin-Helmholtz instabilities (Bodo et al., 2003).

1.3.5 Jet structures and Beaming

In most of the cases, jets are not channels of uniform brightness. They rather display sites of enhanced brightness along their path, generally termed as knots. The origin of the knots has not yet been identified unambiguously. We just mention the two most common explanations related either to the occurrence of (oblique or reverse-forward) shocks or to a change in the beaming factor due to a change in the direction of motion of the plasma.
The last argument is based on the transformation of fluxes and luminosities from the co-moving to the observer frame which occurs when the emitting plasma is moving relativistically. These are summarized by the beaming factor, δ:

$$\delta^{-1} = \Gamma(1 - \beta \cos\theta). \tag{1.2}$$

The beaming factor is determined by the viewing angle θ and the jet/knot bulk velocity Γ. Depending on the jet orientation beaming can act as a powerful flux amplifier. Moving from the knot to the observer frame the intrinsic luminosity L' changes by a factor of δ^4. An even modest change in θ can result in large changes of δ. Therefore, depending on the jet orientation beaming can act as a powerful flux amplifier. An even modest change in θ can be reflected in large changes of δ and then of the observed flux.
It is worth noting that this is just a simplified picture. Dermer (1995) has shown that the pattern of the emitted radiation from a moving blob in an external field of seed photons is different with respect to the synchrotron and inverse Compton emission of local photons.

1.3.6 Radiative Mechanisms

The study of the emission mechanisms at work in extragalactic jets have faced a great improvement with the advent of the last generation of X-ray satellites, *Chandra* and *XMM-Newton* in particular. The number of detection in the X-ray has drastically increased. The imaging capabilities of *Chandra* have even allowed spatially resolved studies.
The two main jet radiation processes are synchrotron and inverse Compton emission. The radio band undoubtedly belongs to the synchrotron. The situation in the X-ray band is more complex as synchrotron and IC emission may be both important.

In low luminosity FR I radio sources there are robust observational evidences that the same mechanism determines the X-ray, optical and radio emission. This is valid for the broadband radiation from the non-thermal core (Chiaberge et al., 1999; Capetti et al., 2002; Verdoes Kleijn et al., 2002), but also at larger scales (Worrall et al., 2001). A steep X-ray spectral index ($\alpha_X \geqslant 1$), often larger than the radio index, and the similar radio optical and X-ray morphology are among the arguments supporting the synchrotron origin.
Given the magnetic field intensities usually considered in the jets (10 to 1000 μG) electrons of energies in the range $10^7 < \gamma < 10^8$ are required to obtain the observed X-ray emission. The lifetimes of the most energetic electrons are of the order of years. As a consequence, synchrotron X-ray emission observed in regions distant from the central BH require a mechanism of acceleration in situ. Acceleration in strong magnetohydrodynamic (MHD) shocks by Fermi I mechanism (Bell, 1978;

Blandford and Ostriker, 1978; Kirk and Duffy, 1999, for a review) is commonly assumed. Uncertainties on the efficiency of the process are related to the presence of an intense magnetic field and our ignorance of actual values of the bulk Lorentz factor.

The emission mechanism of the X-ray radiation in jets of FR II radio galaxies and quasar is more debated. A single synchrotron spectrum cannot account for the radio to broadband emission. Unless postulating the presence of more than one electron population, synchrotron emission seems ruled out in most of the cases.
Radio and X-ray observation of FR II knots seem also to disfavor the explanation of Inverse Compton emission of the local synchrotron photons (SSC). In fact, in order to account for the large ratios of X-ray to radio luminosities a strong dominance of the particle energy over the magnetic field one is required in many cases.
Celotti et al. (2001) and Tavecchio et al. (2000) proposed comptonization of CMB photons by electrons in a very fast jet. Relativistic boosting increases the energy density of the CMB photons in the jet frame. The amplification has a quadratic dependence on the jet bulk Lorentz factor (section 2.3, chapter 2). The model successfully explains the observed X-ray emission with a single population of electrons and without requiring significative violation of the minimum energy assumption. The efficiency of the model is given by the high bulk motion of the jet ($\Gamma = 10 - 20$). A possible uncertainty is related to the number of low energy electrons required. The actual shape of the electron energy distribution at the low energy is not sufficiently probed.

2

Modeling jet emission

2.1 Introduction

Extragalactic jets have been observed on many physical scales and they often extend to hundreds of kiloparsec distances from the nucleus. Although radio jets have been known for many years, the observation of their high energy emission is relatively recent. *XMM-Newton* and *Chandra* X-ray Observatories have revealed their significant X-ray emission (Harris and Krawczynski, 2006, for a review). The MeV-GeV band has been explored by space-born instruments, EGRET in particular, while ground-based Cherenkov telescopes, such as H.E.S.S., MAGIC and VERITAS disclosed the so called very high energy band (VHE, 30 GeV-30 TeV). Gamma-ray studies are now experiencing a new boost with the recent launch of Fermi satellite. At the high energies, observations at different wavelengths allow us to probe different regions of the jet and emitting mechanism. The realm of MeV-TeV energies indeed belongs to blazar sources, which are supposed to have a jet aligned along the line of sight. Although the debate is still open, we believe that the γ-ray emission of blazars originates from a region of the jet close to the black hole. Support to this hypothesis comes from the fast variability characteristic of many blazar sources, which points to an emitting region of small dimensions. Unexpectedly, γ-ray emission from few radio galaxies (Steinle et al., 1998; Mukherjee et al., 2002) was also detected by EGRET (onboard of the Compton Gamma Ray observatory). Very recently *Fermi* LAT observations have confirmed EGRET findings and enlarged the

sample to 11 γ-ray detected radio galaxies (Fermi-LAT Collaboration, 2010). Even more challenging has been the association of VHE emission to the near FR I radio galaxy M87 reported by the HEGRA collaboration (Aharonian, 2003) and investigated by VERITAS (Acciari et al., 2010, and references therein).

Understanding physical processes leading to the observed high energy emission can provide important clues to the jet nature and also to the total quasar power. Thanks to the wealth of multiwavelength data at our disposal, modeling of the broadband spectral energy distribution (SED) of jets has become a powerful tool to derive constraints on the relevant physical parameters. These are the energy distribution of the emitting particle, the magnetic field intensity and the bulk motion of the plasma, and as a direct consequence the jet kinetic power.

The broad-band emission of jets in extragalactic radio sources is usually well-reproduced by a two-component model: a low-energy synchrotron spectrum and a high-energy emission due to Compton up-scattering of seed photons off the particle population in the jet.

The origin of the target photons can be local in the jet (synchrotron self Compton, SSC), or external. Cosmic microwave background (CMB) photons are invoked for jets in powerful FR II sources (Celotti et al., 2001; Tavecchio et al., 2000; Sambruna et al., 2004a) and Broad Line Region (BLR) photons for blazars (Sikora et al., 1994; Ghisellini and Madau, 1996). Direct disk emission and infrared (IR) torus photons have been also considered (Dermer and Schlickeiser, 1993; Sikora et al., 2002; Błażejowski et al., 2004).

Alternatively, a class of models propose non-thermal synchrotron seed photons produced by a fast-moving component and Compton-upscattered by relativistic electrons in a slow flow (and vice versa). The necessary condition is the presence of a velocity structure inside the jet itself, perpendicular (decelerating knot model Celotti et al., 2001; Georganopoulos and Kazanas, 2003) or parallel (spine-layer model Chiaberge et al., 2000; Stawarz and Ostrowski, 2002; Ghisellini et al., 2005) to the jet axis.

In this chapter we set the stage for the study of the SED of extragalactic radio jets under different dynamical and environmental conditions. In a simplified yet accurate way, the adopted model accounts for the several local and external contributions to the radiation energy density at different scales. The effects of the relativistic motion of the jet are also considered. We stress that the model does not include the emission directly observed from the blazar component, which is not the purpose of our study. For the model building, we mainly referred to the following

papers: Ghisellini and Madau (1996); Celotti et al. (2001); Ghisellini et al. (2005); Ghisellini and Tavecchio (2009).

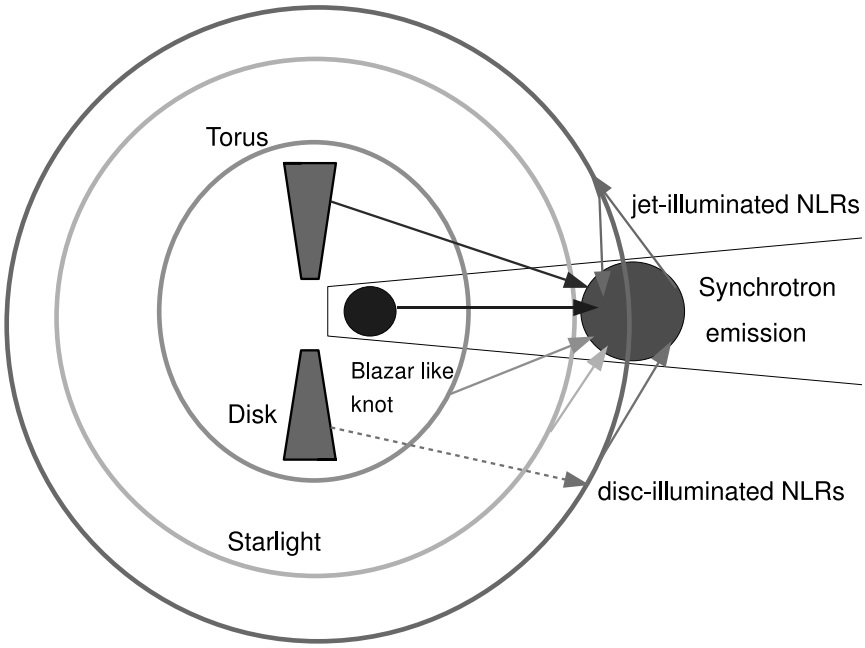

Figure 2.1 A sketch illustrating the geometrical representation assumed for accretion disk, torus, galactic core and NLR. For sake of simplicity, disk and jet illuminated NLR are coincident. The biggest solid sphere is the emitting plasma region while the smallest one stands for the blazar-like region. The arrows show the schematic path of the photons.

2.2 Model setup

We assume that the bulk of the energy dissipation in extragalactic jets occurs in knots. Hereafter we will refer without distinction to jet or knot emission.
In the comoving frame of the radiating knot, particles are injected with relativistic energies and cool over the radiation produced by the knot itself via synchrotron emission, by matter in the accretion disk around the supermassive black hole and by scattering photons coming from nuclear, galactic regions. The model assumes a simplified geometry of the jet, nuclear and galactic structure, schematically shown in Figure 2.1.

The knot is spherical with radius R and located at a height z_d from the jet apex. It is moving with velocity βc and bulk Lorentz factor Γ. The accretion disk emits uniformly within a radius R_{disk}. Matter in torus and NRL clouds

is assumed to be distributed on a spherical thickless surface of radius R_i, with $i = torus, NLR$. We decide to neglect the Broad Line Region contribution and substitute it with the NLR one. The BLR emission is relevant on small scales ($\lesssim 10^{17}$ cm, Ghisellini and Madau, 1996) and has been widely considered for the case of blazars. Here, we study the emission from a blob located already out of the BLRs. In this case, the disk luminosity is typically dominating over the BLR emission.
Dust in the torus absorbs and emits back the same fraction of disk radiation. Disk illumination takes place also in the NLR clouds but in minor measure, because of the larger distance from the central BH and the occluding presence of the torus. In addition, NLR clouds are illuminated and re-emit back a fraction of the continuum produced by the knot itself.
The model accounts for the presence of a radial velocity structure internal to the jet. A second highly relativistic (Γ_{in}) knot, located at the base of the jet, produces an integrated synchrotron luminosity L'_{in} which illuminates the outer knot.
Starlight emission of the host galaxy is limited to the galactic core contribution. As for the torus and NLR, we assume that all the emission comes from a a sphere of radius r_{star}. Finally, cosmic microwave background photons are also considered.

2.3 Radiative fields

The model is designed to reproduce the jet emission at different scales spanning from pc to kpc. The energy densities of the seed photons is estimated in the emitting knot reference frame as a function of its position z_d[1].
The energy density of the local synchrotron photons produced by the knot itself is:

$$U'_r = \frac{L'_r}{V} t_{esc} = \frac{3L'_r}{4\pi R^3} \frac{3R}{4c} = \frac{9L'_r}{16\pi R^2 c}; \tag{2.1}$$

with L'_r and V intrinsic synchrotron luminosity and volume of the spherical knot, and $t_{esc} = 3R/(4c)$ average time needed to a typical photon to leave the source.

Thermal fields

Nuclear and galactic structures are considered to be point-like once the knot has moved out of the structure itself. For $z_d \geqslant R_i$ ($i = disk, torus, NLR,$), the energy

[1] Primed energy densities U'_i refer to the knot reference frame while primed luminosities L'_i always to the intrinsic luminosity.

densities are calculated by means of:

$$U'_i = \frac{L'_i}{4\pi z_d^2 c\Gamma^2}. \tag{2.2}$$

where L'_i are the correspondent intrinsic luminosities.

Disk emission – The accretion disk luminosity is emitted by a region of radius about $10^{15} - 10^{16}$ cm. This is smaller than the scales we are going to probe ($\geqslant 1$ pc). For this reason U_{disk} is always estimated using Equation (2.2).

Torus, disk illuminated NLR – The same geometry but different fractions of disk radiation are assumed for these two components. The equations for the energy densities $U'_{torus/NLR,disk}$ of the torus and disk-illuminated NLRs within R_i has been derived by Ghisellini and Madau (1996) (but see also Sikora et al., 1994):

$$U'_i = \frac{f_i L'_{disk}\Gamma^2}{4\pi R_i^2 c} \int_{-1}^{\mu_i} cos\ \alpha(1 - \beta cos\ \theta)^2 d(cos\ \theta) \tag{2.3}$$

with f_i fraction of disk luminosity reprocessed in the torus/NLR. In the torus/NLR the disk is seen under the angle α:

$$\cos\alpha = \frac{z_d}{R_i}\sin^2\theta - \cos\theta\sqrt{1 - \left(\frac{z_d}{R_i}\right)^2 \sin^2\theta} \tag{2.4}$$

where θ is the angle defined by the velocity vector of the knot and the direction of the incoming (torus/NLR) photon. $\mu_i \equiv cos\ \theta_i$ is given by:

$$\mu_i = \frac{z_d}{\sqrt{R_i^2 + z_d^2}}. \tag{2.5}$$

In the centre of the torus/NLR shell (i.e. $z_d = 0$, and $\cos\alpha = -\cos\theta$) the energy densities become:

$$U'_i \sim \frac{17}{12}\frac{f_i L'_i \Gamma^2}{4\pi R_i^2 c}. \tag{2.6}$$

In the last formula, there is no dependence of the energy density on the knot position inside the sphere. In the exact formula given by Equation (2.3) a weak dependence is present through θ.

The trend of U'_i as a function of z_d can be well described by a plateau with a sudden drop for $z_d > R_i$ caused by relativistic effects, as we change from the extended to

the point-like description (Figures 3.1, 3.2 in Chapter 3).

Starlight and CMB emission – A spherical surface geometry is adopted also to model the starlight diffuse component, which is limited to the galaxy core region. Within the core radius r_{star}, the starlight energy density, U'_{star}, is estimated using Equations (2.3), (2.6) , by substituting the relative starlight luminosity L_{star} and radius r_{star}.
CMB photons provide a uniformly distributed contribution:

$$U'_{CMB} \sim aT^4_{CMB}(1+z)^4\Gamma^2 \tag{2.7}$$

where T_{CMB} is the CMB temperature at redshift zero. The relevance of the CMB photons is decided by the redshift and mostly by the motion of the knot. A knot moving relativistically sees the CMB flux amplified by a factor $\propto \Gamma^2$.

Jet-illuminated NLR emission – NLR clouds behave similarly to the BLR matter, even though on larger scales and dilute fluxes.
Beamed synchrotron emission from the jet knot illuminates a small portion of the NLR. The flux F_{rec} received by each point (P) on the NLR surface may also be intrinsically low, but is highly amplified relative to a comoving observer for a relativistic jet. The level of flux amplification depends on the jet bulk motion (Ghisellini and Madau, 1996):

$$F_{rec} = \frac{1}{\Gamma^4(1-\beta cos\ \alpha)^4}\frac{L'_r}{4\pi r^2(\alpha)} \tag{2.8}$$

where the distance between the knot and P $r(\alpha)$ is given by:

$$r(\alpha) = R_{NLR}\Big[\Big(1-\frac{z_d^2}{R_{NLR}^2}sin^2(\alpha)\Big)^{1/2} - \frac{z_d}{R_{NLR}}cos\alpha\Big]. \tag{2.9}$$

The NLR reprocesses and re-emits an isotropic intensity:

$$I_{NLR,jet} = \frac{f_{NLR,jet}}{4\pi}F_{rec}, \tag{2.10}$$

with $f_{NLR,jet}$ fraction of the jet flux absorbed/re-emitted. As $\theta = 2\pi - \alpha$, the energy density seen by the blob is:

$$U'_{NLR,jet} = \frac{2\pi}{c}\int_{\mu_{NLR}}^{-1} I_{NLR,jet}\Gamma^2(1-\beta\cos\ \theta)^2 d(\cos\ \theta) \quad (2.11)$$

$$= \frac{f_{NLR,jet}L'_r}{8\pi c\Gamma^2}\int_{-\mu_{NLR}}^{1}\frac{(1-\beta\cos\ \alpha)^2}{(1-\beta\cos\ \alpha)^4}\frac{d(\cos\ \alpha)}{r^2(\alpha)}. \quad (2.12)$$

For $\cos\alpha \sim 1$ and $d(\cos\alpha) \sim 1-\beta$, we get the following approximation:

$$U'_{NLR,jet} \sim \frac{4}{\pi}\frac{f_{NLR,jet}L'_r\Gamma^4}{r^2 c} \quad (2.13)$$

where $r = R_{NLR} - z_d$. It is possible to see that $U'_{NLR,jet}$ reaches a maximum when the knot crosses the NLR shell.

Structured jet: emission from a blazar-like knot

The inner knot reproduces the emission from a typical blazar region. The requirement is a large bulk motion Γ_{in}. In the external knot, the flux from this blazar-like component is seen amplified proportionally to the relative motion of the two knots. The energy density U'_{in} is given by (Celotti et al., 2001):

$$U'_{in} \sim \frac{L'_{in}}{4\pi z_d^2 c}\frac{\Gamma_{in}^4}{\Gamma^2}, \quad (2.14)$$

We note that due to beaming effects the total luminosity produced by the inner jet is almost entirely contained in the solid angle defined by $4\pi/\Gamma_{in}^2$.

2.4 Structured jet: spine layer model

In the previous section an axial velocity structure has been considered. This corresponds to the case of a knot which progressively decelerates (see also Georganopoulos and Kazanas, 2003).

High resolution radio data have shown the presence of transverse structures in jets associated with both, low and high power radio galaxies (Giovannini et al., 2001a). The particular *limb brightening* morphology has been interpreted as the evidence for a slower external flow surrounding a fast spine (Swain et al., 1998; Giroletti et al.,

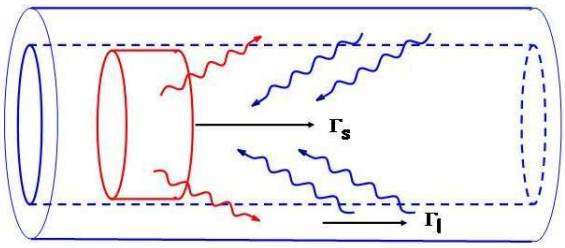

Figure 2.2 Sketch of the spine-layer system.

2004, among others).

The broadband spectral properties of BL Lac objects and FR I radio galaxies give us another argument in support of a jet stratification. Selecting a sample of FR I and BL-Lac sources with the same range of extended luminosity, Chiaberge et al. (2000) have shown that it is difficult to explain the difference in luminosity between the two classes just in terms of beaming effects. A stratified jet can reconcile observations and Unified Scheme. The strongly beamed spine emission dominates in sources oriented closely to the line of sight, while the emission from the slow layer, which is less severely beamed, is detected in misaligned sources. We note that the layer motion has to be still relativistic in order to explain the anisotropic emission observed from the FR I cores (Capetti and Celotti, 1999; Chiaberge et al., 1999; Capetti et al., 2002).

We illustrate here the main aspects of the model and refer to Ghisellini et al. (2005) for a more detailed description.

The layer is a hollow cylinder with external radius R_2, internal radius R and width $\Delta R_l''$. Double primed quantities are in the rest frame of the layer and primed in that of the spine. The spine is a cylinder nested inside the layer (Figure 2.2). Its radius coincides with the internal radius of the layer R, and the width in the spine rest frame is $\Delta R_s'$. The Lorentz factors of the spine and layer are Γ_s and Γ_l, respectively, with $c\beta_s$ and $c\beta_l$ the relative velocities.

The difference of Lorentz factors implies that the radiation emitted by one structure is seen boosted by the other. The factor of amplification Γ' of the radiation energy density with respect to a comoving observer at the same distance from the spine(/layer) is given by:

$$\Gamma' = \Gamma_s \Gamma_l (1 - \beta_s \beta_l) \tag{2.15}$$

Both the regions emit by synchrotron and inverse Compton processes. As a conse-

quence of the boosting, the external photons from the layer (spine) become relevant as seed photons for the scattering process in the spine (layer), in addition to the synchrotron photons produced locally in the spine (layer).
The general outcome is an increase of the inverse Compton flux. The efficiency of this mechanism relies on the bulk Lorentz factors of the spine and layer, as well as on their dimensions. In fact, the energy density of one component in the reference frame of the other is calculated as follows:

- We define $\bar{R} \equiv (R_2 + R)/2$. In the comoving frame of the layer, the radiation energy density in the entire cylinder is assumed to be $U_l'' = L_l''/(\pi \bar{R}^2 c)$. In the frame of the spine, this radiation energy density is assumed to be boosted by a factor $(\Gamma'')^2$, i.e. $U_l' = (\Gamma')^2 U_l''$.
- In the comoving frame of the spine, the radiation energy density within the spine is assumed to be $U_s' = L_s'/(\pi R^2 c)$. In the frame of the layer, this radiation energy density is observed to be boosted by $(\Gamma')^2$, but also diluted (since the layer is larger than the spine) by the factor $\Delta R_s''/\Delta R_l'' = (\Delta R_s''/\Gamma')/\Delta R_l''$.

A further aspect is the anisotropy of the inverse Compton process between the electron of the layer (spine) and the seed photons produced by the spine (layer). The pattern of the emitted radiation in case of external Compton from a moving blob in a bath of seed photons is more beamed than the synchrotron and SSC emission (Dermer, 1995). With respect to the usual pattern $\propto \delta^{3+\alpha}$, the monochromatic intensity of the external Compton follows a pattern $\propto \delta^{4+\alpha}$, where α is the spectral index of the emission. Finding the pattern of the emitted radiation in the spine/layer is not trivial, as also the source of the seed photons is not at rest with respect to the observer. The spine (layer) photons are seen blueshifted in the layer (spine) comoving frame and a further blueshift happens moving to the observer frame. Putting all together, the monochromatic observed intensity of the spine is given by:

$$\begin{aligned} I(\nu) &= I'(\nu')\delta_{s,l}^{4+2\alpha}\delta_l^{3+\alpha} = I'(\nu')\delta_s^{3+\alpha}\left(\frac{\delta_s}{\delta_l}\right)^{1+\alpha} \text{ (EC)} \\ I(\nu) &= I'(\nu')\delta_s^{3+\alpha} \quad \text{(S, SSC)} \end{aligned} \tag{2.16}$$

where $I'(\nu')$ is the monochromatic intrinsic intensity of the spine, and δ_s, δ_l are the beaming factors of the spine and the layer in the observer rest frame, while $\delta_{s,l}$ is defined as the beaming factor of the radiation produced in the spine as observed in

the layer. The external Compton emission (EC) can be compared to the synchrotron (S) and SSC emission. The same transformation with δ_s and δ_l interchanged gives the observed radiation produced by the layer.

With this feedback mechanism, synchrotron and IC luminosities can be produced by a reduced number of relativistic electrons. The same X-ray and γ-ray fluxes can be matched assuming magnetic fields nearer to equipartition assumptions (Ghisellini et al., 2005) with respect to SSC. On the other hand, the power dissipated by the jet is significant compared to its bulk kinetic power. The anisotropy of the emitted luminosity should determine the recoil of the spine and its deceleration (*Compton Rocket* effect).

The process which could determine the formation of a stratified structure is still poorly known. Viscosity and Kelvin-Helmholtz instabilities as entrainment in a relatively dense environment are possible explanations. Also, it is not clear if the jet may be born with a spine-layer structure, or if this is the result of a deceleration which takes place in the first $\sim 10^{17}$ cm (on the basis of the blazar region estimates).

A piece of evidence in support of the spine-layer model would be the detection of flux variability for those radio galaxies observed in the γ-rays. In fact, the spine and the layer must be cospatial. The γ-ray emission of the layer should reflect the flux variation of the spine emission. BL Lac studies allow to locate the spine region at ~ 100 Schwarzschild radii. The flux is expected to vary within timescales of the order of $t_{var} \sim (R/c)/\delta_l$, similar to the variability timescale in blazars.

3

Jets in Young Radio Sources

3.1 Compact and Young Radio Sources

Compact Steep Spectrum (CSS) and Giga-Hertz Peaked Spectrum (GPS) sources are compact ($\leqslant$ 20 kpc) and powerful ($logP_{1.4\,GHz} \geqslant 25$ W Hz^{-1}) radio sources (O'Dea, 1998). They represent 10-40 % of the high frequency radio-selected sources (O'Dea, 1998). Their morphology resembles the classical radio sources and suggests that we are observing not a new class, but rather the young counterparts of the giant radio sources. Support to this hypothesis is given by the determination of both their dynamic (Owsianik and Conway, 1998; Polatidis and Conway, 2003) and spectral (Murgia et al., 1999) ages, turning out to be $\leqslant 10^5$ yrs.

In the alternative scenario, they are radio sources frustrated in their expansion by a dense environmental medium (van Breugel et al., 1984). However, observations have not revealed the presence of such highly dense gas (Gupta et al., 2006), except for few cases.

If the evolutionary hypothesis is correct, compact sources are crucial to address some of the open issues related to the quasar activity, such as the mechanism triggering the activity itself, the physics of the initial phase of the source's evolution and the interactions with the surrounding medium. In particular, X-ray observations of GPS/CSSs can be used to reveal the presence of dense neutral gas and individuate the nature and sites of the most energetic processes.

X-ray detections of GPS/CSSs registered a drastic increase with the advent of

XMM-Newton and *Chandra* observatories. Observational campaigns on GPS and CSS galaxies (Guainazzi et al., 2006; Vink et al., 2006; Tengstrand et al., 2009) and quasars (Siemiginowska et al., 2008b) have been performed for the first time with detection fractions nearly to 100% on the selected subsamples.

Establishing the origin of the high-energy emission is important for two main aspects: 1- to unveil the evolutionary path of extragalactic radio sources, from their birth to their death, through, possibly, recurrent phases of activity; 2- to shed a light on the feedback process between the expanding radio source and its environment, which means to define how much energy the AGN deposit into the intergalactic medium (IGM) and through which mode this preferentially happens.

Unluckily, in the majority of the cases, it is impossible to spatially resolve the X-ray emission in sources that compact. The studies are mainly confined to the analysis of the X-ray spectral properties (presence of an intrinsic absorber, evaluation of X-ray intrinsic luminosities). On the other hand, the low statistics often makes controversial the identification of distinguishing spectral features, as, for instance, the Fe Kα line (with few exceptions, as for Mkn 668, Guainazzi et al., 2004), with the consequence that different models can appear degenerate in the 0.5-10 keV band.

X-ray emission is predicted by theoretical models when the Interstellar Medium (ISM) is swept out by the expanding source and forms a hot (X-ray) emitting cocoon (Reynolds et al., 2001; Bicknell and Sutherland, 2006). Alternatively, it could arise from the central accretion phenomenon, either directly from the hottest inner part of the accretion disk or as soft photons comptonized in the hot corona (Guainazzi et al., 2006; Siemiginowska et al., 2008b; Tengstrand et al., 2009). Consistent non-thermal X-ray flux can be produced in the extended components, namely jets, hot spots and lobes. Recently, Stawarz et al. (2008) proposed a dynamical and radiative model for GPS radio galaxies, which explains the bulk of the high-energy emission as IC emission of nuclear seed photons by relativistic electrons in the compact lobes. Hints on the relevance of the jet contribution come from studies of individual sources, as for the case of 3C 48 (Worrall et al., 2004). Still, the radiative role of the jets during the first stages of the radio source expansion has not been systematically explored.

3.2 Role of the jet in young radio sources

The reliability of the jet hypothesis is here investigated by modeling its spectral energy distribution. In the frame of self-similar expansion of the source, it is plausible to apply to young sources the same radiative mechanisms at work in the jets of their giant counterparts. In our approach, the peculiarity of GPS and CSS sources is rather given by the environment dense of photons in which they are embedded. The radio structures, both jets and lobes, are still relatively compact, therefore local photon fields are expected to be dense. At the same time, the jet is still piercing its way out of the nuclear and galactic environment.
We first use the model outlined in the chapter 2 to analyze how those radiative fields which can act as IC seed photons evolve with the increasing linear size of the source. Then the SED (νL_ν) of a jet with typical linear sizes of GPS and CSS sources are computed assuming a simple leptonic synchrotron and Inverse Compton model.

3.3 Radiative field in GPS/CSS environments

We resume briefly the model presented in Chapter 2: jet emission is summarized by a knot of emitting plasma, located at a height z_d from the central black hole, which is moving with a bulk Lorentz factor Γ. The photon fields we have considered are: local synchrotron photons, external thermal photons from the disk, torus, NLR clouds and the galaxy core, and external synchrotron photons produced by a inner blazar-like knot. All the photon energy densities have been calculated in the reference frame of the outer knot, for two luminosity and bulk motion regimes:

- *Luminosities:* two intrinsic integrated radio luminosities of the knot are assumed $L'_r = 10^{43}$, $L'_r = 10^{45}$ erg s^{-1}. The two luminosity regimes of the jet reflect the general cases of a low and a high power source. For the low-power source, the disk luminosity is equal to $L_{disk} = 10^{44}$ erg s^{-1}, while for the high-power one $L_{disk} = 10^{46}$ erg s^{-1}. The torus reprocesses 10% of the disk luminosity while we assume that the matter in the NLRs receives just 1% of it. The fraction of knot radiation absorbed and re-emitted by the NLRs is fixed at 10%. The internal knot has an unique intrinsic luminosity $L'_{in} = 10^{43}$ erg s^{-1}. The host galaxy contribution is limited to the galaxy core, whose luminosity is equal to $L'_{star} = 10^{45}$ erg s^{-1}. Finally, we use a reference redshift,

$z = 0.1$.

- *Dimensions:* the radius of the emitting knot is proportional to z_d and to the jet semi-aperture angle ψ, so that $R = \psi z_d$ and $\psi = 0.1$. Following Sikora et al. (2002), we set the torus radius using the maximum temperature that dust can survive:

$$R_{torus} \sim \frac{1}{T^2_{torus,max}} \left(\frac{L_{disk}}{4\pi\sigma_{SB}} \right)^{1/2} \sim 1.2 \times 10^{18} \sqrt{L_{disk}/(1 \times 10^{45})} \text{ cm} \quad (3.1)$$

  where we used $T_{torus,max} \sim 1000$ K.
  An HST study of a sample of CSS radio sources (Axon et al., 2000) has found that the largest fraction of the line emission originates from a region within $\leqslant 3$ kpc from the nucleus. The presence of more diffuse and extended ($\sim 10 - 30$ kpc) emission-line component, so called extended NLR, is also reported. Here, we fix the radius of the NLR to 1.5 kpc when the clouds are illuminated by the disk and to 6 kpc when the ionizing continuum comes from the jet. This is mostly aimed at more easily distinguishing the two cases, also with respect to the starlight component.
  The inner knot reproduces a typical compact blazar-like region with radius $R_{in} = 5 \times 10^{16}$ cm.

- *Knot bulk motion:* we consider a knot with a mild relativistic bulk motion ($\Gamma = 1.1$) and highly relativistic knot ($\Gamma = 15$). The bulk motion of the blazar-like knot is fixed equal to $\Gamma_{in} = 15$ (standard blazar values Hovatta et al., 2009). Thus, the $\Gamma = 15$ case corresponds to a jet that has not developed a velocity gradient.

3.3.1 Results

In Figures 3.1 and 3.2, the photon energy densities in the reference frame of the external knot are shown. In the following, we comment the main results first considering the different bulk Lorentz factors and then the luminosities.

Beamed and unbeamed photon fields

When the knot is highly relativistic ($\Gamma = 15$), the relevance of the nuclear photon fields strongly depends on the relative positions of the knot and the source of the

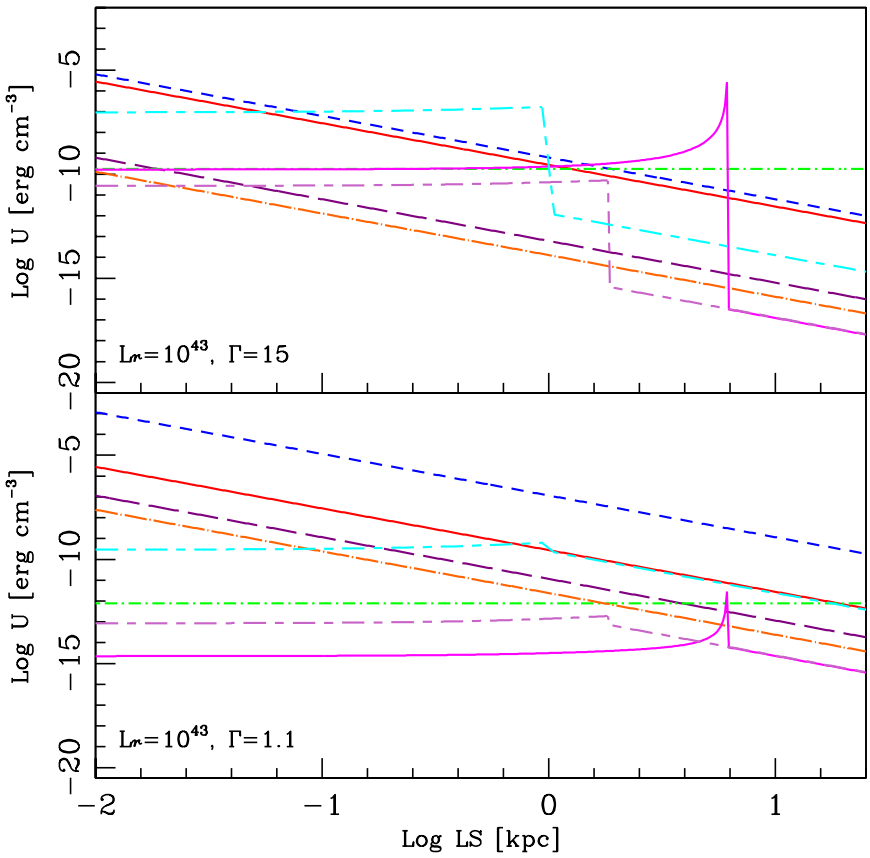

Figure 3.1 Energy densities as a function of z_d for a highly relativistic knot ($\Gamma = 15$) (upper panel) and a mildly relativistic one ($\Gamma = 1.1$). The radiative fields are represented as: U'_r (red solid line), U_{disk} (violet long-dashed), U'_{torus} (orange dot-dashed), $U'_{NLR/disk}$ (pink long-short dashed), $U'_{NLR/jet}$ (magenta solid), U'_{in} (blue dashed), U'_{star} (cyan short-long dashed) and U'_{CMB} (green dot-dashed). The intrinsic radio luminosity of the knot is $L'_r = 10^{43}$ erg s^{-1}, nuclear and starlight luminosities are described in the text.

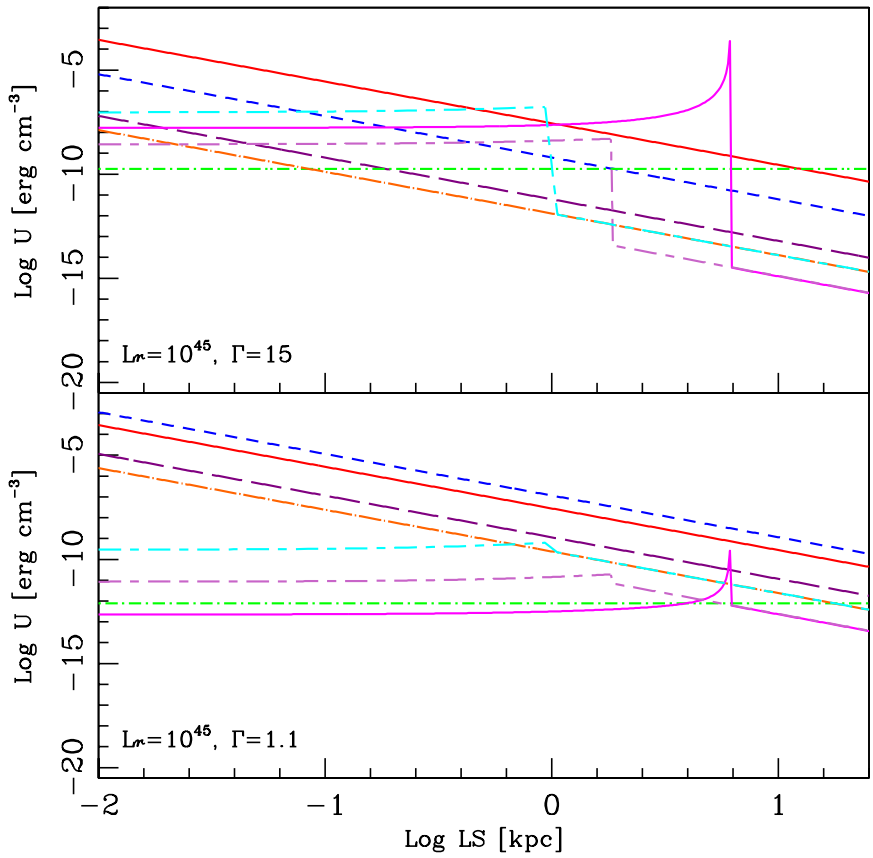

Figure 3.2 Energy densities as a function of z_d for a highly relativistic knot ($\Gamma = 15$) (upper panel) and a mildly relativistic one ($\Gamma = 1.1$). The radiative fields are represented as: U'_r (red solid line), U_{disk} (violet long-dashed), U'_{torus} (orange dot-dashed), $U'_{NLR/disk}$ (pink long-short dashed), $U'_{NLR/jet}$ (magenta solid), U'_{in} (blue dashed), U'_{star} (cyan short-long dashed) and U'_{CMB} (green dot-dashed). The intrinsic radio luminosity of the knot is $L'_r = 10^{45}$ erg s^{-1}, nuclear and starlight luminosities are described in the text.

photons and on the velocity of the knot. As long as the knot is moving inside the nuclear environment, the energy densities of the external nuclear fields are boosted by a factor of $\Gamma^2 = 225$. On the opposite, they suffer a correspondent reduction once the knot has moved out of the nuclear region ($z_d \geqslant R_{NLR/jet} \sim 6$ kpc, including the extended NLRs). The same behavior applies to the starlight energy density at the critical length R_{star} (1 kpc).

The peak in the energy density of the jet-illuminated NLRs (Figures 3.1 and 3.2, *upper panel*) at $z_d = R_{NLR/jet} = 6$ kpc, followed by a a drastic drop, is determined by two factors: 1- the radiation from the blob is strongly beamed in the NLR reference frame with a dependence on the blob-NLR relative distance (see Formulae 2.8, 2.9); 2- we assume that the NLR clouds have a negligible width and they are immediately seen point-like for $z_d > R_{NLR,jet}$.

At large scales ($z_d > 10$ kpc), CMB photons become the relevant field in agreement with the results found for large scale jets (Celotti et al., 2001).

Substancial differences occur for the case of the knot with $\Gamma = 1.1$. The relativistic effects related to the knot motion are attenuated for the external sources of seed photons, because of the low beaming amplification/deamplification factor $\Gamma^2 = 1.21$. We note that this implies a significant increase of the UV-disc energy density with respect to the highly relativistic case. On the opposite, the role of the NLRs, extended NLRs and starlight is significantly reduced in this scenario even when the knot is traveling inside the NLR/galaxy core.

The blazar-like component is proportional to the ratio of the bulk Lorentz factors $U'_{in} \propto \Gamma^4_{in}/\Gamma^2$ (Formula 2.14). The energy density of the external synchrotron is higher in the slow knot by almost two orders of magnitude. The external synchrotron radiation becomes then the dominant photon field at the typical GPS/CSS scales ($z_d \leqslant 30$ kpc).

Low and high luminosity sources

The difference between the two luminosity regimes produces an expected vertical shift of the energy densities of both local (U'_r) and nuclear (disk, torus, NLR) photon energy densities, while starlight, external synchrotron and CMB energy densities are not affected. For $\Gamma = 1.1$ in powerful GPS/CSS sources disk and torus photons might become, together with local and external synchrotron photons, the most intense radiative fields. When the knot is moving with $\Gamma = 15$, interactions between

NLR clouds and the powerful knot produce a considerable amount of target photons, but the overall dominant field is the local synchrotron emission.

3.4 Multiwavelength mapping

A simple power law describes the electron energy distribution (EED):

$$N(\gamma) = K_e \gamma^{-p} \text{ for } \gamma_{min} < \gamma < \gamma_{max}, \tag{3.2}$$

where K_e is the normalization of the distribution (in units of cm^{-3}), γ the particle Lorentz factor, γ_{min} and γ_{max} the limits of the EED, and p the distribution spectral index. Assuming standard values, we set $p = 2.6$, $\gamma_{min} = 10$ and $\gamma_{max} = 10^5$. The EED normalization K_e and magnetic field B have been estimated from the integrated radio powers, under the assumption of equipartition between particles and magnetic field (i.e. $U'_B \sim U'_e$ with U'_B and U'_e magnetic and particle energy densities respectively).

The synchrotron curve is calculated including self absorption effects. We calculated the inverse Compton components (Thomson regime) on the four most intense photon fields at the selected knot distance, luminosity and bulk motion, according to the results of the previous section. Given the chosen parameter values, it is possible to have very similar energy density levels for different fields for some z_d. In this case, either we gave priority to that IC component not already plotted, or we arbitrary chose one.

The thermal emission from the disk (UV), torus (IR), and host galaxy (optical-UV) is modeled as black-body spectra with the appropriate frequency peaks ($\nu_{disk} \sim 2 \times 10^{15}$ Hz, $\nu_{torus} \sim 3 \times 10^{13}$ Hz, $\nu_{star} \sim 2 \times 10^{14}$ Hz). The bolometric intrinsic luminosities are the same of the photon field analysis ($L'_{disk} = 10^{46}$ erg s^{-1}, $L'_{torus} = 10^{45}$ erg s^{-1} in the high power case, and $L'_{disk} = 10^{44}$ erg s^{-1}, $L'_{torus} = 10^{43}$ erg s^{-1} in the low power one) and starlight luminosity is fixed to 10^{45} erg s^{-1}. We also assume a blackbody as a spectral shape of both disk and jet illuminated NLR emission. The NLR peaking frequency is set equal to the $[OIII]$ line frequency ($\nu_{NLR} \sim 6 \times 10^{14}$ Hz).

Synchrotron emission ($L_{in} = 10^{43}$ erg s^{-1}) from the inner knot is modeled assuming a simple power law for the EED, with spectral index $p_{in} = 2.6$ and limits $\gamma_{min,in} \sim$

50 and $\gamma_{max,in} \sim 10^4$.

3.4.1 Results

We computed the knot broadband emission at four distances from the core, 33 pc, 100 pc, 1 kpc and 10 kpc, in the reference frame of an observer at the same redshift of the source ($z = 0.1$). The effects of beaming have been analyzed, considering two extreme jet orientation with respect to the observer, $\theta = 5°, 60°$. The resulting broadband SED are shown in Figures 3.3, 3.4, 3.5.

Unbeamed emission ($\Gamma = 1.1$)

In Figure 3.3, the SED for the mildly relativistic knot with $L_r = 10^{43}$ erg s^{-1} (*Left Panel*) and $L_r = 10^{45}$erg s^{-1} (*Right Panel*) are shown.
For $L_r = 10^{45}$erg s^{-1}, the most relevant inverse Compton components are given by comptonization of the local photons (SSC, red solid line), disk (EC/disk, violet long-dashed), torus (EC/torus, orange dot-dashed) and blazar-like synchrotron (EC/syn, blue short-dashed) photons. Except for a progressive decrease of all IC fluxes with the increasing z_d, there is no significant evolution of the SED with the jet size. We note that in the X-rays the IC/disk emission is observed already in its low-energy tail, while the bulk of its contribution is given at higher energies.
Differently, the low-power knot experiences a partial evolution: U'_{torus} and U'_{star} are still comparable at $z_d = 100$ pc, while at larger scales the starlight component prevails (IC/star, cyan long-short dashed line), as also shown in Figure 3.3. When $z_d = 10$ kpc, IC emission of CMB photons (IC/CMB, green dot-dashed) is one of the candidate contribution.
Finally, we see that the dominant contribution in the high energy band is given by EC/syn. In particular, this appears to be the only viable mechanism able to reproduce the observed X-ray luminosities in GPS/CSS radio sources for a low power jet with a mildly relativistic motion.

Beamed emission ($\Gamma = 15$)

More complexity is added when a beamed component is present. The photon field analysis has shown the role of the relative position, between the emitting plasma and the source of the external seed photons, in determining the energy density in the knot reference frame. This also emerges in the SED under two aspects. First,

the IC component of different seed photons emerges with respect to the unbeamed case: disc and jet illuminated photons (IC/NLR$_{disk,jet}$, pink long-short dashed and magenta solid respectively). Second, there is a partial evolution with z_d of the dominant IC component. For $L_r = 10^{43}$ erg s^{-1}, IC/star rises at $z_d = 1$ kpc, while IC/CMB becomes dominant at $z_d = 10$ kpc. Similar behavior is displayed also by the powerful jet.

In addition, moving from the knot to the observer reference frame, it is necessary to include beaming effects: the flux from a jet oriented near to the line of sight is strongly amplified, conversely for large θ the flux is Doppler hidden. This can be seen comparing the overall SED for $L_r = 10^{43}, 10^{45}$ erg s^{-1} and $\Gamma = 15$ (Figures 3.4,3.5) calculated for $\theta = 5°$ (*Left Panel*) and $\theta = 60°$ (*Right Panel*). The beaming factors for the two angles are $\delta(\Gamma = 15, \theta = 5°) \sim 11$ and $\delta(\Gamma = 15, \theta = 60°) = 0.13$. The bolometric luminosity transforms, from intrinsic to observed, as $L = L'\delta^4$. The result is a jump of about 7 orders of magnitude when the same intrinsic luminosity is observed at the two different inclinations.

The different luminosity regimes clearly imply a difference in the total emitted luminosity. The link between knot (and then the jet) and disk luminosities modifies also the relevance of IC/disk and of those comptonized components depending on the disk luminosity. In particular, we note that for $L_r = 10^{45}$ erg s^{-1}, IC/NLR$_{disk}$ is one of the candidate IC contributions.

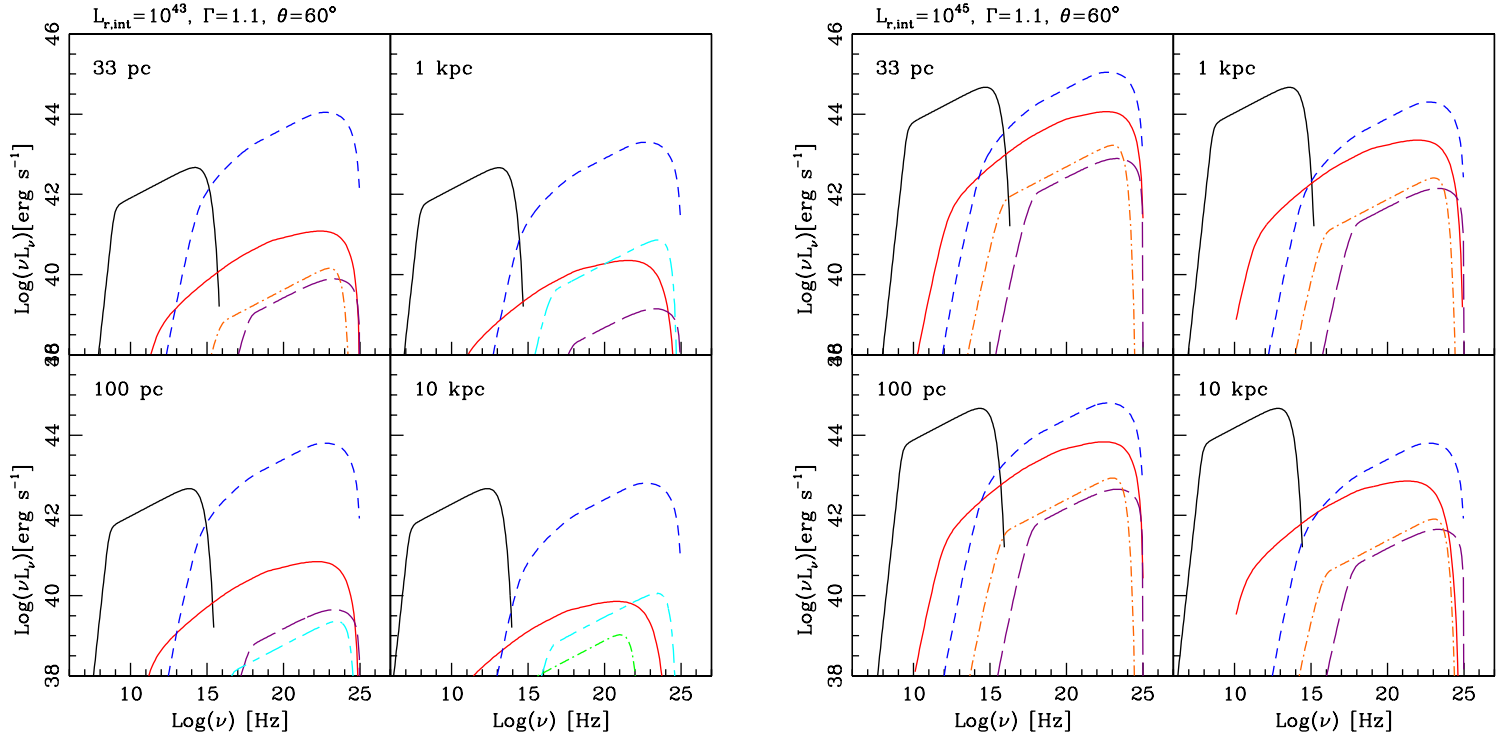

Figure 3.3 Spectral energy distributions for an emitting knot located at 33 pc, 100 pc, 1 kpc, 10 kpc from the core , moving with a bulk Lorentz factor $\Gamma = 1.1$ and observed at a viewing angle $\theta = 60°$. The intrinsic integrated synchrotron power is $L_r = 10^{43}$ erg s^{-1} (*Left Panel*) and $L_r = 10^{45}$ erg s^{-1} (*Right Panel*). The black solid line is the synchrotron emission, red solid one for SSC, blue short-dashed for external Compton off synchrotron photons (EC/syn), violet long-dashed for IC of disk photons (EC/disk), orange dot long- dashed for IC of toris photons (EC/torus), cyan long-short dashed for IC of starlight photons (EC/star), green dot short-dashed for IC of CMB photons (EC/CMB). The EED is a single power law with spectral index $p = 2.6$, with minimum and maximum electron Lorentz factors $\gamma_{min} = 10$ and $\gamma_{max} = 10^5$. Magnetic field B and normalization of the EED have been calculated under assumption of minimum energy.

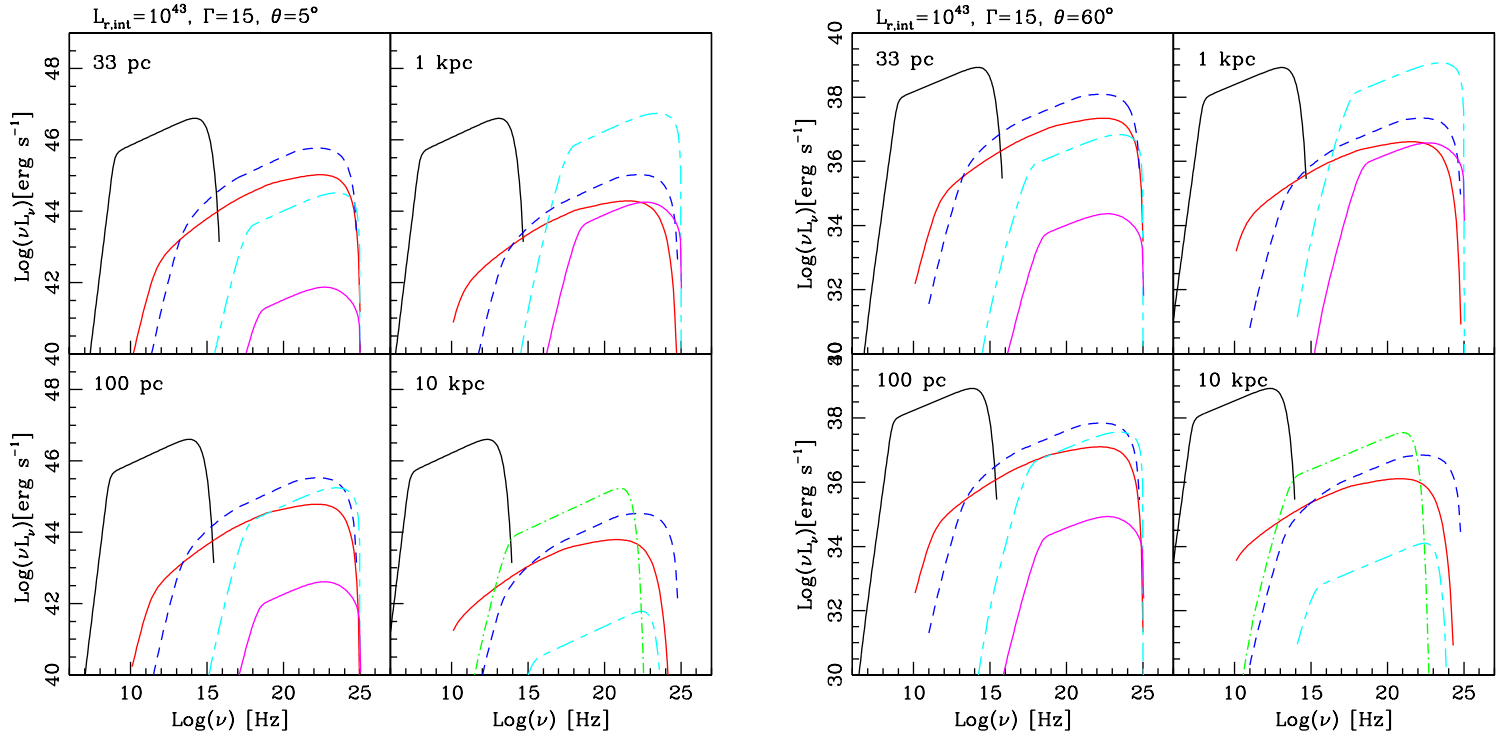

Figure 3.4 Spectral energy distributions for an emitting knot located at 33 pc, 100 pc, 1 kpc, 10 kpc from the core , of intrinsic integrated synchrotron power $L_r = 10^{43}$ erg s^{-1} , moving with a bulk Lorentz factor $\Gamma = 15$ and observed at a viewing angle of $\theta = 5°$ (*Left Panel*), and $\theta = 60°$ (*Right Panel*). The black solid line is the synchrotron emission, red solid one for SSC, blue short-dashed for external Compton off synchrotron photons (EC/syn), cyan long-short dashed for IC of starlight photons (EC/star), green dot short-dashed for IC of CMB photons (EC/CMB) and magenta solid for IC of photons from jet-illuminated NLR (EC/NLR$_{jet}$). The EED is a single power law with spectral index $p = 2.6$, with minimum and maximum electron Lorentz factors $\gamma_{min} = 10$ and $\gamma_{max} = 10^5$. Magnetic field B and normalization of the EED have been calculated under assumption of minimum energy.

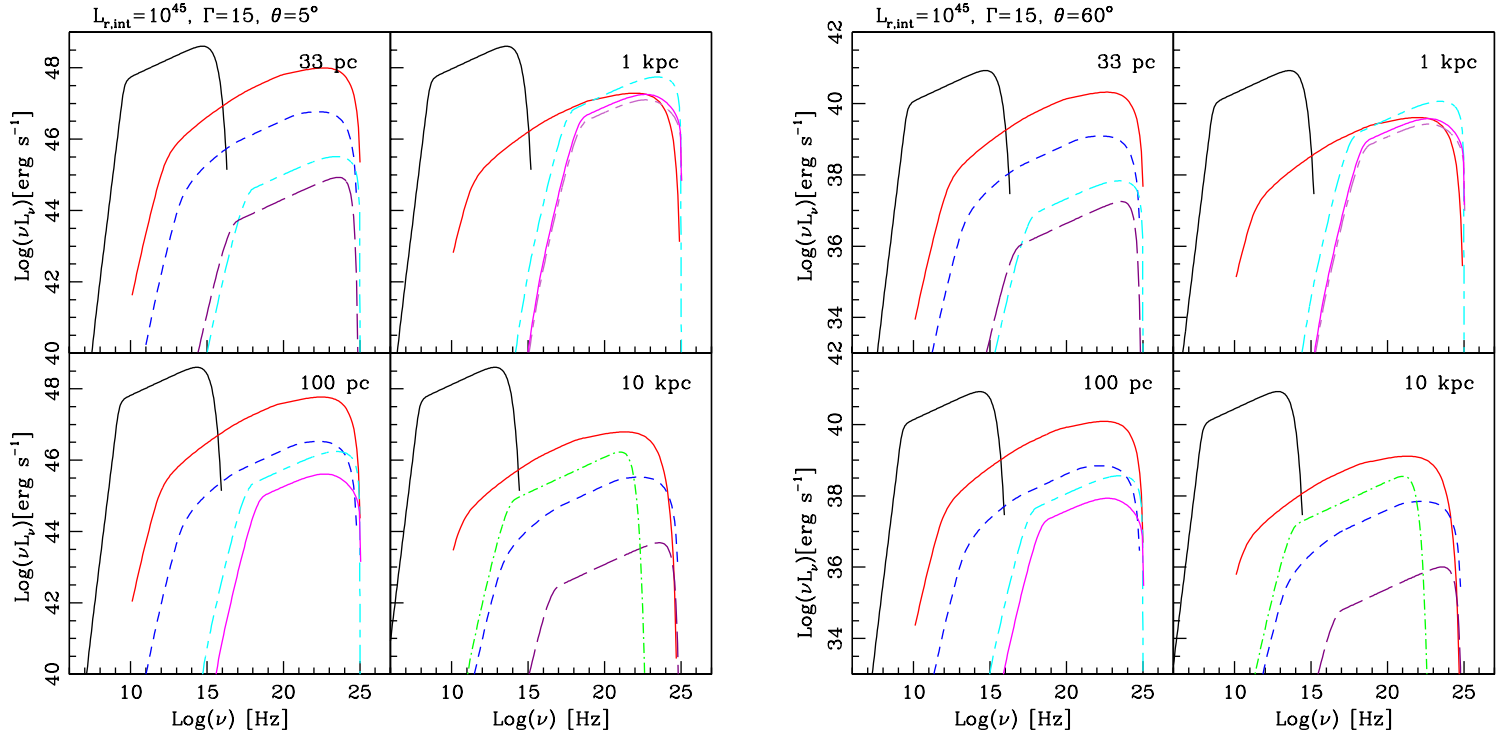

Figure 3.5 Spectral energy distributions for an emitting knot located at 33 pc, 100 pc, 1 kpc, 10 kpc from the core , of intrinsic integrated synchrotron power $L_r = 10^{45}$ erg s^{-1} , moving with a bulk Lorentz factor $\Gamma = 15$ and observed at a viewing angle of $\theta = 5°$ (*Left Panel*), and $\theta = 60°$ (*Right Panel*). The black solid line is the synchrotron emission, red solid one for SSC, blue short-dashed for external Compton off synchrotron photons (EC/syn), violet long-dashed for IC of disk photons (EC/disk), cyan long-short dashed for IC of starlight photons (EC/star), green dot short-dashed for IC of CMB photons (EC/CMB), magenta solid for IC of photons from jet-illuminated NLR (EC/NLR$_{jet}$) and pink short long-dashed for IC of photons from disk-illuminated NLR (EC/NLR$_{disk}$). The EED is a single power law with spectral index $p = 2.6$, with minimum and maximum electron Lorentz factors $\gamma_{min} = 10$ and $\gamma_{max} = 10^5$. Magnetic field B and normalization of the EED have been calculated under assumption of minimum energy.

3.5 Assumptions and Caveats

Here we discuss the main assumptions of the model and the consequences on the results:

- *Assumptions on the geometry* – The knot dimensions depend on the knot linear size through the aperture angle. The knot radius for the maximum considered linear size ($z_d = 10$ kpc) is 1 kpc, in agreement with typical observed knot dimensions. Even though this choice is reasonable, we must note that it partly influences the results on the IC emission, if the energy densities of the target photons is a function of z_d. In fact, the IC luminosity is proportional to:

$$L_{IC} \propto V \times U'_i \propto (0.1 \times z_d)^3 \times 1/z_d^2 \propto 10^{-3} \times z_d. \tag{3.3}$$

  When the jet radius is independently fixed, we have $L_{IC} \propto V \times z_d^{-2} \propto z_d^{-2}$, since V constant. Nevertheless, this is balanced when magnetic field and EED normalization, both depending on the knot volume, are calculated.
  The estimate of torus radius is rather conservative and should correspond to the dimensions of the innermost part of the thick torus, where the hot dust, which produces the near-IR emission, is located. The actual torus dimensions can be larger ($\leqslant 100$ pc) as also its covering factor can be even $> 50\%$. In the case of the obscured GPS radio galaxy Mkn 668 the obscuring matter is confined within the distance between the two radio hotspots (~ 10 pc, Guainazzi et al., 2004). The jet could be still embedded in the torus photon field. Relaxing the assumption on R_{torus} in the smallest sources of the GPS class, the dominant contribution to the X-ray emission from the jet could be given by IC scattering of dusty torus photons. Ostorero et al. (2010) find that it is possible to explain the observed X-ray emission from GPS radio galaxies invoking Compton scattering of the mid-IR torus photons by the relativistic electrons in the lobes.
  Another source of uncertainty is given by the amount of light absorbed in the NLR regions. Photoionization models implying covering factors of 10^{-2} provide good representation of typical observed narrow emission line spectra (Osterbrok and Ferland, 2006; Mor et al., 2009). For lower values of the covering factors, say 10^{-4}, the luminosity associated to the NLR is smaller and the corresponding comptonized component becomes less important.

- *Caveat on the jet luminosity* – The adopted input parameters may imply extreme observed luminosities ($L \geqslant 10^{48}$ erg s^{-1} for $L_r = 10^{45}$ erg s^{-1} and $\Gamma = 15$). This happens for the jet pointing toward the observer and coincides indeed with a blazar source, even though still of compact linear size. Incidentally, we note that the presence of young GPS/CSS radio sources oriented near the line of sight is statistically expected. Interestingly, the model predicts γ-ray emission of the order of $\sim 10^{46}-\sim 10^{47}$ erg s^{-1} from knots located at ~ 1 kpc from the nuclear region, while, in blazar sources, the γ-ray region is usually placed inside the BLR (Dermer and Schlickeiser, 1993; Sikora et al., 1994; Ghisellini and Madau, 1996; Marscher, 1980, the last for an alternative interpretation).

  The model establishes a correspondence between the jet radio luminosity and the bolometric disk luminosity. The same radio luminosity may imply different radiative and kinetic powers, in view of the two bulk motions assumed. A study of the jet power and its relation with the accretion disk was beyond the goals of this stage of the work, limited to explore the radiative output of the jet.

- *Assumptions on the EED and magnetic field* – the electron energy distribution has always been described by a simple power law with $p = 2.6$. It is likely that a better representation of the actual EED would require a more complex form, for example a broken power law, which takes into account possible modifications induced by adiabatic and radiative losses.

  Young radio sources seem to fulfill the condition of energy equipartition between particles and magnetic field (Orienti and Dallacasa, 2008). However, estimates usually refer to radio lobes. Recent combined X-ray and radio studies have shown that, while lobes of giant radio sources are close to equipartition, in many cases it is difficult to reconcile X-ray emission from jet knots and hot spots with standard SSC model without implying a severe equipartition violation (Harris and Krawczynski, 2006, for a complete review). Therefore, the assumptions on B and K_e are conservative. Any larger deviation from the minimum power condition would increase the expected inverse Compton emission, for a fixed synchrotron power.

3.6 Discussion

We have analyzed the effects on jet broadband emission of the expansion in a galactic environment rich of photons. We now discuss the results with respect to the hypothesis that the bulk of the observed X-ray emission in GPS and CSS sources is non-thermal and produced by the jet.

Radio galaxies and quasars are discussed separately. This is motivated by some differences in the X-ray spectra. In particular, radio galaxy X-ray spectra display high ($> 10^{22}$ atoms cm^{-2} Vink et al., 2006; Tengstrand et al., 2009) column densities with respect to quasars, which show no intrinsic absorption with detection limits below $< 10^{21}$ atoms cm^{-2} (Siemiginowska et al., 2008b).

GPS radio galaxies

X-ray luminosities of GPS radio galaxies span between $\sim 9 \times 10^{41}$ and 5×10^{44} erg s^{-1} (see Tengstrand et al., 2009, for a summary of X-ray observations). These luminosities are indeed matched by the modeled IC emission. However, not all the sets of parameter values are suitable for the comparison with GPS radio galaxies. Radio galaxies are considered to lie near the plane of sky. Hence, a main requirement is to limit the comparison with jets observed at large viewing angles.

For $\theta \geqslant 60°$, beamed emission is ruled out as main source of X-rays, either for a radio weak or powerful jet (Figures 3.4, 3.5, *Right panels*). A mildly relativistic jet (Figure 3.3) can produce the required level of X-ray emission. In the case of a radio weak jet, EC/syn emission is the only viable mechanism. Then, the jet scenario for the origin of the X-ray emission is at the same time a scenario for the jet, as a well specific structure is implied. This is not a necessary condition if the jet is radio powerful, as different IC components (SSC, EC/disk and EC/torus) are able to provide the required fluxes. The spectral index assumed for the jet ($\alpha = 0.8$) is softer than the average X-ray spectral index of the sample of GPS sources ($\Gamma = 1.66$ Tengstrand et al., 2009), however the SED results are not strongly modified for $\alpha = 0.66$.

The jet scenario predicts an anti-correlation between the 2-10 keV to 5 GHz luminosity ratio and the source linear size. Tengstrand et al. (2009) report just a weak indication of anti-correlation between the two quantities. The fact that at different scales the dominating photon field changes might partly disturb this correlation. Alternatively, other competing contributions to the X-ray emission could dilute the expected relation. In compact GPS sources, lobes may be strong X-ray emitters via

Compton scattering. A dominant role, among the candidate seed photons, is played by IR emission from the dusty torus (Stawarz et al., 2008; Ostorero et al., 2010). The alternative hypothesis is a thermal origin of the high energy emission, related to the central accretion (Vink et al., 2006; Tengstrand et al., 2009).

GPS and CSS quasars

GPS and CSS quasars have X-ray luminosities between $\sim 10^{43}$-10^{46} erg s^{-1} for 5 GHz luminosity between $\sim 10^{43} - 10^{45}$ erg s^{-1} (Siemiginowska et al., 2008b). In order to compare observations and model, we have assumed a standard viewing angle for quasars of $\sim 30^{\circ}$ and considered an intrinsically powerful source ($L_r = 10^{45}$ erg s^{-1} , Figure 3.6). Despite θ is smaller than for radio galaxies, radiation from a highly relativistic ($\Gamma \sim 15$) jet is still severely debeamed ($\delta \sim 0.5$) and X-ray luminosities in the observer frame are too faint ($\sim 10^{42} - 10^{41}$ erg s^{-1}). As for radio-galaxies, a structured jet is the most efficient radiative scenario, even though the X-ray weakest quasars can be explained also with SSC emission.

In GPS quasars, emission from the nuclear region should not suffer the same degree of obscuration as in radio galaxies. The average 1 keV luminosity, produced in the hot corona via comptonization of the disk photons, has been estimated to be $\sim 10^{1.5}$ times lower than the UV-bump luminosity Koratkar and Blaes (1999). UV luminosities in GPS/CSS quasars can be even fews 10^{46} erg s^{-1} . Hence, it is possible that in the most UV powerful quasars X-ray emission, either related to direct accretion luminosity or associated to a hot corona, dominates over the jet contribution.

We briefly comment on the differences between the non-thermal X-ray emission produced in the jet and in the lobes. Indeed, the main factors which distinguish the two processes are related to the anisotropy/isotropy of the emission, i.e. the jet motion and the orientation of its axis with respect to the line of sight. Therefore, a way to discriminate the origin of the X-ray emission could be through correlated statistical and morphological studies.

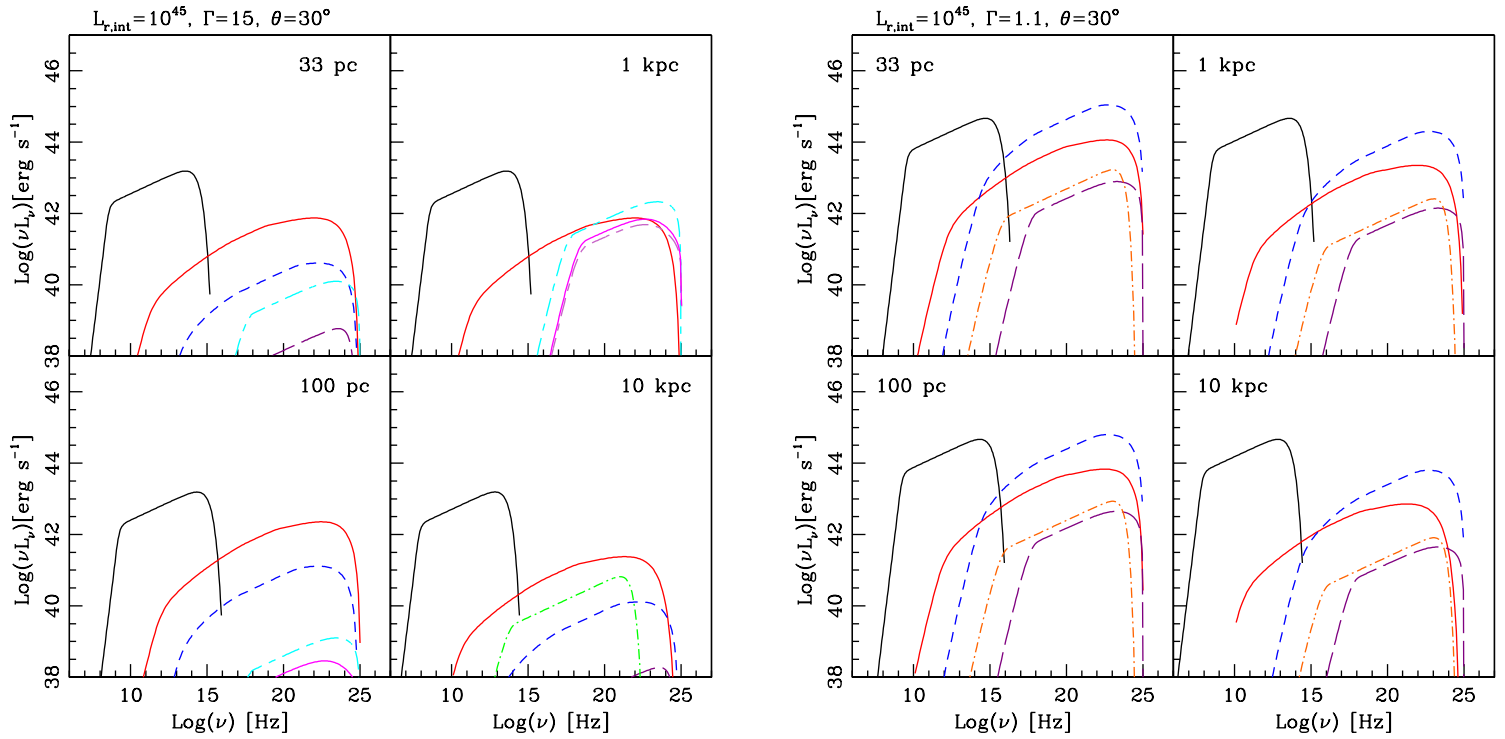

Figure 3.6 Spectral energy distributions for an emitting knot located at 33 pc, 100 pc, 1 kpc, 10 kpc from the core , of intrinsic integrated synchrotron power $L_r = 10^{45}$ erg s^{-1} , moving with a bulk Lorentz factor $\Gamma = 15$ (*Left Panel*) and $\Gamma = 1.1$ (*Right Panel*). The viewing angle is $\theta = 30°$, resembling the case of a quasar. The black solid line is the synchrotron emission, red solid one for SSC, blue short-dashed for external Compton off synchrotron photons (EC/syn), violet long-dashed for IC of disk photons (EC/disk), orange dot long- dashed for IC of toris photons (EC/torus), cyan long-short dashed for IC of starlight photons (EC/star), green dot short-dashed for IC of CMB photons (EC/CMB), magenta solid for IC of photons from jet-illuminated NLR (EC/NLR$_{jet}$) and pink short long-dashed for IC of photons from disk-illuminated NLR (EC/NLR$_{disk}$). The EED is a single power law with spectral index $p = 2.6$, with minimum and maximum electron Lorentz factors $\gamma_{min} = 10$ and $\gamma_{max} = 10^5$. Magnetic field B and normalization of the EED have been calculated under assumption of minimum energy.

GPS and CSS jets in the gamma-ray band

Jets can provide the X-ray luminosities measured in GPS and CSS sources. Interestingly, the modeled SEDs show that GPS and CSS jets should be bright in the GeV photon energy range. The result is partly determined by the shape and the spectral index assumed for the EED (see discussion on the assumptions). However, Stawarz et al. (2008) also find that radio lobes in GPS radio galaxies could also produce γ-ray emission via EC/disk. On the opposite, high energy emission related to accretion phenomena is expected to drastically drop in the MeV-GeV band.

The detection of γ-ray emission associated to young radio sources would represent the unambiguous confirmation of the non-thermal scenario. Specifically, in case of GPS and CSS quasars, the jet origin for the high energy emission is favored with respect to the lobes.

In Figure 3.7 we plot the radio (5 GHz), X-ray (2-10 keV) and γ-ray (0.1-10 GeV) fluxes for a modeled jet of 1 kpc linear size, with $\Gamma = 1.1$, in the CSS quasar case, i.e. $L_r = 10^{45}$ erg s^{-1} and $\theta = 30°$, as a function of the increasing redshift. The 0.1-10 GeV predicted fluxes for SSC, EC/syn, EC/disc and EC/torus emission are compared with the Fermi-LAT (integral) sensitivity after 1 year[1]. While Compton emission related to the nuclear fields and SSC drops at $z \leqslant 0.2$, EC/syn from sources at $\lesssim 0.4$ is above the LAT treshhold. It must be noticed that most of the GPS and CSS quasars are typically found at $0.5 \leqslant z \leqslant 2.0$. The γ-ray fluxes have been estimated for a jet with $\Gamma = 1.1$, excluding the relativistic jet because of debeaming (Figure 3.6, *upper panel*). However, if we assume smaller θ ($\sim 20°$) and less extreme Γ $(6 - 8)$, beaming effects amplify the jet flux and move our observative limit to higher redshifts.

[1] see www-glast.slac.stanford.edu/software/IS/glast_lat_performance.htm and Atwood and Abdo (2009)

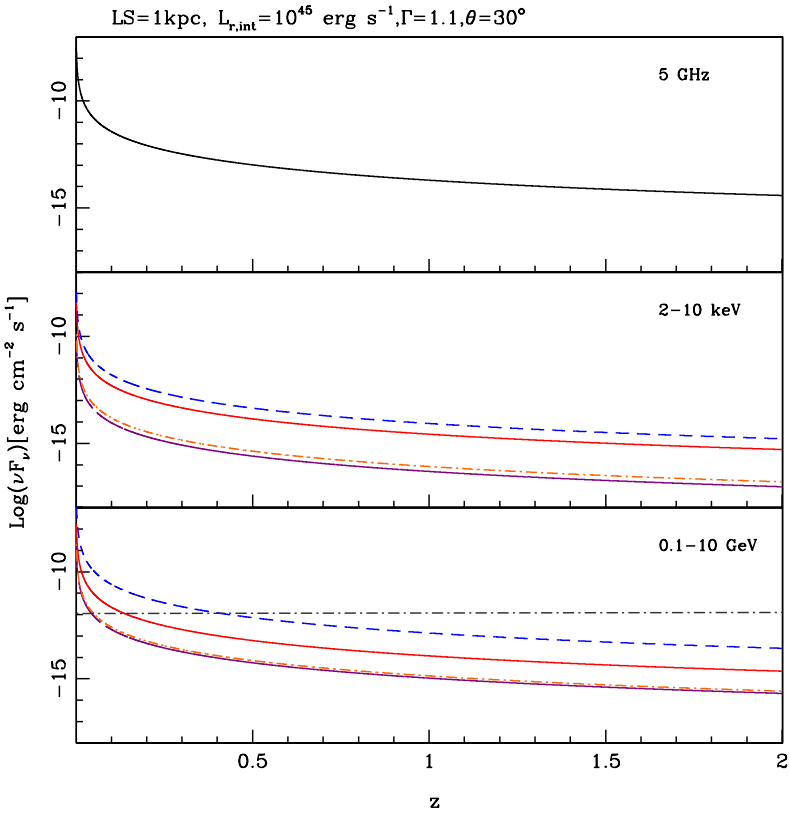

Figure 3.7 radio (5 GHz), X-ray (2-10) and γ-ray (0.1-10 GeV) fluxes as a function of the redshift z for a knot at 1 kpc from the core and moving with $\Gamma = 1.1$. The total intrinsic synchrotron power is $L_r = 10^{45}$ erg s^{-1}. Black solid curve is for the synchrotron 5 GHz flux, red for SSC fluxes, blue short-dashed for external Compton of synchrotron photons, violet for external Compton off disc photons and orange for external Compton of torus photons. The grey dot-dashed horizontal line reproduces the Fermi-LAT 1 year integral flux limit.

4

Jets in Young Radio Sources: the case of 3C 186

4.1 Introduction

The SED modeling method described in chapter 3 has the main goal to investigate the contribution of the jet to the total high-energy emission in compact and young radio sources, with a focus on the most investigated X-ray band. Using standard values, the model predicts significant and complex non-thermal X-ray emission. In particular, the hypothesis that the bulk of the X-ray emission is non-thermal from the jet implies precise constraints on the jet structure for the most X-ray luminous ($L_{2-10} \sim 10^{46}$ erg s^{-1}) radio quasars (Siemiginowska et al., 2008b). Beaming effects exclude a highly relativistic jet, in favor of a knot moving with a low bulk Lorentz factor ($\Gamma = 1.1$). The most efficient radiative mechanism for the production of X-ray emission requires a structured jet with a inner blazar-like knot as source of non-thermal seed photons.

Until now we have considered a generic case of a powerful knot and assumed standard values for the estimate of all the contributions. Here we proceed applying the model to the case of the Compact Steep Spectrum quasar 3C 186. This is one of the few detection of a radio-loud source in an X-ray cluster environment at relatively high redshift ($z = 1.06$). Its 2 arcsec structure is not resolved by the imaging capabilities of the current X-ray telescopes. Unveiling the origin of the bulk of the

high-energy emission is of primary importance in order to understand the evolution of the source and its interactions with the galaxy and cluster environment. The SED modeling provides constraints on the relevant jet parameters, and allows to define the total power carried by the jet.

4.2 Radio-loud quasar 3C 186

3C 186 is a luminous quasar ($L_{bol} \sim 10^{47}$ erg s^{-1}) with a Fanaroff-Riley II (FR II) morphology, located at redshift $z = 1.067$. The small-scale radio structure is characterized by two components, identified as the radio lobes separated by 2 arcsec and a knotty jet connecting the core to the northwest lobe (Spencer et al., 1991).
The steep radio spectrum, a relatively small projected linear size of ~ 16 kpc and a spectral age of $\sim 10^5$ yrs (Murgia et al., 1999) indicate that the source belongs to the class of Compact Steep Spectrum radio quasars.
A diffuse (~ 120 kpc) X-ray emission surrounding the quasar was discovered in the first *Chandra* observation of 3C 186 and identified with the thermal emission from a hot ($kT = 5.2^{+1.3}_{-0.9}$ keV) intracluster medium (Siemiginowska et al., 2005). The study of the properties of the cluster medium and radio source led the authors to the conclusion that the radio source could not be thermally confined by the cluster medium.
The quasar X-ray luminosity ($L_X(2-10 \text{ keV}) = 1.2 \times 10^{45}$ ergs s^{-1}) dominates over the thermal cluster emission in the central region ($L_X(\text{diff}) \sim 10\% - 15\%$ of the total X-ray flux). Nevertheless, its site and nature are not determined. A morphological X-ray study is not possible, since the whole quasar structure is not spatially resolved in the *Chandra* image. The X-ray spectral analysis alone, based on the 38 ksec long *Chandra* observation, is not conclusive. The best fit model, a simple power-law with a steep spectral index ($\Gamma_X = 2.01 \pm 0.07$), is compatible with different hypothesis. Non-thermal emission from the extended components as also a nuclear origin related to Comptonized disk photons by electrons in a hot corona are both plausible.
At the UV wavelengths 3C 186 has a typical AGN spectrum, dominated by an intense big blue bump ($L_{UV} = 5.7 \times 10^{47}$ erg s^{-1}, Siemiginowska et al., 2005), and broad optical emission lines (Netzer et al., 1996; Simpson and Rawlings, 2000; Kuraszkiewicz et al., 2002; Evans and Koratkar, 2004). However, the presence in the quasar X-ray spectrum of the Fe Kα line, which would point to the nuclear origin

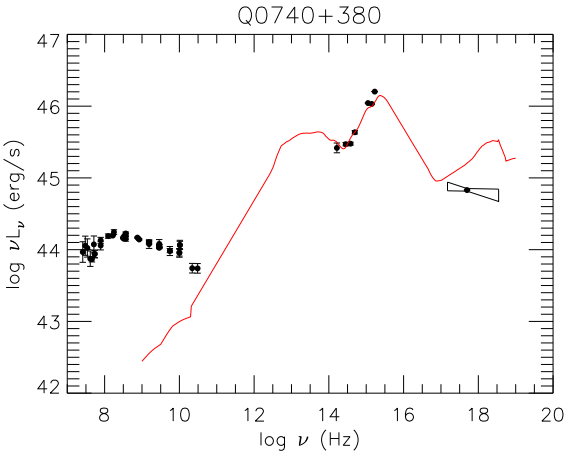

Figure 4.1 3C 186 SED is compared to the average radio-loud SED from Elvis et al. (1994), normalized at a minimum point of logν=14.5, (Siemiginowska et al., 2008b). Photometric data are taken from NED. The *Chandra* data are represented by the 1 σ bowtie regions.

hypothesis, remains uncertain due to the limited statistics. On the other hand the quasar is extremely radio-loud (RL), as can be seen in Figure 4.1 where its broad band (radio to X-rays) spectral energy distribution is compared to the average SED of radio-loud quasars by Elvis et al. (1994). The excess in the radio is also confirmed with respect to a sample of RL quasars selected by Sikora et al. (2007), comparing the radio-loudness parameter[1] values (Siemiginowska et al., 2008b). This plays in favour of a relevant radiative contribution from the radio components which could give a strong X-ray emission.

4.3 Chandra Observations

4.3.1 Observations and Data Analysis

3C 186 has been observed for the second time with *Chandra* Advance CCD Imaging Spectrometer (Weisskopf et al., 2002) on 2007 December 03. The $\sim$ 200 ksec long observation has been divided in four intervals (see Table 4.1).
The source has been located $\sim 1'$ from the default aim-point position on the ACIS-S backside-illuminated chip S3 (Proposer's Observatory Guide [POG]). The observation has been made in VFAINT mode, which ensures a more efficient way of

[1]Radio-loudness parameter is here defined as $R_L = F_{5GHz}/F_B$; F_{5GHz} is the total radio emission at 5 GHz and F_B the B-band flux.

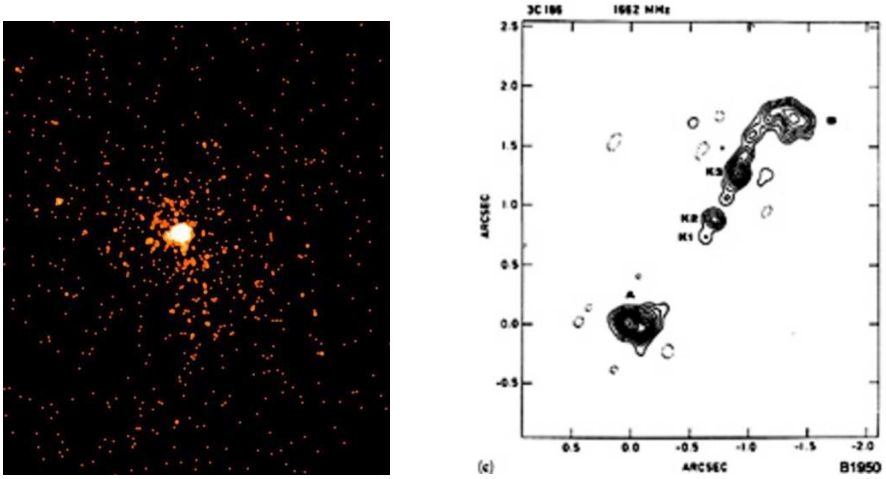

Figure 4.2 *Left panel:* smoothed exposure corrected image of the new *Chandra* ACIS-S observation of 3C 186 in the 0.3-7 keV energy range. *Right panel:* high resolution 1662 MHz combined EVN+MERLIN map (Spencer et al., 1991). The map is convolved to a resolution of 84×84 mas^2 and contours at -2, 3, 6, 10, 14, 18, 24, 30, 40, 50, 60, 80, 100, 140 and 180 mJy beam^{-1}.

Table 4.1. The four new *Chandra* observations of 3C 186

Obs Date	Obs ID	Livetime (s)	Source Counts after filtering
2007-12-03	9407	66323	4189
2007-12-11	9408	39723	2313
2007-12-06	9774	75592	4495
2007-12-08	9775	16389	908

determining the background events and cleaning background, especially at higher energies.
We performed the X-ray data analysis using CIAO version 4.2 and the calibration files from the last CALDB release (4.2). This version includes the upgrade of the ACIS-S contamination file (*acisD1999-08-13contamN0005.fits*), which accounts for the temporal degradation of the detector quantum efficiency due to materials deposition on the ACIS chips or optical blocking filters.
We ran `acis-process-events` to remove pixel randomization and obtain the highest resolution image data. No periods of significative high flares were individuated.
In Figure 4.2 (*Left panel*) the *Chandra* ACIS-S image in the 0.3-7.0 keV band is shown: both the central quasar and the extended cluster emission are clearly visible. The whole quasar structure is included in a circular region of radius smaller than 2 arcsec. The diffuse cluster emission extends to ∼120 kpc from the central quasar.

4.3.2 X-ray Spectral Analysis

The central quasar has a total angular size of $\sim$ 2.2 arcsec. The quasar structure is then completely unresolved in the X-rays because of *Chandra* angular resolution ($\sim 1''$). We defined the quasar emission region as a circle centered on the source coordinates with a radius r=1.75", in order to collect the 98% of the total source emission. A circular region of 28" radius was selected for the background. In this way a source spectrum and the relative background dataset were obtained for each of the four observations. The total counts for each dataset are shown in Table 4.1. Because of the increase of the background at low and high energies, we restricted the analysis to the 0.5-7.0 keV energy band.
We used Sherpa 4.2 (Freeman et al., 2001) to model simultaneously the four background-subtracted, source spectra, applying χ^2 statistic with the Nelder-Mead Simplex optimization method (Nelder and Mead, 1965). All the errors were calculated at 90% confidence limits for a single parameter with the `conf` routine in Sherpa.
We first modeled the spectra with an absorbed power law (*xswabs* and *xspowerlaw* models in Sherpa). The equivalent column was fixed at the galactic value $N_H = 5.68 \times 10^{20}$ cm^{-2}, calculated using COLDEN. The best fit power-law model (see Table 4.2) in the selected energy range has a photon index $\Gamma_X = 2.00^{+0.02}_{-0.01}$.
The unabsorbed fluxes between 0.5-2 keV and 2-10 keV are respectively $F_{0.5-2} = 1.83 \times 10^{-13}$ erg cm^{-2} s^{-1} and $F_{2-10} = 2.13 \times 10^{-13}$ erg cm^{-2} s^{-1}.

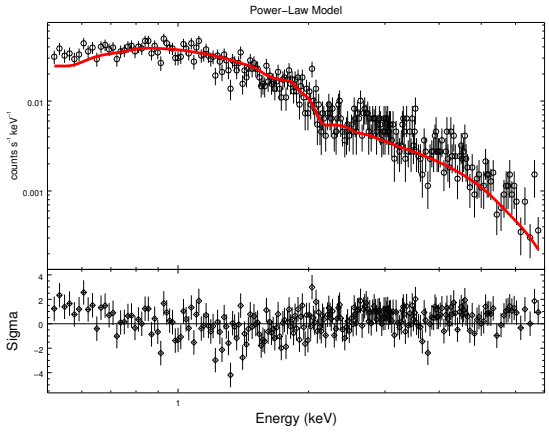

Figure 4.3 *Upper panel:* ACIS-S 0.5-7.0 keV spectrum of the 3C 186 quasar. Here, the data set extracted from the longest observation, ObsID 9774, (*empty points*) is shown with the best fit power law model (*red solid line*). *Lower panel:* residuals are shown in terms of standard deviations of the observed data from the model.

While the spectral index is in good agreement with the results presented in Siemiginowska et al. (2005, 2008b) ($\Gamma_X = 2.01 \pm 0.07$), we note some level of discrepancy between the flux values ($F_{2-10} = 1.7 \times 10^{-13}$ erg cm^{-2} s^{-1}). The different flux is most likely related to the new contamination model applied to our analysis.

We did not detect any significant absorbing column intrinsic to the quasar, with a 3-σ upper limit to the equivalent column of hydrogen of $< 2 \times 10^{20}$ cm^{-2}.

We then test the hypothesis that part of the emission has a thermal origin including a thermal component (*xsmekal* in Sherpa). First we aimed at investigating the contamination due to the cluster emission, fixing the gas temperature at 3 keV on the basis of the results of analysis of the cluster data (Siemiginowska et al., 2010). The metal abundance parameter was set equal to 0.3. This composite model does not improve the level of the fit: power-law parameters are unchanged and the normalization for the thermal component is small ($norm_{kT} = 1.04 \times 10^{-11}$ photons cm^2 s^{-1}). If our assumption on the cluster gas temperature in the central region holds, we can apparently exclude a strong cluster contamination.

As a following step, we left the gas temperature free to vary. The best-fit model for this case is shown in Table 4.2. The gas temperature goes down to 0.6 ± 0.2 keV as the power-law index flattens ($\Gamma_X = 1.86 \pm 0.05$). The contribution of the thermal component in the soft X-ray band (0.5-2 keV) to the total flux is of the order of $\sim 17\%$. The improvement in the fit due to the thermal component is not striking enough to be conclusive on the presence of a cool gas, either related to the quasar

or to the cluster.
We also checked whether there are emission features present in the spectra and determined that there is no evidence for the presence of an emission line in the spectra, the detection of which, at ∼3 keV, was only tentative in the first *Chandra* observation (Siemiginowska et al., 2005).

4.4 3C 186 Jet

The spectral analysis on the new X-ray data confirms that the bulk of the X-ray emission arises from a steep simple power law. A thermal component may contribute at most 17% of the soft X-ray flux. The elusive detection of the Fe Kα line can be explained in term of different competing radiative mechanism, as observed sometimes in RL quasars, with a dominant contribution of the jet. Siemiginowska et al. (2008b) noted that the X-ray spectral indexes of the observed GPS/CSS quasars are typically steeper than the values of 1.57 ± 0.08 (Bechtold et al., 1994b,a) and 1.55 ± 0.17 (Belsole et al., 2006) observed for radio-loud quasars. High resolution radio observations of 3C 186 (Table 4.3) show that all the extended components have a steep spectrum, $\alpha_r \geqslant 1.2$, between 600 MHz and 15 GHz (Nan et al., 1991) and the jet contribution rises at higher radio frequencies ($F_{5\ GHz}(jet) = 93$ mJy and $F_{15\ GHz} = 25$ mJy).
The results of the general SED modeling (Chapter 3) suggest that the observed X-ray luminosities can be consistently explained invoking emission from a mildly relativistic jet and provide some guidelines on the dominant IC components. We then apply this scenario to the jet of 3C 186. The multiwavelength data available allow to perform the analysis of the most relevant seed photons in the quasar environment. In addition, the presence of an axial velocity structure is postulated, assuming a progressively jet deceleration with the increasing distance from the black hole.

4.4.1 Physical parameters

There are some delicate points in modeling the jet broadband SED related to necessary assumptions of the main parameters values, e.g. the geometry of the emitting region, its magnetic field B and electron energy spectrum (EED). The angle between the jet axis and the observer line of sight θ, and the bulk motion Γ are fundamental

Table 4.2. QUASAR MODELS

Model[a]	Γ	$norm_\Gamma$ ($10^{-4}\,phot\ cm^{-2}\,sec^{-1}$)	kT keV	$norm_{kT}$ ($10^{-4}\,phot\ cm^{-2}\,sec^{-1}$)	$\chi^2/d.o.f.$[b]
Power-law[c]	$2.00^{+0.02}_{-0.01}$	$3.4^{+0.1}_{-0.1}$	...	...	849.27/764
Power-law [c]+ Thermal component[d,e]	$2.00^{+0.02}_{-0.01}$	$3.4^{+0.1}_{-0.1}$	$3.0\,(fixed)$	$1.0^{0.2}_{--}$	849.275/763
Power-law [c]+ Thermal component[d,e]	1.86 ± 0.05	$2.8^{+0.2}_{-0.3}$	0.6 ± 0.2	$5^{+2.0}_{-2}$	801.76/762
Power-law [c]+ Thermal component[d,e]	$2.0\,(fixed)$	$3.4^{+0.1}_{-0.1}$	$0.2^{+0.2}_{-0.08}$	27^{+400}_{-23}	819.718/763

[a:] All models include equivalent Hydrogen column of 5.68×10^{20} cm^{-2} in the Milky Way from COLDEN;

[b:] the value χ^2 is given following Nelder and Mead (1965);

[c:] *xspowerlaw* model in Sherpa;

[d:] *xsmekal* model in Sherpa;

[e:] metal abundance parameter is fixed at 0.3.

Table 4.3. Radio data for 3C 186 components: fluxes (F), angular sizes (θ_1, θ_2) and spectral indeces (α). References: Cawthorne et al. (1986), Nan et al. (1991), Spencer et al. (1991), van Breugel et al. (1992), Ludke et al. (1998).

Regions	$600MHz$		$1.6GHz$			$5GHz$	$15GHz$
	$F(mJy)$	$\theta_1 \times \theta_2(mas)$	$F(mJy)$	$\theta_1 \times \theta_2(mas)$	α	$F(mJy)$	$F(mJy)$
A(hot spot+	525	52×15	520	350×250	$\geqslant 1.2$	$\cdots$	$\cdots$
South lobe)	584	203×42	$\cdots$	$\cdots$	$\cdots$	90	20(South East?)
k_1(nucleus)	abs.	$\cdots$	12	$\cdots$	~ 0.0	15	21
k_2(first knot)	$\cdots$	$\cdots$	40	93×65	$\geqslant 1.2$	$\cdots$	$\cdots$
k_3(second knot)	$\cdots$	$\cdots$	80	85×48	$\geqslant 1.2$	$\cdots$	$\cdots$
N-jet(k_3 to B)	$\cdots$	$\cdots$	130	725×100	$\geqslant 1.2$	$\cdots$	$\cdots$
Jet(total)	385	140×44	$\cdots$	$\cdots$	$\cdots$	93	25(Central)
B(North lobe)	315	224×83	290	460×320	$\geqslant 1.2$	$\cdots$	9(North West?)

but partly degenerate parameters with respect to the observables. An appropriate description of the spatial trend of the local and external photon densities is also necessary. Multi-band data and radio maps allow to place some constraints on these quantities.

Jet radio morphology – Radio observations provide us with spatial details on the 3C 186 jet structure, necessary to constrain the physical parameters of the emitting regions. The radio map at 1662 MHz in Spencer et al. (see Figure 2 in the paper) shows a jet with two knots ($k2$ and $k3$) connected to the northern lobe B by a radio low-luminous bridge. In the southern lobe, A, observations at 600 MHz reveal the presence of a hot spot (Nan et al., 1991). The core, $k1$, is self-absorbed below 1.6 GHz. The 600 MHz, 1.6, 5, 15 GHz measurements are summarized in Table 4.3.
The radio surface brightness of the knots (6.62×10^{-3} mJy/mas^2 for $k2$ and 1.96×10^{-2} mJy/mas^2 for $k3$ at 1.6 GHz) and hot spot (0.67 mJy/mas^2 at 600 MHz) is higher with respect to the one of the diffuse structure (1.79×10^{-3} mJy/mas^2), supporting the idea that the compact substructures are the main sites of power dissipation in the jet. Therefore, in modeling the jet emission we will consider only the two knots, and the hotspot and neglect the region of low radio emission.
Jet axis inclination and bulk motion – Symmetrical arguments seem to rule out an extreme alignment ($\theta \leqslant 10^\circ$) of the source along the line of sight: the two lobes, A and B, are located at similar distances from the central region (respectively at 970 and 1250 mas, Spencer et al., 1991). On the other hand, the detection of broad optical lines indicates a direct observation of the inner nuclear region, free from dust obscuration. Thus, unless hypothesizing a large torus opening angle, the source is not lying too close to the plane of the sky ($\theta \lesssim 60^\circ$). The visible jet is pointing towards the lobe more distant from the core, usually interpreted as the farthest from the observer, and is not on the same side of the bright hot spot. Estimates based on the one-sided VLA jet give a $\theta \leqslant 30^\circ$ angle and a corresponding de-projected size of at least ≈ 30 kpc (Siemiginowska et al. 2010). The value CD parameter (CD=−1.66), albeit the uncertainties and caveats, indicates a moderate alignment along the line of sight, Thus, we will assume an inclination angle of 30° and discuss the variation of the modeling results for smaller θ.
Knot/hot spot physical parameters –The deprojected distances, from the radio core location, of the two knots, $k2$ and $k3$, and the hot spot for the assumed $\theta = 30^\circ$ derived from the 18-cm radio data (see Table 3 in Spencer et al., 1991), are respectively $z_d(k2) \sim 2.4$ kpc, $z_d(k3) \sim 9.8$ kpc and $z_d(hs) \sim 15.4$ kpc. We calculated the

physical volumes using the 1.6 GHz maps for the two knots and the 600 MHz map for the hot spot assuming a cylindrical geometry (in Table 4.3 the smallest angular size corresponds to the base diameter and the longest to the height).
We calculated the advance velocity of the jet v_{ad} from the linear size and the source age. For a linear size spanning between 15 and 30 kpc, i.e. the projected linear size and the deprojected one at $\theta = 30°$ respectively, and an estimated source age of $\sim 10^5$ yrs (Murgia et al., 1999), v_{ad} ranges between $0.24c$ and $0.49c$. The lower value is close to the typical hot spots' advance velocities of CSS sources (Katz-Stone and Rudnick, 1997; Owsianik and Conway, 1998) and almost an order of magnitude larger than the values found for giant doubles. Based on these results, we assume an approximated bulk Lorentz factor of 1.1.
Magnetic field and EED – The magnetic field, B, and particle densities, U_e, are initially calculated under equipartition assumption and adjusted to match the observed fluxes. As no indications of a complex spectral shape can be extrapolated by the observed SED, we assume a simple power law for the electron energy distribution, $N(\gamma) = k_e\gamma^{-p}$: p is derived from the lower limit of radio spectral index $\alpha_r \leqslant 1.2$, $p = 2\alpha_r + 1 = 3.4$ and the minimum and maximum Lorentz factors are set equal to $\gamma_{min} \sim 50$ and $\gamma_{max} \sim 10^5$.

4.4.2 Photon fields

The local synchrotron photon densities U'_r for each component have been calculated using the intrinsic integrated synchrotron luminosities, $L'_r(k2/k3/hot\ spot) = 3 \times 10^{43}/9 \times 10^{43}/1.6 \times 10^{44}$ erg s^{-1} from Equation 2.1, reported in Chapter 2.
The energy densities of disk and torus photons ($U'_{disk/dust}$) have been calculated assuming that, at the knot minimum distance ($z_d \sim 1$ kpc), both the structures can be considered point-like sources (Equation 2.2). The estimated disk luminosity of 3C 186 is $L'_{disk} = 5.7 \times 10^{46}$ erg s^{-1}. With the assumed parameters, the corresponding energy density is $U'_{disk} \approx 2 \times 10^{-8}/(z_d/kpc)^2$ erg cm^{-3}.
The IR luminosity of 3C 186 ($L_{IR} = 2.9 \times 10^{45}$ erg cm^2 s^{-1} in the 1.6-10 μm band) is completely ascribed to the dusty torus. Haas et al. (2008) have shown that in high-z quasars the galaxy contribution is a factor of 5-10 below the heated dust component. In order to account for the torus vertical thickness, we assume that all the dust emission comes from a height of ∼10 pc above the disk position. This means that $z_d(torus) = z_d(disk) - 10$ pc. The energy density of torus photons in 3C 186 can be written as $U'_{dust} \approx 6 \times 10^{-9}/(z_d(torus)/kpc)^2$ erg cm^{-3}.

The analysis of the radiative fields shows that starlight emission can be a competing source of seed photons at $\sim$ 1 kpc for a luminous knot (Figure 3.2, *lower panel*). Carballo et al. (1998) have measured the magnitude of the host galaxy of 3C 186 in the K-band ($m_V(gal) = 17.1$), which should be a good indicator of the starlight emission. The galaxy contribution in the band is estimated to be about $\sim 18\%$ of the total K-luminosity. Since the starlight emission appears dominated, both in the IR to UV band, by the quasar emission, we have neglected here this contribution.
The quasar is located at relatively high redshift and the CMB energy density proportional to $(1+z)^4$ and Γ^2 (Formula 2.7) is higher than the one considered in Chapter 2 (calculated at $z = 0.1$). Notwithstanding, given the low knot bulk Lorentz factor ($\Gamma = 1.1$), U'_{CMB} is still significantly smaller than the other photon fields ($U'_{CMB} \sim 9 \times 10^{-12}$ erg cm^{-3}).
As a final step, we estimate the contribution of the continuum emitted by a region of jet in highly relativistic motion. The modeling of this component is rather delicate, since in 3C 186 there is no observative evidence of its presence. However, its existence is somehow expected if the Unified Scheme of Active Galactic Nuclei holds, and quasars are the counterparts of the aligned flat spectrum radio quasars (FSRQs). We then modeled the fast inner blob as a typical blazar-like region. The observed core ($k1$) radio emission ($L_r(k1)$) is used to normalize synchrotron luminosity of this blazar-like component. Bulk Lorentz factor values between 10 and 20 are usually adopted to model the SED of blazar sources (Celotti & Ghisellini 2008, Ghisellini 2010), with few extreme cases of blazars in flaring state (for instance, in PKS 2155-304 the SSC modeling gives $\Gamma \approx 100$, Finke et al. 2008). Here we assume a moderate bulk motion of the blazar-like component, $\Gamma_{in} = 11$, which gives an intrinsic synchrotron luminosity of $\approx 8.0 \times 10^{44}$ erg s^{-1}. The energy density of the synchrotron photons from this component, measured in the rest frame of the outer knot (in this case either $k2$, $k3$ or hot spot), is calculated using equation 2.14.

In Figure 4.4 we show the energy densities of the photon fields as a function of the distance z_d for a jet (i.e. a knot in our approximation) with a bulk motion Γ=1.1. The de-projected positions of the two knots (assuming $\theta = 30$ degrees) and the hot spot in 3C 186 jet are marked by vertical lines and the values of the local synchrotron fields U'_{SSC} are represented by solid points.
The beamed emission (U'_{in}) is the dominant field even at large scales ($\approx$ 20 kpc). For comparison, we also show the case in which the jet has no velocity structure (i.e. $\Gamma_{in} = 1.1$): the nuclear fields, $U'_{disk,dust}$, are the most intense at the scale of the first knot $k2$ ($z_d \lesssim$3 kpc). Due to the intensity of the disk radiation, U'_{disk} can

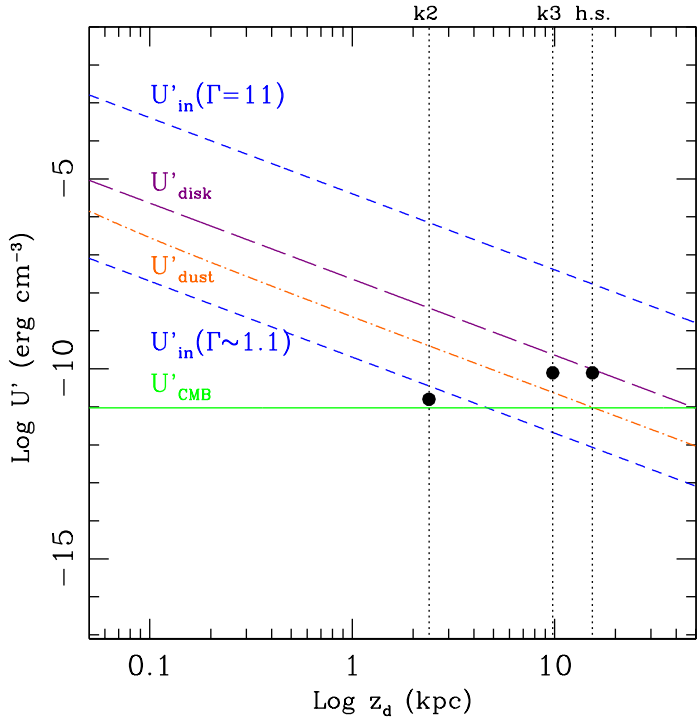

Figure 4.4 Energy densities as a function of the distance from the base of the jet z_d in the reference frame of the mildly relativistic ($\Gamma = 1.1$) knot. The external photon fields are: U'_{disk} (long-dashed), U'_{dust} (dot-dashed), U'_{CMB} (solid) and U'_{in} (short-dashed). The energy density of the external synchrotron photons are estimated for a highly relativistic ($\Gamma \sim 11$) knot (blazar-like) and, for comparison, for a mildly relativistic knot ($\Gamma_{in} \sim 1.1$). The dotted vertical lines mark the position of the two knot and the hot spot in 3C 186 and the black solid points correspond to the energy densities of the local synchrotron fields (U'_{SSC}). The projected distance scale assumes $\theta = 30$ degrees.

be higher, or comparable with, the local synchrotron emission U'_{SSC} up to the hot spot distance ($z \approx 15$ kpc). We note that U'_{CMB} is relatively less important below $z_d \approx 20$ kpc as the amplification factor related to the knot/hot spot bulk motion is low ($\Gamma^2_{(knot/hot\ spot)} \sim 1.2$).

4.4.3 Multiwavelength mapping results

The results of the photon field analysis show that the nuclear photons and the beamed external synchrotron radiation dominate at the scales of the first knot $k2$. In addition, U'_{disk} and U'_{in} are more intense than, or comparable with, U'_{SSC} even at the hotspot distance. This and the fact that the volumes and energy densities of the electrons in the knots and hot spot are similar imply that the bulk of the IC emission of the jet should be produced close to the nuclear region. Thus, we can use the knot nearest to the core as a reasonable approximation to model the jet high-energy emission.

In Figure 4.5, we show the results of the SED modeling of the $k2$ knot emission together with the observed 3C 186 SED. The black points are the multiwavelength data taken from ASDC archive[2], the green one is the Spitzer flux ($F_{15\mu m(1+z)} = 8.2 \pm 0.6$ mJy, Leipski et al., 2010) and the bow-tie the 1 keV flux from the *Chandra* data presented in this paper.

The synchrotron emission of $k2$ (*black solid line*) is normalized to the 1.6 GHz flux (*magenta point*). Disk (*violet solid line*) and torus (*orange solid line*) emission have been modeled as simple blackbodies peaking at $\sim 10^{15}$ Hz and $\sim 10^{13}$ Hz, respectively. In the model of the structured jet, $k2$ corresponds to the slow moving knot. The synchrotron emission of the blazar-like component is normalized using the observed radio emission of the core ($k1$), assuming a spherical region of radius $R_{in} \sim 2 \times 10^{17}$ cm, moving with $\Gamma_{in} = 11$ in a magnetic field $B'_{in} = 1.1$ G. The dashed lines represent the Comptonization (Thomson regime) of the non-thermal, local (SSC) and external synchrotron (EC/syn) photons and of the thermal, disk (EC/disk) and torus (EC/torus) photons by the relativistic electrons in $k2$ knot.

In the high energy band (X-ray to γ-rays), the SSC emission gives a negligible contribution ($L_{SSC} \leqslant 10^{40}$ erg s^{-1}). The luminosities of the EC/disk and EC/torus (in the observer rest frame) can reach values of the order of a few 10^{43} erg s^{-1} but still stay below the observed X-ray emission. We also note that the EC/torus and EC/disk luminosities peak at different frequencies: the up-scattered torus photons

[2]http://tools.asdc.asi.it/SED/

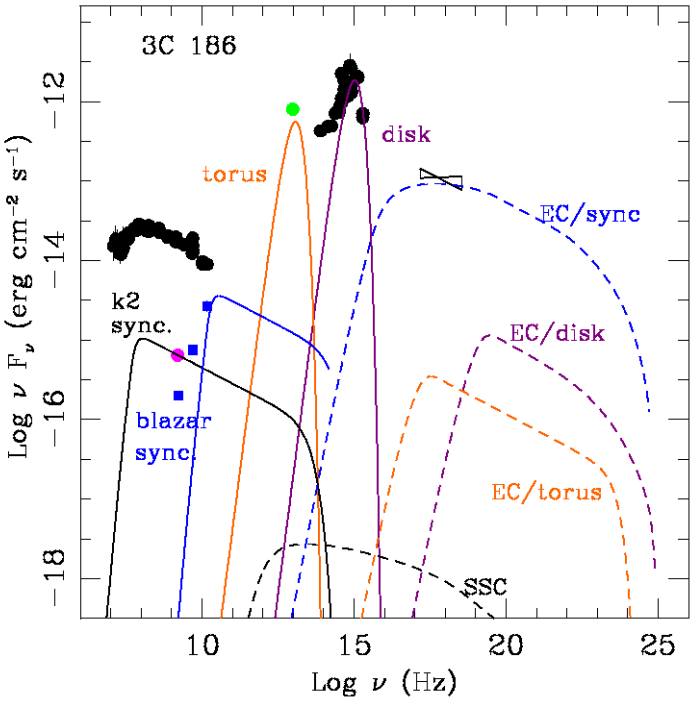

Figure 4.5 Data and modeled SED of the knot $k2$, located at ≈ 2 kpc of distance from the jet apex. Data: black solid points are taken from ASDC archive, the green point is the Spitzer flux (Leipski et al., 2010), the magenta point is the 1.6 GHz flux for $k2$ and the blue squares are the radio fluxes for the core, $k1$ (Spencer et al., 1991). The X-ray data (*black "bow-tie"*) are from the *Chandra* observation here presented. The red arrow is the upper limit of Fermi-LAT flux. Model: the black solid line is the $k2$ synchrotron emission, the orange and violet solid lines are the torus and disk emission and the blue solid line is the synchrotron emission of the core, blazar-like, component (see the text). The dashed lines corresponds to the Comptonization of the synchrotron and nuclear photons with colour correspondence with the seed photons as follows: SSC emission is the black dashed line, orange and violet dashed lines reproduce the upscatterd torus (EC/tours) and disk (EC/disk) photons and the blue dashed line is the EC of the external core synchrotron photons (EC/syn).

are mostly emitted in the 2-10 keV band and the bulk of the comptonized UV photons above 10^{19} Hz. Overall, the contribution of the inverse Compton emission off the nuclear and local-synchrotron photon fields is not significant in the X-ray band. However, in the framework of the structured jet model, the observed *Chandra* flux can be reached via up-scattering of the synchrotron photons from the blazar-like component by the electrons in the slow moving knot.

4.5 Discussion

The SED modeling of 3C 186 provides even stronger indications on the jet contribution to the X-ray (and high energy) emission of the quasar with respect to the previous general predictions.

The first evidence is that under the assumed conditions the jet is not radiatively relevant with respect to the observed X-ray flux, unless a velocity structure is present. Is it possible to change this result with different assumptions? SSC emission should imply a drastic violation of equipartition between magnetic field and particles. The particle energy density should be about 4 orders of magnitude larger than the magnetic field one, even considering the second knot $k3$ and the hot spot. Flux amplification related to the jet motion is limited by beaming and affects equally the synchrotron and IC curves. Then, a calibrated change of θ and Γ still implies a strong particle dominance.

It is possible to raise the X-ray EC/torus emission to the required X-ray flux moving the position of the dissipative knot nearer to the core at $z_d(torus) \sim 120$ pc. However, under the assumption that the jet section is proportional to its length, the knot volume at smaller distances decreases and the knot flux with it.

We now investigate deeper the implications of the structured jet model we have considered. A significant reduction in the velocity of the jet with the increasing distance from the centre is the determinant factor to ensure the mechanism efficiency. We can justify the drastic change in terms of strong deceleration of the jet with the expansion, or replacing the slow outer knot with an external layer of the jet, possibly slowed down by the interaction with the surrounding medium (Stawarz and Ostrowski, 2002; Ghisellini et al., 2005).

A second aspect is the jet total power, L_{kin}, implied by the model. We can calculate the kinetic and radiative powers for the two knots $k1$ and $k2$. The kinetic powers

Table 4.4. 3C 186 Jet Powers estimated for the two velocity jet model.

	$k1$	$k2$
L_e (erg s^{-1})	3.2×10^{46}	2.0×10^{45}
L_p (erg s^{-1})	1.1×10^{48}	3.5×10^{46}
L_B (erg s^{-1})	2.1×10^{47}	7.8×10^{44}
L_{kin} (erg s^{-1})	1.13×10^{48}	3.7×10^{46}
L_r (erg s^{-1})	1.1×10^{47}	1.8×10^{45}

are given by:

$$L_i = \pi R^2 \Gamma^2 \beta c U_i' \tag{4.1}$$

where U_i' is the energy density, in the comoving frame, of electrons, $U_e = m_e c^2 n_e < \gamma >$, cold protons, $U_p = m_p c^2 n_p$, and magnetic field, $U_B = B^2/8\pi$. Here, we assume one cold proton per electron ($n_p = n_e$), m_e and m_p are respectively the electron and proton masses and, $< \gamma >$ is the average electron Lorentz factor.
The analogous component associated to radiation is:

$$L_r = \pi R^2 \Gamma^2 c U_{rad}' \sim L' \Gamma^2 \tag{4.2}$$

with L' intrinsic total (synchrotron and IC) luminosity.
The results for the kinetic and radiative powers calculated on the basis of the parameters of the two knots are shown in Table 4.4.
The values obtained for $k2$ are rather standard. Its jet kinetic power is also in rough agreement with the one ($L_{kin} \sim 2.4 \times 10^{45}$ erg s^{-1}) given in Siemiginowska et al. (2005). The latter is derived by the relation between radio luminosity at 151 MHz and jet power (Willott et al., 1999) and, given the significant scatter in the relation, has to be considered as an order of magnitude estimate.
The kinetic power of $k1$ ($L_{kin} \sim 1 \times 10^{48}$ erg s^{-1}) is instead in the high energy tail respect to what found usually for powerful radio sources, ranging between 10^{46} and 10^{48} erg s^{-1} (Celotti and Ghisellini, 2008; Ghisellini et al., 2009, 2010a). This result is driven by the assumption made on protons. Excluding them, the jet at its base would result magnetically dominated ($L_B = 2 \times 10^{47}$ erg s^{-1}) and highly dissipative ($L_r \sim \times 10^{47}$ erg s^{-1}). The difference between the two jet powers in $k1$ and $k2$ of about 2 orders of magnitude implies that the power should not be conserved along the jet. Some kind of efficient dissipation is required going from sub-pc to

kpc scales to make the two results consistent. Alternatively, we should hypothesize two subsequent outbursts with a significative different intensity. Several studies suggests that compact sources should display recurrent phases of radio activity on short timescales of $\sim 10^3 - 10^5$ years (Baum et al., 1990; Reynolds and Begelman, 1997; Owsianik and Conway, 1998; Czerny et al., 2009). The possible presence of an extended radio of 10 arcsec relic in the cluster hosting 3C 186, indicated by initial studies on VLA radio data (Siemiginowska et al., 2008a), needs still the final confirmation (Siemiginowska et al., 2010).

The jet power calculated from $k1$ is almost 2 orders of magnitude larger than the estimated bolometric luminosity, $L'_{bol} \sim 10^{47}$ erg s^{-1} (Siemiginowska et al., 2010). Recent studies on blazars, based on high energy (X-ray to γ-ray) observations, find that the jet power is proportional but larger than the disk luminosity (see for a summary Ghisellini, 2010). This would have interesting consequences in the frame of the source-IGM interactions (feedback), which, in this case, would be driven by the mechanical work done by the jet. Conversely, if the hypothesis of the structured model is rejected, the jet kinetic power calculated using $k2$ parameter, is at most comparable to the disk luminosity. In this case, both the mode (radiative versus mechanical) and intensity of the power conveyed into the ambient together with the scale of the interactions (pc versus kpc), are very different.

4.6 Summary

Our purpose was to investigate the role of the jet emission to the total high-energy and X-ray radiation in the compact, young and powerful quasar 3C 186. The results of the spectral analysis based on a new deep *Chandra* observation are ambiguous. The best-fit model, a single power-law with a steep slope ($\Gamma = 2.00^{+0.02}_{-0.01}$, $F_{2-10} = 2.13 \times 10^{-13}$ erg cm^{-2} s^{-1}), is compatible with non-thermal emission from the extended jets and lobes as well as thermal emission related to the central accretion.

The jet broad band emission has been modeled including the up-scattering of external seed photons relevant in the CSS environment, i.e. disk and torus photons. Following the general SED modeling result, we also tested the effects on the total emission of the presence of a velocity gradient in the jet.

The SED modeling shows that the observed *Chandra* X-ray flux is matched by the jet only invoking external Compton emission of the beamed synchrotron radiation

from the blazar-like component. Then, the relevance of the jet as a source of high-energy radiation in 3C 186 seems strictly related to its dynamical structure.
Indeed, this extreme scenario is questionable under many aspects. Incidentally, we note that estimates of the X-ray emission related to the disk emission based on Koratkar and Blaes (1999) give $L_X \sim L_{UV}/10^{1.5} \sim 2 \times 10^{45}$ erg s^{-1} in agreement with the observed X-ray luminosity. Also, the structured jet scenario has some strong implications on the jet evolution and on the quasar-source feedback mode. Dynamically the jet has to decelerate on kpc scales. An initial, rather high jet kinetic power ($L_{kin} \sim 10^{48}$ erg s^{-1}) is required, comparable to the most powerful blazar sources. In order to be coherent with the kinetic power values measured in the external knot $k2$ and from the power stored in the radio lobes, the jet power has to experience a strong dissipation on kpc scales. The alternative hypothesis involves outflows with different intensities. The initial jet power is almost 2 orders of magnitude larger than the disk luminosity. As a consequence the interactions with the galaxy first and the cluster then should be dominated by the jet rather than by the disk emission.

5

Probing the jet structure: NGC 6251

5.1 Introduction

The study of the spectral energy distribution in compact and young radio sources seems to funnel the jet hypothesis into a rather specific direction. A jet, with emitting components moving with different velocities, is not only a very efficient radiative mechanism to produce X-ray emission, but also, most likely, the only viable solution to save the (jet) non-thermal scenario in GPS/CSS quasars, as seen in 3C 186. However, in compact sources there are no evidences of the presence of such a structure. Differently, in giant radio sources, support to this idea comes from: comparative studies on parent populations (Chiaberge et al., 2000), high resolution radio observation (Swain et al., 1998; Giovannini et al., 2001a; Giroletti et al., 2004) and the surprising discovery of γ-ray and TeV emission from radio galaxies (Ghisellini et al., 2005; Tavecchio and Ghisellini, 2008).

In particular EGRET detection in γ-ray band, of the radio galaxies Centaurus A (Steinle et al., 1998) and NGC 6251 (Mukherjee et al., 2002), as of M87 in the TeV band with HEGRA, has been explained by some authors with a spine-layer model (Ghisellini et al., 2005; Tavecchio and Ghisellini, 2008). This allows to solve the incongruity of the low bulk motions ($\Gamma \lesssim 3-4$), with respect to the typical BL Lac values, required by fitting the SED with a synchrotron self Compton model (Chiaberge et al., 2001, 2003; Guainazzi et al., 2003).

Renewed interest arises now with the detection by the Large Area Telescope (LAT, Atwood and Abdo, 2009), onboard of *Fermi* Gamma-ray Space Satellite, of 11 misaligned[1] AGN (MAGN, Fermi-LAT Collaboration, 2010, , hereafter AA).
Here, the radio galaxy NGC 6251, one of the sources in the MAGN sample detected by LAT, is used as a case study to probe the jet structure. The source is suitable for this study under many aspects: it has been widely observed and we dispose of a good broadband coverage, with multi-epoch radio and X-ray observations. In particular, the γ-ray detection is fundamental to determine the shape of the high energy curve. It belongs to the FR I class and previous studies have shown a nuclear SED dominated by the jet non-thermal emission (Chiaberge et al., 2003; Guainazzi et al., 2003; Ghisellini et al., 2005; Foschini et al., 2005), suggesting an inefficient accretion flow. Therefore, similarly to BL Lac sources, the nuclear environment should be relatively poor of photons. This limits the number of IC components to that have to be taken into account and favor the study of the jet structure itself.

5.2 NGC 6251

NGC6251 (z=0.02471) is an elliptical galaxy with a flux density of $\sim 4 \times 10^{24}$ W Hz^{-1} sr^{-1} at 178 MHz, typical of FRI radio galaxies. It exhibits a spectacular radio emission with a extension of 1.1 degree (Waggett et al., 1977). At a distance of 106.4 Mpc (for $H_0 = 71$ km s^{-1} Mpc^{-1} $\Omega_m = 0.27$, and $\Omega_\Lambda = 0.73$), this corresponds to a linear extension of 1.9 Mpc (1"=491 pc).
High resolution VLA studies revealed a radio core and a complex kpc jet, initially bright and structured (within 4.4'/113 kpc) and then faint and curved (Perley et al., 1984). Sudou and Taniguchi (2000) showed that the angle between the jet axis and the line of sight increases by more than 10 degrees going from 50 arcs to 200 arcs from the core . The VLBI maps show an asymmetric core-jet radio structure aligned with the VLA jet (Jones et al., 1986).

Non-thermal radiation is present in the infrared bands. Although dust emission is dominant at 15-30 μm, a jet contribution of $\sim$30% to the total mid-IR Spitzer flux was estimated by Leipski et al. (2009). A synchrotron process is probably responsible also for the bulk of the optical to UV core emission ($\leqslant 0.2''$) as suggested

[1] this term include radio galaxies and Steep Spectrum Radio Quasars (SSRQ) whose jet is thought to point away from the observer.

by Chiaberge et al. (2003). However, the nuclear region in the optical band is complex. An obscuring ($A_V = 0.88 \pm 0.13$ mag), extended (1.43") dusty disk not perpendicular to the radio jet is seen in Hubble Space Telescope images. Moreover, ionized gas in motion around a black hole of 4-8 $\times 10^8$ $M_\odot$ is confined in the region (0.3" 150 pc) of the disk (Ferrarese and Ford, 1999).

NGC 6251 has been observed by the main X-ray satellites. There is general agreement on the spectral shape of the source, that is well-fit by a composite model: a thermal emission and intrinsically absorbed power law. The presence of the iron line Fe Kα is still debated (see Turner et al., 1997; Guainazzi et al., 2003; Gliozzi et al., 2004; Evans et al., 2005). The unresolved core is the main X-ray emitter although high resolution imaging of Chandra resolves X-ray distinct emission in three different jet regions (Evans et al., 2005). An extended ($\sim$ 100 kpc), X-ray thermal ($kT \sim 1.7$ keV) halo has been detected by ROSAT (Birkinshaw and Worrall, 1993), Chandra (Mack et al., 1997; Evans et al., 2005) and XMM-Newton (Sambruna et al., 2004b). A drop in the surface brightness of the X-ray halo, in positional agreement with the northern radio lobe, suggests that the lobe has evacuated a cavity in the X-ray surrounding gas (Kerp and Mack, 2003; Evans et al., 2005).

This source has been also detected at hard ($>$ 10 keV) X-ray energies by Beppo-Sax (Guainazzi et al., 2003; Grandi et al., 2006) and INTEGRAL (Foschini et al., 2005) and was proposed as a counter-part of the EGRET source 3EG J1621+8203 (Mukherjee et al., 2002). Very recently *Fermi* confirmed that NGC 6251 is a GeV source (AA). Several authors analyzed the complete SED (from radio to γ-ray) and argued that the observed nuclear emission is likely to originate in the relativistic jet. Indeed, the SED shows a typical double-hump shape, characteristic of blazar sources (Chiaberge et al., 2003; Guainazzi et al., 2003; Ghisellini et al., 2005; Foschini et al., 2005). Most of these conclusions rely on the extension of the SED up to GeV energies. Its recent undoubted detection by *Fermi* /LAT (AA) seems to provide further support to the non-thermal scenario.

5.3 Spectral Energy Distribution

5.3.1 Observational Constraints

Site of the gamma-ray emission

One of the crucial topic under discussion concerns the site of production of the γ-ray photons, whether in the core region or in the extended structures. Currently, ongoing simultaneous multi-frequency VLBI, X-ray/Swift and FERMI campaigns (Sokolovsky et al., 2010; Giovannini et al., 2010) aim at trace the γ-ray origin and constraint the physical parameters (as size, magnetic field) of the region. For blazar sources, preliminary results based on high frequency radio observations and correlated variability at different bands seem to indicate the bright radio core as the favorite candidate. In MAGNs observed by *Fermi* -LAT, no significant γ-ray variability has been detected, with the exception of NGC 1275 (Abdo, 2009; Kataoka et al., 2010, AA). It is unclear if this is a real effect or a consequence of the proximity of the MAGN LAT fluxes to the detector flux threshold. However, multi-wavelength variability studies for MAGNs result severely hampered/limited. Moreover, the *Fermi* -LAT discovery of γ-ray emission from the lobes of Cen A has revealed the radio lobes as a further possible site of γ-ray photons (Fermi-LAT Collaboration Abdo, 2010). In NGC 6251 the location of the γ-ray emission in the nuclear region appears to be the most consistent hypothesis. Besides the analogy with the parent population of BL-Lac sources, this is also supported by the results of the multi-wavelength analysis. The nuclear non-thermal emission is relevant, if not dominant, at all the wavelengths (excluding the optically thick domain). The X-ray spectral analysis, using high resolution Chandra data, has shown that the bulk of the X-ray emission comes from the nuclear region ($r \leqslant 4$ arcsec), while the jet knot accounts for no more than 10% of the total X-ray observed flux (Evans et al., 2005, and this paper). In Jones et al. (1986) (see Figure 12), the core and jet-knot radio fluxes are compared at different frequencies: the core is optically thick below $\sim$ 13.5 GHz, and becomes dominant at higher radio frequencies. We also note that NGC 6251 was observed by EGRET (Mukherjee et al., 2002) in a brighter flux state respect to the *Fermi* detection. This could be indicative of γ-ray variability on time scales of years and makes unlikely the hypothesis of γ-ray emission from the lobes.

Dimensions

Observations allow to derive some constraints on the physical parameters of the emitting region. VLBI observations (Jones et al., 1986) place an upper limit of $\leqslant 0.20$ mas ($\sim 3 \times 10^{17}$ cm) to the size of the nuclear region. There is not clear evidence of flux variability on short timescales which could provide more stringent limits. Gliozzi et al. (2004) reported the detection of short-time ($\sim 10^4$ s), low-amplitude X-ray flux variation. Evans et al. (2005), analyzing XMM-Newton and Chandra data, conclude that variations in 2-10 keV fluxes are plausible but not certain. Radio fluxes (VLBI) vary of a factor near 2 over time-scales of years, corresponding to a region radius R of few $\sim 10^{18}$ cm/parsecs.

Jet orientation and Bulk motion

Another key question for MAGNs is the orientation of the jet, expected to be large in the objects with no extreme blazar characteristics. The jet inclination, a very elusive quantity, is a fundamental ingredient to understand the physical processes of sources moving at relativistic speed.

Here we propose a range of possible values of the jet inclination for NGC6251, obtained using three different observational quantities: the jet sidedness (J), the VLBI apparent velocity v_a of the jet knots and the Core Dominance. If an intrinsic symmetry is assumed, the ratio between jet and counter-jet brightness ratio J can be expressed in term of the jet velocity (β) and orientation (θ): $J = (\frac{1+\beta cos\theta}{1-\beta cos\theta})^{(2+\alpha)}$, with $\alpha = 0.5$. In a similar way the apparent transverse velocity of a relativistic emitting blob is related to β and θ via $v_a = \frac{\beta sin\theta}{1-\beta cos\theta}$ (Urry and Padovani, 1995). Giovannini et al. (2001b) found a general correlation between the core and total radio power in radio galaxies $LogP_c = 0.62 LogP_{tot} + 7.6$, where P_c is the arcsecond core radio power at 5 GHz, and P_{tot} the total radio power at 408 MHz. This relation can be easily used to derive upper and lower limits of β and θ (for details see Giovannini et al., 1994), allowing the core density to vary within a factor of 2. Thus, if P_c and P_{tot} are known and J and v_a values/upper limits are available, a narrow region of permitted values can be defined in the β versus θ plot .

In NGC 6251 the counter jet observed in VLA maps (Perley et al., 1984) disappears at mas scales. Jones and Wehrle (2002) investigated the possibility that free free absorption by ionized accretion disk could hide the receding jet, but concluded, on the basis of the high electron density required, that relativistic boosting effects better explain the observations. In line with their considerations, we assume that

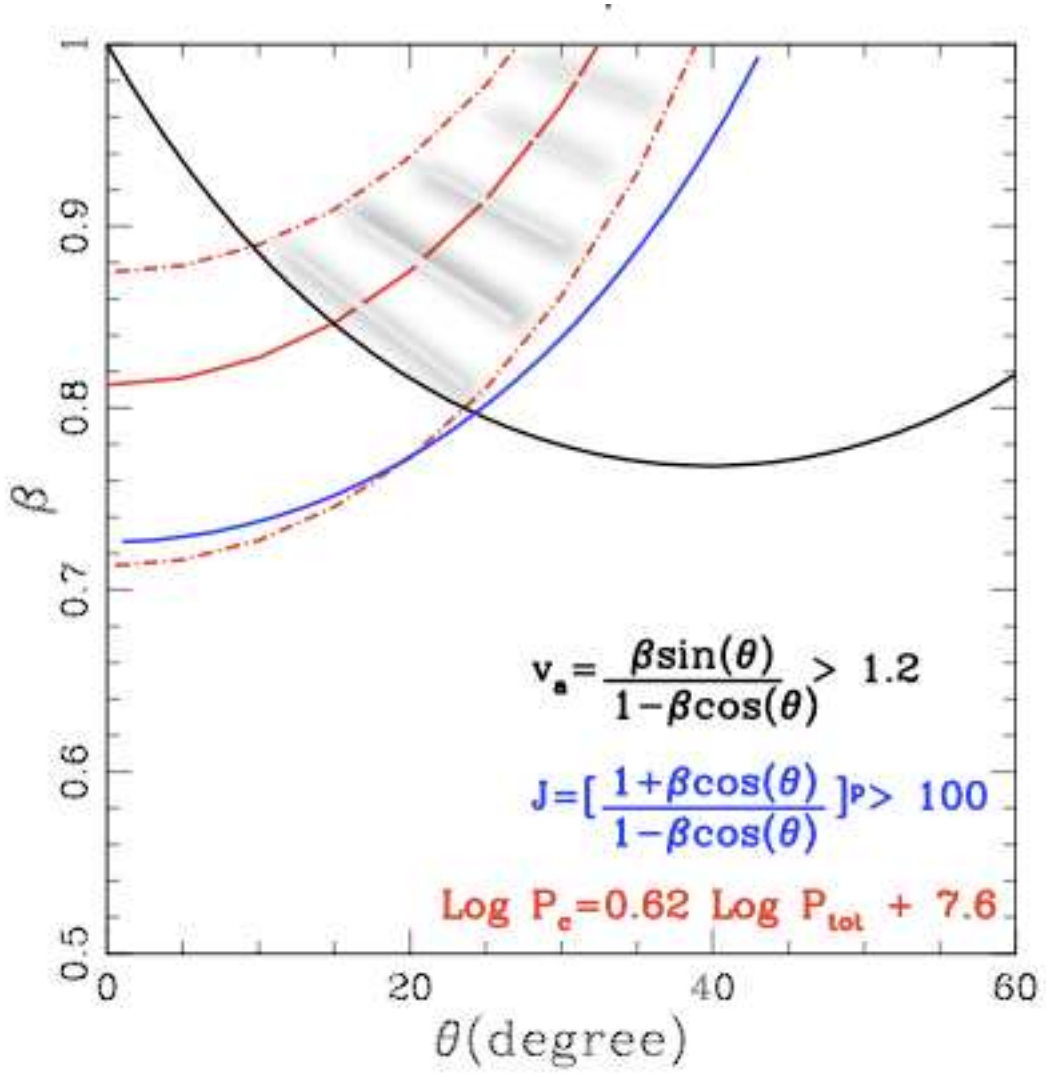

Figure 5.1 Constraints on the angle θ between the jet and the line of sight and the jet velocity β in unit of the speed of light. Blue and black curves correspond to $J = 100$ and $v_a = 1.2c$, respectively. The red curve is from the P_c versus P_{tot} relation. The doted-dashed red lines are obtained allowing the core density to vary by a factor 2. The dashed gray area corresponds to the permitted values of β and θ.

the brightness ratio 100:1 measured within 6 mas of the core is a plausible lower limit for J (Jones and Wehrle, 1994). Superluminal velocity of the jet has been never observed in NGC6251. Only a lower limit of $v_a > 1.2c$ has been provided by Jones and Wehrle (1994). Finally, the values of $P_c = 0.4$ Jy (Perley et al., 1984) and P_{tot}=5.3 Jy (Waggett et al., 1977) were considered to estimate the jet inclinations and velocities allowed by the Core Dominance correlation.
The final β-θ plot is shown in Figure 5.1. The permitted values (dashed gray region) are within the area delimited by $J > 100$, $v_a > 1.2c$ and the Core dominance relation. Only bulk motions larger than $\sim 0.78c$ and inclination angles ranging from 10 to 40 degrees are possible for the NGC6251 jet.

5.3.2 Radio to Optical-UV Data

The radio to UV data shown in Table 5.4 are used to build the nuclear broad-band SED of NGC 6251. All fluxes are collected from literature. We note that radio fluxes are taken at different angular resolution and sample nuclear regions of different dimensions. Moreover, data are not simultaneous and variability could then be an issue. However, Evans et al. (2005), with an inspection of radio fluxes over 17 years, limit the maximum flux variability to a factor of $\leqslant 2$ (see Table 9 in Evans et al., 2005).
The IR flux (15-30 μm) is decomposed and the synchrotron jet emission, extrapolated from the radio data (Leipski et al., 2009), is estimated to be the $\sim$30% of the total IR emission. The sharp drop in the near-IR (NIR) to optical/UV band is interpreted as due to dust-extinction. Then, de-reddening ($A_V = 0.88 \pm 0.13$ mag) has been calculated for the the optical-UV data have been de-reddened assuming $A_V = 0.88$ using the extintion curves of Cardelli et al. (1989).

5.3.3 High Energy Data

All the Chandra, XMM-Newton and Swift observations available in the public archives were re-analyzed (see below) and included in the SED.

We analyzed only the most recent and longest Chandra observation of the source (November 2003) that was performed in ACIS–S (S3 and S4 chips) configuration. The Chandra pointing of September 2000 is not taken into account because in this observation the core fell in a chip gap and it cannot help in constraining the physical parameters of the source. Data were reprocessed using the *Chandra Interactive*

Analysis of Observation (CIAO v.4.1) and the *Chandra Calibration Database* CALDB 3.5.1. After correction for high particle background the total exposure time reduces to 45 ks. The nuclear spectrum was extracted from a circular region of 5" radius centered on the source. The background was chosen in an adjacent circular region with radius 12". The observation is piled up. We estimated a pile up fraction of nearly 13% from the PIMMS software [2]. However even excluding the inner 1" circle from our extraction region, the effects of pile up are still present in the spectrum. For this reason we decided to not consider the Chandra point in the SED. As an extended extra-nuclear emission associated to the kpc jet is clearly visible in the Chandra image, a spectrum was also extracted for this component. The accumulation region is a box of 20" and 5.3" each side, far 6" from the nucleus. An analogous box was chosen for the background. A good fit is obtained by using a simple absorbed power–law with Γ=$2.3^{+0.26}_{-0.24}$ and $N_{H_{Gal}}$ =5.7×10^{20} cm^{-2}. The 0.5–2 keV unabsorbed flux is 3.1×10^{-14} erg cm^{-2} s^{-1}, while the 2–10 keV flux is 2.3×10^{-14} erg cm^{-2} s^{-1}.

The XMM–Newton observation of NGC 6251 was analyzed using the latest software and calibration files available (SAS v.9.0). We excluded time intervals affected by high background. After this data cleaning we obtained a net exposure of 8.7 ks with a count rate of 1.867±0.015 count s^{-1} for the pn and 13.9 ks and 0.553±0.006 count s^{-1} for MOS1, 13.5 ks and 0.556±0.006 count s^{-1} for MOS2. The source and background spectra were extracted from circular regions of 27" radius. The response matrices were created using the SAS commands RMFGEN and ARFGEN. The observation of the nucleus is not piled up. Data were grouped to 25 counts per bins in order to apply the χ^2 statistic. The best fit model for the pn (0.3-10 keV) data consists of an absorbed power–law plus an APEC component (χ^2=408 for 372 dof). The parameter values are reported in Table 2. The same results (not shown in Table 2) are obtained using MOS data. There is no strong evidence for the Fe Kα emission line.

The Swift X–Ray Telescope data were reduced using the on–line XRT data analysis provided by the ASDC [3]. Source spectra for each observation were extracted from a circular region of 20" radius, while the background was taken from an annulus of inner–radius 40" and outer–radius 80".The data were rebinned to 20 counts per bin in order to apply the χ^2 statistics. All spectral fits were performed in the 0.5–10 keV band. Data can be well fitted by an absorbed power–law with column density slightly in excess with respect to the Galactic value. Unlike XMM.Newton, the XRT

[2]http://cxc.harvard.edu/toolkit/pimms.jsp
[3]http://swift.asdc.asi.it/

Table 5.1 X-ray data analysis results

Satellite	XMM-Newton/PN	Swift/XRT	Swift/XRT	Swift/XRT
Obs date	2002-03-26	2007-04-07	2009-05-05	2009-06-05
N_H ($\times 10^{21}$ cm^{-2})	1.0±0.01	$1.5^{+0.08}_{-0.07}$	$1.9^{+0.12}_{-0.11}$	1.1±0.1
Γ	1.88±0.04	$2^{+0.23}_{-0.21}$	$2.2^{+0.35}_{-0.31}$	$2.03^{+0.35}_{-0.31}$
norm ($\times 10^{-3}$)	1.16±0.05	$8.5^{+2.1}_{-1.6}$	$7.2^{+2.8}_{-2.0}$	$6^{+2.1}_{-1.5}$
kT (keV)	0.63±0.2	–	–	–
norm ($\times 10^{-5}$)	$(5.0^{+2.4}_{-2.1})$	–	–	–
$\text{Flux}^a_{(0.5-2keV)}$	2.7×10^{-12}	1.9×10^{-12}	1.6×10^{-12}	1.33×10^{-12}
$\text{Flux}^a_{(2-10keV)}$	3.6×10^{-12}	2.11×10^{-12}	1.42×10^{-12}	1.45×10^{-12}

Unabsorbed fluxes in unit of erg cm^{-2} s^{-1}

spectra, characterized by a lower signal-to-noise ratio, do not require the addition of a soft thermal emission (see Table 2).

For EGRET and *Fermi*-Lat data we refer to the papers of Mukherjee et al. (2002) and Abdo et al. 2010.

5.4 SED Modeling

5.4.1 One-zone SSC and structured jet models

First, we model the SED of NGC 6251 with a one-zone synchrotron self-Compton (SSC) model, where the seed IC photons are the local synchrotron photons themselves. We assume the geometry of a spherical homogeneous blob. On the basis of the VLBI constraints (section 3.1), we placed an upper limit for the blob radius of 10^{18} cm.

Radio observations provide constraints on the inclination of the jet axis with respect to the observer line of sight θ and the jet bulk motion β. As discussed in section

3.1, jet counter-jet flux ratio, apparent velocity and the Core Dominance relation define a range of allowed values for the core jet speed β and relative inclination θ. We decided to assume $\theta = 25°$ and $\beta = 0.91$, which roughly coincide with the center of the area of the permitted values in Figure 5.1. The resulting beaming factor is $\delta = 2.4$.

Looking at the broad-band SED (Fig. 2), the synchrotron and IC peaks can be approximately located respectively in the frequency intervals 10^{13-14} Hz and 10^{21-22} Hz. Quillen et al. (2003) report a spectral index $\alpha_{os} = 1.1$ between the sub-millimeter (870 μm) and the optical band, while the IR-to-UV slope between 16,000 and 2,200 A is $\alpha_{IR-UV} = 1.75 \pm 0.16$ (Chiaberge et al., 2003). The spectral index values in the high energy band, $\alpha_X = 0.88 \pm 0.04$ between 2 and 10 keV and $\alpha_\Gamma = 1.52 \pm 0.12$ in the *Fermi* -LAT frequency interval, are slightly flatter than the sub-mm-UV α but still consistent. Quillen et al. (2003) also note that dust extinction can partially reduce the flux of the optical continuum in the core and determine the spectral steepening. Then, as a reasonable approximation, we assume the same spectral indexes for the synchrotron and IC curves below ($\alpha_1 = 0.88$) and above ($\alpha_2 = 1.52$) the peaks and adopt a broken power-law to describe the energy distribution, $N(\gamma)$, of the emitting electrons (EED):

$$N(\gamma) = \begin{cases} K_e \gamma^{-p1} & \text{if } \gamma_{min} \leqslant \gamma < \gamma_b, \\ K_e \gamma_b^{p2-p1} \gamma^{-p2} & \text{if } \gamma_b \leqslant \gamma < \gamma_{max}. \end{cases} \tag{5.1}$$

where γ is the usual electron Lorentz factor which spans between γ_{min} and γ_{max}, K_e is the EED normalization, $p1 = 2\alpha_1 + 1$ and $p2 = 2\alpha_2 + 1$ are the low and high energy EED spectral indexes and γ_b the energy break of the distribution. From the ratio between the synchrotron (ν_s) and IC (ν_c) peak frequencies, using the formula:

$$\gamma_b = \left(\frac{3\nu_c}{4\nu_s} \right)^{1/2} \tag{5.2}$$

we can derive a range of value for γ_b spanning between$\sim 3 \times 10^3$ and $\sim 3 \times 10^4$.

The best fit SSC model for the nuclear SED of NGC 6251 is shown in Figure 5.2 (*Upper panel*) and the corresponding model parameters are reported in Table 5.2. The intrinsic parameters of the emitting region, comoving radius ($R = 1.2 \times 10^{17}$ cm) and magnetic field ($B = 0.037$ G) are in the ranges typical for BL Lac sources (Tavecchio et al., 2010). However, the beaming factor ($\delta = 2.4$) and inclination angle ($\theta = 25^o$) , based on observational constraints, necessarily imply a quite slow

Table 5.2. NGC 6251 nuclear SED - Models

Parameters	Model 1	Model 2	
	SSC	Layer	Spine
R (cm)	1.2×10^{17}	8.0×10^{16}	1.0×10^{16}
L (cm)	$\cdots$	2.5×10^{16}	1.0×10^{15}
K (cm^{-3})	1.5×10^{6}	7.0×10^{4}	7.1×10^{4}
γ_{min}	250	60	100
γ_{max}	1.4×10^{5}	4.1×10^{4}	2.0×10^{4}
γ_b	2.0×10^{4}	7.0×10^{3}	3.0×10^{3}
$p1$	2.76	2.76	2.1
$p2$	4.04	4.04	3.0
B (G)	3.7×10^{-2}	0.7	1.8
δ	2.4	2.4	0.7

jet with $\Gamma = 2.4$. For comparison, typical bulk Lorentz factors of BL Lac objects are $\Gamma = 10 - 20$ (Kellermann et al., 2004)

The values of the main parameters are similar to the results of the SSC model fitting of NGC 6251 in Chiaberge et al. (2003), where $\theta = 18°$ and $\Gamma = 3.2$ were assumed. The particle to magnetic field energy density ratio is $U'_e/U'_B \gtrsim 400$, where $U'_e = m_e c^2 n_e \langle\gamma\rangle$ (m_e: electron mass, $\langle\gamma\rangle$: average electron Lorentz factor) and $U'_B = B^2/8\pi$. The violation of the minimum energy assumption is then rather severe already without considering any contribution from the protons.

In summary, the SSC model provide a good overall fit of the data, but the relatively slow motion of the jet is a challenge for the BL-Lac FRI unification as previuosly pointed out by other authors (Chiaberge et al., 2000, 2001).

We then apply the spine-layer model. This model was already apply by Ghisellini et al. (2005) to the case of NGC 6251. However, we note that the new *Fermi* detection and additional (Spitzer and Swift) data in the IR band provide us with a more precise description of the overall SED partly improved with respect to what previously possible.

The fit to NGC 6251 nuclear SED applying the spine-layer model is shown in Figure 5.2 (*Lower Panel*). The geometry of the two regions is cylindrical (L is the cylinder length), with the spine nested inside the hollow layer cylinder. The spine parameters in Table 5.2 are chosen to reproduce a standard BL Lac object: $\Gamma_{spine} = 15$ for a region of radius $R_{spine} = 10^{16}$ cm in an intense magnetic field ($B_{spine} = 1.8$ G). The spine EED is a broken power-law with $p1 = 2.1$ and $p2 = 3.0$ and an energy break

$\gamma_{b,spine} = 3.0 \times 10^3$. We keep the same spectral shape as before for the layer EED ($p1 = 2.76$ and $p2 = 4.04$) as also the same δ and θ. We note that the estimates of the non-thermal contribution to the total Spitzer flux imply a low energy spectral index of the layer EED significantly steeper than what assumed in Ghisellini et al. ($p1 = 1.6$).

The red and black solid (dashed) curves in Figure 5.2 (*Lower Panel*) represent the layer (spine) SSC model, without including the seed photons coming from the spine (layer). The blue long-dashed curve is the layer IC emission of the spine synchrotron photons. The feedback between the spine and layer ensures the efficiency in reproducing the observed X-ray to γ-ray emission and requires a low particle density ($K_{layer} = 7 \times 10^4$ cm^{-3}) in favour of larger magnetic field ($B_{layer} = 0.7$ G). On the other hand, the strong de-beaming ($\delta_{spine} \sim 0.7$), that occurs to the spine emission at $\theta = 25^o$, hides the presence of the fast flow.

A critical point is that the spine-layer model assumes a flux variability of the spine radiation similar to what observed in blazar sources. Rapid changes in the spine synchrotron flux should reflect in the IC layer emission with timescales of the order of $t_{var} \sim (R/c)\delta_{layer} \sim 6.5 \times 10^6$ sec. In NGC 6251 no clear indication of variability, in X-rays as in γ-rays, has been yet revealed. It might be that the layer volume dimensions could partially dilute the expected variability of the high energy flux.

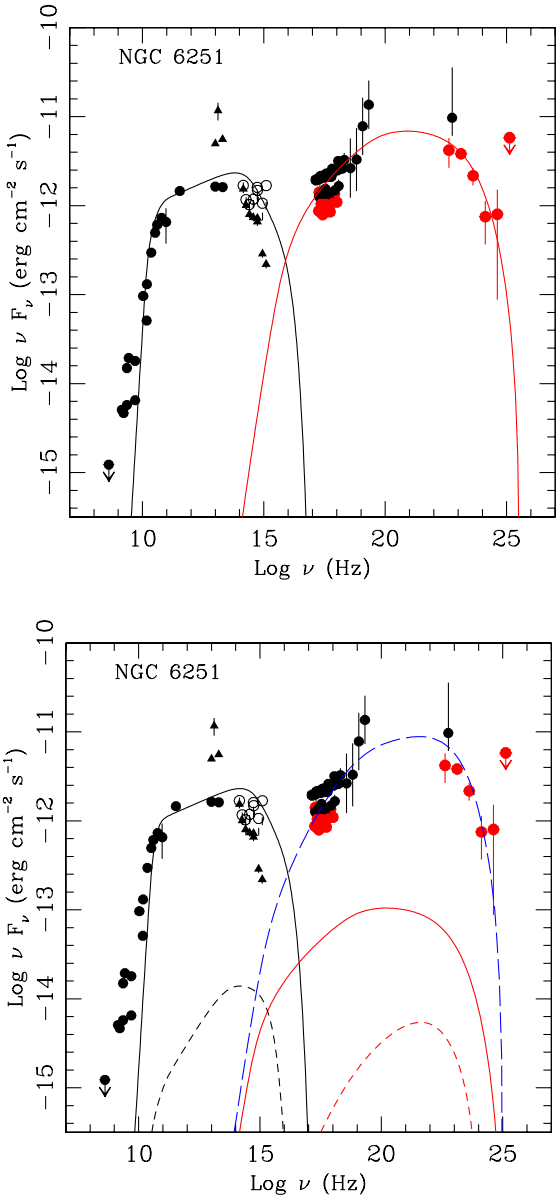

Figure 5.2 Nuclear broadband SED of NGC 6251 compiled using multi-epoch data. Black-dotted radio to optical-UV data are reported in Table 5.4. Empty dotted optical-UV data are dereddened (see Table 5.4). X-ray emission is presented in Section 3.3: black dots are for XMM-Netwon data and red from Swift satellite. Black dotted γ-ray point correspond to EGRET flux (Mukherjee et al. 2002). Red dotted γ-ray are *Fermi* data (AA) *Left Panel:* the SED is modeled with a one-zone SSC model (solid black line: synchrotron curve, solid red line: IC emission). *Right Panel:* the SED is modeled with the spine-layer model illustrated in Ghisellini et al. (2005). Solid back and red lines reproduce the SSC emission of the layer. Dashed black and red curves are the SSC model for the spine. The long-dashed blue lines is the IC emission of the spine synchrotron photons off the layer relativistic electrons.

Table 5.3. NGC 6251 Jet Powers for the SSC and spine-layer Models

	Model 1	Model 2	
	SSC	Layer	Spine
L_e (erg s^{-1})	1.6×10^{44}	3.9×10^{42}	4.8×10^{43}
L_p (erg s^{-1})	4.9×10^{44}	5.2×10^{43}	2.2×10^{44}
L_B (erg s^{-1})	3.6×10^{41}	2.3×10^{43}	4.8×10^{43}
L_{kin} (erg s^{-1})	6.5×10^{44}	7.9×10^{43}	3.2×10^{44}
L_r (erg s^{-1})	2.0×10^{43}	2.4×10^{43}	9.0×10^{43}

5.5 Jet Powers

The SED modeling allows to infer the physical parameters of the emitting region and then to derive the jet kinetic powers and Poynting flux.

Jet powers for electrons (L_e), protons (L_p) and Poynting flux (L_B) are calculated using Formula (4.1) in Chapter 4. We assume one cold proton per electron and that all the electrons are radiating. The radiative power is then calculated using Equation (4.2), in Chapter 4.

The kinetic and radiative jet powers for the two applied models, SSC and spine-layer, are shown in Table 5.3. The SSC model implies a strong particle dominance ($L_e \sim 1.6 \times 10^{44}$ erg s^{-1} and $L_p \sim 5 \times 10^{44}$ erg s^{-1}) over the magnetic field ($L_B \sim 3.6 \times 10^{41}$ erg s^{-1}). The radiative power is $L_r \sim 2 \times 10^{43}$ erg s^{-1}, about an order of magnitude below the kinetic power. In this case, the bulk of the jet power is conserved and goes in the formation of the large radio structures. The values are in the range of powers derived for typical BL-Lacs (Celotti and Ghisellini, 2008; Ghisellini et al., 2010a; Tavecchio et al., 2010), even though we note that L_B is in the low-power tail of L_B values for BL Lacs (Celotti and Ghisellini, 2008). Two interesting results are then inferred from the SSC model: 1) L_e and L_p are dominated by the particle number n_e and n_p more than by the low Bulk Lorentz factor. In other words, we are considering a relatively slow and heavy jet; 2) The low Poynting flux seems to exclude a magnetically confined jet.

On kpc scales the jet expands at variable lateral velocity and exhibits the presence of re-confinement sites (Perley et al., 1984). Several authors (Perley et al., 1984; Mack et al., 1997; Evans et al., 2005) have shown that the pressure exerted by the extended (out to 100 kpc) halo of X-ray emitting gas around the radio source can

account for the jet confinement on kpc scales. On the other hand, in the inner few seconds the jet is rapidly expanding and thermal confinement would required an X-ray luminosity incompatible with the observed one. An initial regime of free expansion seems then more likely (Perley et al., 1984). It remains then an issue understanding the jet evolution from pc to Mpc scales.
On the contrary, in the spine-layer model the jet is in average faster and less heavy and magnetic fields could play a fundamental role in its confinement. The total jet kinetic power derived from the spine-layer model parameters is just slightly smaller ($L_{kin} \sim 3 \times 10^{44}$ erg s^{-1}). Differently, the spine-layer model introduces a source of external seed IC photons and requires a lower number of relativistic particles respect to the SSC model to obtain the same IC flux, while the magnetic fields are near to equipartition with particles (Ghisellini et al., 2005). The bulk of the jet kinetic power is carried by the fast spine.
The radiative dissipation ($L_r = 9 \times 10^{43}$ erg s^{-1}) is rather high in the spine. The jet converts about the 30% of its total power into radiation, and should then undergo a strong progressive deceleration, as also predicted by the Compton rocket effect (Ghisellini et al., 2005). Nevertheless, we observe that NGC 6251 has an extraordinary linear extension of ~ 1.9 Mpc.

5.5.1 Checking the Kinetic Jet Power

In order to check the reliability of the kinetic power derived from the SED modeling (with Equation 4.1), we compare it with the estimates based on the integrated power stored into the lobes. First, we apply the relation between the jet power and the observed radio luminosity at 151 MHz, L_{151} (Willott et al., 1999):

$$L_{kin} = 3 \times 10^{45} f^{3/2} L_{151}^{6/7} \; erg \; s^{-1}, \tag{5.3}$$

where L_{151} is in units of 10^{28} W Hz^{-1} sr^{-1}. In the revised formula considered here, a factor f takes into account possible systematic underestimates intrinsic to the technique. Hardcastle et al. (2007) estimate f in the range between 10 and 20 for a sample of FRI and FRII sources. The 151 MHz luminosity of NGC 6251 is $L_{151} = 2.46 \times 10^{24}$ W Hz^{-1} sr^{-1}, and the kinetic power, setting f respectively equal to 1 and 15, is in the range 2.4×10^{42}-1.44×10^{44} erg s^{-1}.
An alternative approach is based on the work done by the radio lobe to evacuate a cavity in the X-ray halo (Evans et al., 2005). The PdV work done by the lobe can

be calculated assuming pressure equilibrium between the relativistic component in the lobes and the external thermal plasma (Fabian et al., 2002; Allen et al., 2006). The total energy content, E_{tot}, of the lobe is:

$$E_{tot} = \frac{1}{\gamma_2 - 1} PV + PV = 4PV \tag{5.4}$$

with V being the volume of the cavity and γ_2 mean adiabatic index of the fluid inside the cavity. The last equality comes for $\gamma_2 = 4/3$ in the case of a relativistic plasma. The jet power involved is estimated as:

$$L_{kin} = \frac{E_{tot}}{t_{lobe}} \tag{5.5}$$

and the age of the cavity t_{lobe} is (Fabian et al., 2002; Birzan et al., 2004):

$$t_{lobe} = R_{lobe}/c_s \tag{5.6}$$

where R_{lobe} is the lobe radius and c_s is the adiabatic sound speed of the gas (on the scale of the cavity). The latter is expressed as $c_s = \sqrt{\gamma_2 kT/\mu m_p}$, with T gas temperature of the gas, m_p proton mass, $\mu = 0.62$ mean atomic weight.
In the assumption of equipartition between particles and magnetic field, we obtain an equipartition magnetic field $B_{eq} \sim 0.8 \times 10^6$ G, calculated using the flux at 178 MHz ($F_{178} = 11.6$ Jy) and assuming a spherical geometry for the lobe with $R_{lobe} = 230$ kpc (Evans et al. 2005). The total energy E_{tot} is then 3.5×10^{59} erg s^{-1}. The cavity age $t_{lobe} = 1.35 \times 10^{16}$ sec is calculated for the halo gas temperature kT of 1.7 keV (Evans et al. 2005). The resulting jet power is $L_{kin} \sim 2.6 \times 10^{43}$ erg s^{-1}. This value can be considered as a lower limit, as we have been conservative in the estimate of B_{eq}. In fact, we assumed a volume filling factor f and a factor k[4] equal to 1. For typical values used in literature $f = 0.1$ and $k = 100$, B_{eq} is amplified by a factor $(k/f)^{2/7} \sim 7.2$ and E_{tot}, as also the final L_{kin}, by a factor $(f/k)^{4/7} \sim 52$. Relaxing the assumptions on f and k, we then obtain a jet power of a few 10^{44} erg s^{-1}. In conclusion, both the applied methods give (maximum) jet kinetic powers in rough agreement with the ones derived from the SED modeling.

[4] k accounts for the additional energy in relativistic particles accompanying the electrons and any non-relativistic component.

5.5.2 Jet Power versus Accretion

The SED of NGC 6251 in the optical-UV band is dominated by the non-thermal emission of the jet. No sign of big blue bump is identified and there is no strong evidence in the X-ray spectrum of the Fe Kα emission line. The disk luminosity L_{disk} appears weak and can be assumed to be about a factor of 10 below the observed non-thermal luminosity.

The jet power dominance over the disk luminosity may imply either a radiatively inefficient disk (ADAF, see Narayan, 2002, for a review) or a low accretion flow. The second case requires then an alternative mechanism to power the jet, as could be rotational energy of the spinning black hole, the so called spin-paradigm (Blandford, 1990; Wilson and Colbert, 1995; Moderski and Sikora, 1996, among the others) based on the Blandford-Znajek mechanism (Blandford and Znajek, 1977).

It is possible to derive some constraints on the rate of accretion $\dot{M}$ of the central black hole. Under the assumption of spherical symmetry and negligible angular momentum, the accretion rate can be calculated as (Bondi, 1952):

$$\dot{M}_B \approx 7.3 \times 10^{-4} \left(\frac{M_{BH}}{10^8 M_\odot} \right)^2 \left(\frac{n}{0.1\ cm^{-3}} \right) \left(\frac{200\ km\ s^{-1}}{c_s} \right)^3 M_\odot\ year^{-1}. \quad (5.7)$$

Here we use the formula as given in Ho (2008): M_{BH} is the black hole mass, n is the particle density at the Bondi accretion radius, defined as $r_A = 2GM_{BH}/c_s^2$, with G gravitational constant and $c_s \approx 0.1T^{1/2}$ km s^{-1} sound speed of the gas, at r_A with a temperature T (in Kelvin). Ferrarese and Ford (1999) estimate the black hole mass in the range between $4 - 8 \times 10^8$ M$_\odot$. We adopt the intermediate value $M_{BH} = 6 \times 10^8$ M$_\odot$. The X-ray spectral analysis indicates the presence of thermal emission with a temperature $kT = 0.62$ keV. Typical densities in the central regions of elliptical galaxies are in the range $n \approx 0.1 - 0.5$ cm^{-3} (Di Matteo et al., 2001; Pellegrini, 2005). Here we set $n = 0.5$ cm^{-3} in consideration of the fact that densities are expected to be higher near to r_A (see also Allen et al., 2006; Balmaverde et al., 2008). With these values, the estimated Bondi accretion rate is $\dot{M}_B \sim 5 \times 10^{-2}$ M$_\odot$ year^{-1}. We note that the Bondi accretion rate estimated by Ferrarese and Ford (1999) is 2 order of magnitude below this value. The difference can be partly due to the lower values of n and T ($n = 0.1$ cm^{-3} and $kT = 0.5$ keV), but most likely to limits on the central pressure derived from ROSAT/PSPC observations (Birkinshaw and Worrall, 1993).

The maximum power released by the black hole is:

$$P_{Bondi} = \dot{M}_B c^2, \tag{5.8}$$

which gives $P_{Bondi} = 2.8 \times 10^{45}$ erg s^{-1}. In the ideal condition we have assumed, namely that all the gas crossing r_A accretes onto the black hole, Bondi accretion power is almost an order of magnitude greater than L_{kin}. According to this result, accretion is enough to explain the estimated jet powers. The mechanism converting accretion to jet power is very efficient ($\eta_{jet} \sim 10\%$). In comparison, the radiative efficiency of the disk is at least an order of magnitude lower. This is in line with recent findings for blazar sources (Ghisellini et al., 2010b, and references therein).

5.6 Summary

In this paper we presented a study of the broad band nuclear SED of the radio galaxy NGC 6251, one of the MAGNs detected by *Fermi* -LAT. In agreement with previous studies, the nuclear SED is dominated by non-thermal emission related to the sub-pc jet. The nuclear origin appears the most likely explanation for γ-ray emission. This is also supported by the results of the X-ray analysis of archival XMM-Newton, Chandra and Swift observations. Both the models, SSC and spine-layer, adopted to reproduce the observed SED, give a good overall fit. In the following we summarize the main results of the SED modeling:

- SSC model implies a slow and heavy jet. Particles dominate over the magnetic field ($\sim$3 orders of magnitude). This seems to rule out a magnetically accelerated and confined jet. The X-ray halo surrounding the jet can account for its confinement on kpc scales but leaves unsolved the issue in the core region. A low bulk Lorentz factor, when a SSC model is used, is shared also with other MAGNs detected by *Fermi* -LAT (Abdo, 2009; Abdo et al., 2009; Kataoka et al., 2010, and Abdo et al. on Cen A core), and is difficult to be reconciled with the Unified Model.

- The spine-layer model requires a structured jet, with a fast inner component which carries the bulk of the jet power. The jet is relatively light and could be magnetically confined. However, the strong radiative dissipation ($L_r \sim 0.3\, L_{kin}$) is at odds with the Mpc jet length. Also, the flux variability predicted by the model in the high energy band has not been yet observed.

- The derived jet powers are model dependent and rely on some important assumptions. However, similar values are derived using the 151 MHz luminosity (Willott et al. 1999).

- Accretion should supply enough power ($P_{Bondi} = 2.8 \times 10^{45}$ erg s^{-1}) to explain L_{kin}. The mechanism channeling power into the jet has to be very efficient ($\eta_{jet} \geqslant 10\%$). Conversely, the radiative efficiency of the disk is low and determines a weak disk, completely hidden by the jet emission.

Table 5.4. NGC6251 nuclear SED - Data

ν Hz	Flux Jy	errFlux Jy	Ref	Angular Resolution
408.90×10^6	< 0.3	0.0	1	3.7'x3.7'
14.070×10^8	0.36	0.0	1	
26.950×10^8	0.72	0.02	1	3.7'x3.7'
153.75×10^8	0.85	0.04	1	0.65"x 0.65"
1.6655×10^9	0.28	0	2	VLBI (¡3mas)
2.3×10^9	0.25	0	2	
4.9965×10^9	0.36	0	2	
2.3×10^9	0.65	0	3	VLBI (0.6mas)
1.07×10^{10}	0.9	9	3	
5×10^9	0.13	0	4	VLBA (0.5mas)
1.5×10^{10}	0.34	0	4	
3.4459×10^{11}	0.4233	0.011	5	23"
22.8×10^9	1.3	0.04	6	Wmap 0.88°
33.0×10^9	1.5	0.07	6	0.66°
40.7×10^9	1.5	0.08	6	0.51°
60.8×10^9	1.2	0.1	6	0.35°
93.5×10^9	0.7	0.3	6	0.22°
1.3×10^{13}	90×10^{-3}	20×10^{-3}	7	0.5-2'
2.0×10^{13}	27.88×10^{-3}	0	8	4-11" Total emiss
1.0×10^{13}	49.68×10^{-3}	0	8	4-11" Total emiss
2.0×10^{13}	8.1×10^{-3}	0	8	4-11" Syn emiss (29% Tot)
1.0×10^{13}	16.4×10^{-3}	0	8	4-11" Syn emiss (33% Tot)
1.42430×10^{14}	1.07847×10^{-3}	1.07847×10^{-4}	9	0.2" no Abs correction
1.84615×10^{14}	5.45183×10^{-4}	5.45183×10^{-5}	9	0.2"
2.54734×10^{14}	3.14067×10^{-4}	3.14067×10^{-5}	9	0.2"
3.69276×10^{14}	1.99998×10^{-4}	1.99998×10^{-5}	9	0.2"
5.39762×10^{14}	1.33729×10^{-4}	1.33729×10^{-5}	9	0.2"
5.45355×10^{14}	1.20923×10^{-4}	1.20923×10^{-5}	9	0.2"
8.73362×10^{14}	3.30048×10^{-5}	3.30048×10^{-6}	9	0.2"
1.24275×10^{15}	1.76588×10^{-5}	1.76588×10^{-6}	9	0.2"

References: 1 - Waggett et al. (1977); 2 - Jones et al. (1986); 3 - Cohen and Readhead (1979); 4 - Sudou and Taniguchi (2000); 5 - Quillen et al. (2003); 6 - Wright et al. (2009); 7- Knapp et al. (1990); 8 - Leipski et al. (2009); 9 - Chiaberge et al. (2003)

6

Summary and Conclusions

In the thesis, the high energy emission of extragalactic jets has been studied by modeling their spectral energy distribution. A simple synchrotron inverse Compton leptonic model has been assumed to describe the jet emission. In order to obtain a tool suitable to investigate the jet radiation under different conditions, we have included all the main components which could possibly contribute to the inverse Compton emission. The main local and external radiation fields have been defined following the prescription given by several studies (with particular reference to Ghisellini and Madau, 1996; Celotti et al., 2001; Ghisellini et al., 2005). The implications from the radiative point of view of a complex velocity structure have been also considered.

The model is used to address the problem of the origin of the X-ray emission in compact and young radio sources. The jet hypothesis has been tested first using a general approach and then on the specific case of the CSS quasar 3C 186.

In the general case, the energy density of the radiative fields relevant for the Compton emission has been evaluated as a function of the distance from the central black hole. Linear sizes and radio powers typical for GPS and CSS radio galaxies and quasars have been considered. Motivated by multiwavelength observations which suggest a similar nuclear environment for giant and young sources, standard IR to UV luminosities have been adopted to model the radiative field contributions.

The jet SED have been estimated for two different regimes of luminosity and jet bulk motion at selected distances from the central black hole and for increasing viewing angles. On the basis of the modeling results, the hypothesis of emission from a highly relativistic jet appears disfavored because of debeaming effects. Debeaming effects

might be stronger in compact radio galaxies than in quasars, which are supposed to lie at larger viewing angles than quasars. SSC emission from highly relativistic jets accounts only for the X-ray weakest compact quasars ($L_{2-10\ keV} \sim 10^{42}$ erg s^{-1}) at the minimum size considered (33 pc).

The X-ray luminosity ranges ($10^{41} \lesssim L_{2-10\ keV} \lesssim 10^{46}$ erg s^{-1}) observed in compact quasars and radio galaxies can be reproduced by more than one IC component in mildly relativistic jets, either with a low or a high radio power. In powerful sources, comptonization of the nuclear fields may be relevant most likely at GPS scales, while in low power cases a marginal contribution is given by comptonized starlight emission as long as the jet is moving in the galaxy core. However, these contributions may consistently explain only the low tail of the X-ray luminosity range.

X-ray SSC emission is still appreciable high and can be of the order of 10^{44} erg s^{-1} in powerful sources, however the most intense luminosity is obtained by scattering external synchrotron photons from a inner blazar-like component. In low power sources the presence of a velocity structure becomes a necessary condition to save the jet hypothesis in young sources.

To summarize, the emerging picture is that the observed X-ray emission can be easily ascribed to the jet only under the specific conditions of a structured jet. In absence of observational evidences is hard to give preference to this hypothesis with respect to the competing scenarios of accretion and non-thermal emission from the lobes (limited to the GPS radio galaxies). The jet model predicts also consistent gamma-ray luminosities ($L_{1GeV} \sim 10^{44} - 10^{45}$ erg s^{-1}).

The γ-ray detection of GPS and CSS sources by *Fermi* -LAT would certainly represent a turning point as thermal emission drops drastically in this energy band. We find that LAT flux sensitivity should allow the detection of sources located at $z \lesssim 0.5$. This could be challenging given the typical redshifts of X-ray detected GPS/CSS quasars ($0.5 < z < 2.0$).

The general results find further confirmation when the jet model is applied to the powerful CSS quasar 3C 186. The structured jet seems the only "non-thermal" viable solution to match the observed flux. However, the kinetic power required by the presence of the blazar-like component are rather high ($L_{kin} \sim 1.2 \times 10^{48}$ erg s^{-1}) and comparable to the most powerful blazars.

As a following step, we have performed a detailed study on NGC 6251, one of the misaligned AGN recently detected by *Fermi* -LAT. An environment that is not dense of external photons and the γ-ray detection that allows to constrain the high

energy tail of the emission make the source an ideal laboratory to better investigate the jet internal structure. Its broadband non-thermal nuclear continuum has been modeled with a SSC and a spine-layer model. Even though both the models can consistently reproduce the multiwavelength nuclear emission, the spine-layer model allows to reconcile the inferred velocities and intrinsic luminosities with the Unified Scheme of RL AGN and avoids the acceleration and confinement issues implied by the strongly particle dominated SSC jet. Critical points remain the non-detection of the predicted flux variability as also the high radiative dissipation with respect to the extraordinary jet length (Mpc scale).

It is worth mentioning that the spine-layer models have been preferentially investigated in the jets of FR I radio sources. The presence of transverse structures have been also detected in high power radio galaxies. Future perspectives concern the SED modeling of the FR II sources of the *Fermi* -LAT sample. This will provide a useful term of comparison with the class of the GPS and CSS sources, which are powerful by selection criteria. The study of the jet role in a class of low luminosity compact sources which display similar properties to FR I sources (Kunert-Bajraszewska and Thomasson, 2009; Baldi and Capetti, 2009) is a second direction of investigation.

Part I

Bibliography

Bibliography

Abdo, A. A., Harris, D. E., Massaro, F., and Stawarz, Ł. (2009). Fermi Large Area Telescope Gamma-Ray Detection of the Radio Galaxy M87. *ApJ*, 707:55–60.

Abdo, A. A. e. a. (2009). Fermi Discovery of Gamma-ray Emission from NGC 1275. *ApJ*, 699:31–39.

Acciari, V. A., Harris, D. E., and Massaro, F. (2010). Veritas 2008-2009 Monitoring of the Variable Gamma-ray Source M87. *ApJ*, 716:819–824.

Aharonian, F. e. (2003). Is the giant radio galaxy M 87 a TeV gamma-ray emitter? *A&A*, 403:L1–L5.

Allen, S. W., Dunn, R. J. H., Fabian, A. C., Taylor, G. B., and Reynolds, C. S. (2006). The relation between accretion rate and jet power in X-ray luminous elliptical galaxies. *MNRAS*, 372:21–30.

Antonucci, R. (1993). Unified models for active galactic nuclei and quasars. *ARA&A*, 31:473–521.

Atoyan, A. M. and Dermer, C. D. (2003). Neutral Beams from Blazar Jets. *ApJ*, 586:79–96.

Atwood, W. B. and Abdo, A. A. e. a. (2009). The Large Area Telescope on the Fermi Gamma-Ray Space Telescope Mission. *ApJ*, 697:1071–1102.

Axon, D. J., Capetti, A., Fanti, R., Morganti, R., Robinson, A., and Spencer, R. (2000). The Morphology of the Emission-Line Region Of Compact Steep-Spectrum Radio Sources. *AJ*, 120:2284–2299.

Baldi, R. D. and Capetti, A. (2009). Radio and spectroscopic properties of miniature radio galaxies: revealing the bulk of the radio-loud AGN population. *A&A*, 508:603–614.

Balmaverde, B., Baldi, R. D., and Capetti, A. (2008). The accretion mechanism in low-power radio galaxies. *A&A*, 486:119–130.

Baum, S. A., O'Dea, C. P., Murphy, D. W., and de Bruyn, A. G. (1990). 0108 + 388 - A compact double source with surprising properties. *A&A*, 232:19–26.

Bechtold, J., Elvis, M., Fiore, F., Kuhn, O., Cutri, R. M., McDowell, J. C., Rieke, M., Siemiginowska, A., and Wilkes, B. J. (1994a). Infrared to x-ray spectral energy distributions of high redshift quasars. *AJ*, 108:374–394.

Bechtold, J., Elvis, M., Fiore, F., Kuhn, O., Cutri, R. M., McDowell, J. C., Rieke, M., Siemiginowska, A., and Wilkes, B. J. (1994b). X-ray spectral evolution of high redshift quasars. *AJ*, 108:759–765.

Begelman, M. C., Blandford, R. D., and Rees, M. J. (1984). Theory of extragalactic radio sources. *Reviews of Modern Physics*, 56:255–351.

Bell, A. R. (1978). The acceleration of cosmic rays in shock fronts. I. *MNRAS*, 182:147–156.

Belsole, E., Worrall, D. M., and Hardcastle, M. J. (2006). High-redshift Faranoff-Riley type II radio galaxies: X-ray properties of the cores. *MNRAS*, 366:339–352.

Bicknell, G. V. (1995). Relativistic Jets and the Fanaroff-Riley Classification of Radio Galaxies. *ApJS*, 101:29–+.

Bicknell, G. V. and Sutherland, R. S. (2006). Evolutionary models of powerful radio galaxies. *Astronomische Nachrichten*, 327:235–240.

Birkinshaw, M. and Worrall, D. M. (1993). The X-ray structure and spectrum of NGC 6251. *ApJ*, 412:568–585.

Birzan, L., Rafferty, D. A., McNamara, B. R., Wise, M. W., and Nulsen, P. E. J. (2004). A Systematic Study of Radio-induced X-Ray Cavities in Clusters, Groups, and Galaxies. *ApJ*, 607:800–809.

Blandford, R. D. (1990). Physical processes in active galactic nuclei. In R. D. Blandford, H. Netzer, L. Woltjer, T. J.-L. Courvoisier, & M. Mayor, editor, *Active Galactic Nuclei*, pages 161–275.

Blandford, R. D. and Ostriker, J. P. (1978). Particle acceleration by astrophysical shocks. *ApJL*, 221:L29–L32.

Blandford, R. D. and Payne, D. G. (1982). Hydromagnetic flows from accretion discs and the production of radio jets. *MNRAS*, 199:883–903.

Blandford, R. D. and Rees, M. J. (1974). A 'twin-exhaust' model for double radio sources. *MNRAS*, 169:395–415.

Blandford, R. D. and Znajek, R. L. (1977). Electromagnetic extraction of energy from Kerr black holes. *MNRAS*, 179:433–456.

Błażejowski, M., Siemiginowska, A., Sikora, M., Moderski, R., and Bechtold, J. (2004). X-Ray Emission from the Quasar PKS 1127-145: Comptonized Infrared Photons on Parsec Scales. *ApJL*, 600:L27–L30.

Bodo, G., Rossi, P., Mignone, A., Massaglia, S., and Ferrari, A. (2003). Deceleration of relativistic jets. , 47:557–559.

Bondi, H. (1952). On spherically symmetrical accretion. *MNRAS*, 112:195–+.

Capetti, A. and Celotti, A. (1999). Testing the FR I/BL Lac unifying model with HST observations. *MNRAS*, 304:434–442.

Capetti, A., Celotti, A., Chiaberge, M., de Ruiter, H. R., Fanti, R., Morganti, R., and Parma, P. (2002). The HST survey of the B2 sample of radio-galaxies: Optical nuclei and the FR I/BL Lac unified scheme. *A&A*, 383:104–111.

Capetti, A., Fanti, R., and Parma, P. (1995). Radio galaxies of intermediate radio luminosity: a discussion of the radio properties of B2 0836+29, B2 0844+31 and B2 1521+28. *A&A*, 300:643–+.

Carballo, R., Sánchez, S. F., González-Serrano, J. I., Benn, C. R., and Vigotti, M. (1998). K-Band Imaging of 52 B3-VLA Quasars: Nucleus and Host Properties. *AJ*, 115:1234–1252.

Cardelli, J. A., Clayton, G. C., and Mathis, J. S. (1989). The relationship between infrared, optical, and ultraviolet extinction. *ApJ*, 345:245–256.

Cawthorne, T. V., Scheuer, P. A. G., Morison, I., and Muxlow, T. W. B. (1986). A sample of powerful radio sources for VLBI studies. *MNRAS*, 219:883–893.

Celotti, A. and Fabian, A. C. (1993). The Kinetic Power and Luminosity of Parsecscale Radio Jets - an Argument for Heavy Jets. *MNRAS*, 264:228–+.

Celotti, A. and Ghisellini, G. (2008). The power of blazar jets. *MNRAS*, 385:283–300.

Celotti, A., Ghisellini, G., and Chiaberge, M. (2001). Large-scale jets in active galactic nuclei: multiwavelength mapping. *MNRAS*, 321:L1–L5.

Chiaberge, M., Capetti, A., and Celotti, A. (1999). The HST view of FR I radio galaxies: evidence for non-thermal nuclear sources. *A&A*, 349:77–87.

Chiaberge, M., Capetti, A., and Celotti, A. (2000). The HST view of the FR I / FR II dichotomy. *A&A*, 355:873–879.

Chiaberge, M., Capetti, A., and Celotti, A. (2001). The BL Lac heart of Centaurus A. *MNRAS*, 324:L33–L37.

Chiaberge, M., Gilli, R., Capetti, A., and Macchetto, F. D. (2003). The Nuclear Spectral Energy Distribution of NGC 6251: A BL Lacertae Object in the Center of an FR I Radio Galaxy. *ApJ*, 597:166–174.

Cohen, M. H. and Readhead, A. C. S. (1979). Misalignment in the radio jets of NGC 6251. *ApJL*, 233:L101–L104.

Czerny, B., Siemiginowska, A., Janiuk, A., Nikiel-Wroczyński, B., and Stawarz, Ł. (2009). Accretion Disk Model of Short-Timescale Intermittent Activity in Young Radio Sources. *ApJ*, 698:840–851.

Dermer, C. D. (1995). On the Beaming Statistics of Gamma-Ray Sources. *ApJL*, 446:L63+.

Dermer, C. D. and Schlickeiser, R. (1993). Model for the High-Energy Emission from Blazars. *ApJ*, 416:458–+.

Di Matteo, T., Carilli, C. L., and Fabian, A. C. (2001). Limits on the Accretion Rates onto Massive Black Holes in Nearby Galaxies. *ApJ*, 547:731–739.

Elvis, M., Fiore, F., Wilkes, B., McDowell, J., and Bechtold, J. (1994). Absorption in X-ray spectra of high-redshift quasars. *ApJ*, 422:60–72.

Evans, D. A., Hardcastle, M. J., Croston, J. H., Worrall, D. M., and Birkinshaw, M. (2005). Chandra and XMM-Newton observations of NGC 6251. *MNRAS*, 359:363–382.

Evans, I. N. and Koratkar, A. P. (2004). A Complete Atlas of Recalibrated Hubble Space Telescope Faint Object Spectrograph Spectra of Active Galactic Nuclei and Quasars. I. Pre-COSTAR Spectra. *ApJS*, 150:73–164.

Fabian, A. C. (2006). A short introduction to broad and variable iron lines around black holes. *Astronomische Nachrichten*, 327:943–+.

Fabian, A. C., Celotti, A., Blundell, K. M., Kassim, N. E., and Perley, R. A. (2002). The properties of the X-ray holes in the intracluster medium of the Perseus cluster. *MNRAS*, 331:369–375.

Falcke, H. and Biermann, P. L. (1995). The jet-disk symbiosis. I. Radio to X-ray emission models for quasars. *A&A*, 293:665–682.

Fanaroff, B. L. and Riley, J. M. (1974). The morphology of extragalactic radio sources of high and low luminosity. *MNRAS*, 167:31P–36P.

Fermi-LAT Collaboration (2010). Fermi Large Area Telescope Observations of Misaligned AGN. *ApJ*, 720:912–922.

Fermi-LAT Collaboration Abdo, A. A. e. a. (2010). Fermi Gamma-Ray Imaging of a Radio Galaxy. *Science*, 328:725–.

Ferrarese, L. and Ford, H. C. (1999). Nuclear Disks of Gas and Dust in Early-Type Galaxies and the Hunt for Massive Black Holes: Hubble Space Telescope Observations of NGC 6251. *ApJ*, 515:583–602.

Ferrari, A. (1998). Modeling Extragalactic Jets. *ARA&A*, 36:539–598.

Foschini, L., Chiaberge, M., Grandi, P., Grenier, I. A., Guainazzi, M., Hermsen, W., Palumbo, G. G. C., Rodriguez, J., Chaty, S., Corbel, S., Di Cocco, G., Kuiper, L., and Malaguti, G. (2005). Investigating the EGRET-radio galaxies link with INTEGRAL: The case of 3EG J1621+8203 and NGC 6251. *A&A*, 433:515–518.

Freeman, P., Doe, S., and Siemiginowska, A. (2001). Sherpa: a mission-independent data analysis application. In J.-L. Starck & F. D. Murtagh, editor, *Society of Photo-Optical Instrumentation Engineers (SPIE) Conference Series*, volume 4477 of *Society of Photo-Optical Instrumentation Engineers (SPIE) Conference Series*, pages 76–87.

Georganopoulos, M. and Kazanas, D. (2003). Decelerating Flows in TeV Blazars: A Resolution to the BL Lacertae-FR I Unification Problem. *ApJL*, 594:L27–L30.

Ghisellini, G. (2010). The jet/disk connection in blazars. In G. Bertin, F. de Luca, G. Lodato, R. Pozzoli, & M. Romé , editor, *American Institute of Physics Conference Series*, volume 1242 of *American Institute of Physics Conference Series*, pages 43–54.

Ghisellini, G. and Madau, P. (1996). On the origin of the gamma-ray emission in blazars. *MNRAS*, 280:67–76.

Ghisellini, G. and Tavecchio, F. (2009). Canonical high-power blazars. *MNRAS*, 397:985–1002.

Ghisellini, G., Tavecchio, F., and Chiaberge, M. (2005). Structured jets in TeV BL Lac objects and radiogalaxies. Implications for the observed properties. *A&A*, 432:401–410.

Ghisellini, G., Tavecchio, F., Foschini, L., Ghirlanda, G., Maraschi, L., and Celotti, A. (2010a). General physical properties of bright Fermi blazars. *MNRAS*, 402:497–518.

Ghisellini, G., Tavecchio, F., Foschini, L., Ghirlanda, G., Maraschi, L., and Celotti, A. (2010b). General physical properties of bright Fermi blazars. *MNRAS*, 402:497–518.

Ghisellini, G., Tavecchio, F., and Ghirlanda, G. (2009). Jet and accretion power in the most powerful Fermi blazars. *MNRAS*, 399:2041–2054.

Giovannini, G., Casadio, C., Giroletti, M., Beilicke, M., Cesarini, A., and Krawczynski, H. (2010). The Jet in M87 from e-EVN Observations. *ArXiv e-prints*.

Giovannini, G., Cotton, W. D., Feretti, L., Lara, L., and Venturi, T. (2001a). VLBI Observations of a Complete Sample of Radio Galaxies: 10 Years Later. *ApJ*, 552:508–526.

Giovannini, G., Cotton, W. D., Feretti, L., Lara, L., and Venturi, T. (2001b). VLBI Observations of a Complete Sample of Radio Galaxies: 10 Years Later. *ApJ*, 552:508–526.

Giovannini, G., Feretti, L., Venturi, T., Lara, L., Marcaide, J., Rioja, M., Spangler, S. R., and Wehrle, A. E. (1994). VLBI observations of a complete sample of radio galaxies. IV: The radio galaxies NGC 2484, 3C 109, and 3C 382. *ApJ*, 435:116–127.

Giroletti, M., Giovannini, G., Feretti, L., Cotton, W. D., Edwards, P. G., Lara, L., Marscher, A. P., Mattox, J. R., Piner, B. G., and Venturi, T. (2004). Parsec-Scale Properties of Markarian 501. *ApJ*, 600:127–140.

Gliozzi, M., Sambruna, R. M., Brandt, W. N., Mushotzky, R., and Eracleous, M. (2004). The XMM-Newton view of ¡ASTROBJ¿NGC 6251¡/ASTROBJ¿. *A&A*, 413:139–144.

Govoni, F., Falomo, R., Fasano, G., and Scarpa, R. (2000). The optical properties of low redshift radio galaxies. *A&A*, 353:507–527.

Grandi, P., Malaguti, G., and Fiocchi, M. (2006). BeppoSAX View of Radio-loud Active Galactic Nuclei. *ApJ*, 642:113–125.

Guainazzi, M., Grandi, P., Comastri, A., and Matt, G. (2003). The hard X-ray view of the low-luminosity blazar in the radio galaxy NGC 6251. *A&A*, 410:131–138.

Guainazzi, M., Siemiginowska, A., Rodriguez-Pascual, P., and Stanghellini, C. (2004). XMM-Newton discovery of a Compton-thick AGN in the GPS galaxy Mkn 668. *A&A*, 421:461–471.

Guainazzi, M., Siemiginowska, A., Stanghellini, C., Grandi, P., Piconcelli, E., and Azubike Ugwoke, C. (2006). A hard X-ray view of giga-hertz peaked spectrum radio galaxies. *A&A*, 446:87–96.

Gupta, N., Salter, C. J., Saikia, D. J., Ghosh, T., and Jeyakumar, S. (2006). Probing radio source environments via HI and OH absorption. *MNRAS*, 373:972–992.

Haardt, F., Maraschi, L., and Ghisellini, G. (1994). A model for the X-ray and ultraviolet emission from Seyfert galaxies and galactic black holes. *ApJL*, 432:L95–L99.

Haas, M., Willner, S. P., Heymann, F., Ashby, M. L. N., Fazio, G. G., Wilkes, B. J., Chini, R., and Siebenmorgen, R. (2008). Near- and Mid-Infrared Photometry of High-Redshift 3CR Sources. *ApJ*, 688:122–127.

Harris, D. E. and Krawczynski, H. (2006). X-Ray Emission from Extragalactic Jets. *ARA&A*, 44:463–506.

Ho, L. C. (2008). Nuclear Activity in Nearby Galaxies. *ARA&A*, 46:475–539.

Hovatta, T., Valtaoja, E., Tornikoski, M., and Lähteenmäki, A. (2009). Doppler factors, Lorentz factors and viewing angles for quasars, BL Lacertae objects and radio galaxies. *A&A*, 494:527–537.

Jones, D. L., Unwin, S. C., Readhead, A. C. S., Sargent, W. L. W., Seielstad, G. A., Simon, R. S., Walker, R. C., Benson, J. M., Perley, R. A., Bridle, A. H., Pauliny-Toth, I. I. K., Romney, J., Witzel, A., Wilkinson, P. N., Baath, L. B., Booth, R. S., Fort, D. N., Galt, J. A., Mutel, R. L., and Linfield, R. P. (1986). High dynamic range VLBI observations of NGC 6251. *ApJ*, 305:684–697.

Jones, D. L. and Wehrle, A. E. (1994). Morphological changes in the NGC 6251 jet. *ApJ*, 427:221–226.

Jones, D. L. and Wehrle, A. E. (2002). What Happened to the NGC 6251 Counterjet? *ApJ*, 580:114–121.

Kataoka, J., Stawarz, Ł., Cheung, C. C., Tosti, G., Cavazzuti, E., Celotti, A., Nishino, S., Fukazawa, Y., Thompson, D. J., and McConville, W. F. (2010). Gamma-ray Spectral Evolution of NGC 1275 Observed with Fermi Large Area Telescope. *ApJ*, 715:554–560.

Katz-Stone, D. M. and Rudnick, L. (1997). A Spectral Analysis of Two Compact Steep-Spectrum Sources. *ApJ*, 479:258–+.

Kellermann, K. I., Lister, M. L., Homan, D. C., Vermeulen, R. C., Cohen, M. H., Ros, E., Kadler, M., Zensus, J. A., and Kovalev, Y. Y. (2004). Sub-Milliarcsecond Imaging of Quasars and Active Galactic Nuclei. III. Kinematics of Parsec-scale Radio Jets. *ApJ*, 609:539–563.

Kellermann, K. I., Sramek, R., Schmidt, M., Shaffer, D. B., and Green, R. (1989). VLA observations of objects in the Palomar Bright Quasar Survey. *AJ*, 98:1195–1207.

Kerp, J. and Mack, K. (2003). Chandra's view of the X-ray jet and halo of the giant radio galaxy NGC 6251. *New Astronomy Review*, 47:447–449.

Kirk, J. G. and Duffy, P. (1999). TOPICAL REVIEW: Particle acceleration and relativistic shocks. *Journal of Physics G Nuclear Physics*, 25:163–+.

Knapp, G. R., Bies, W. E., and van Gorkom, J. H. (1990). Infrared properties of nearby radio galaxies. *AJ*, 99:476–496.

Komissarov, S. S. (1994). Ram-Pressure Confinement of Extragalactic Jets. *MNRAS*, 266:649–+.

Koratkar, A. and Blaes, O. (1999). The Ultraviolet and Optical Continuum Emission in Active Galactic Nuclei: The Status of Accretion Disks. *Publ. Astr. Soc. Pac.*, 111:1–30.

Kunert-Bajraszewska, M. and Thomasson, P. (2009). A survey of Low Luminosity Compact sources. *Astronomische Nachrichten*, 330:210–+.

Kuraszkiewicz, J. K., Green, P. J., Forster, K., Aldcroft, T. L., Evans, I. N., and Koratkar, A. (2002). Emission Line Properties of Active Galactic Nuclei from a pre-COSTAR Faint Object Spectrograph Hubble Space Telescope Spectral Atlas. *ApJS*, 143:257–276.

Laing, R. A. and Bridle, A. H. (1987). Rotation measure variation across M84. *MNRAS*, 228:557–571.

Laing, R. A. and Bridle, A. H. (2002). Dynamical models for jet deceleration in the radio galaxy 3C 31. *MNRAS*, 336:1161–1180.

Laing, R. A., Canvin, J. R., and Bridle, A. H. (2003). The physics of jets in FR I radio galaxies. , 47:577–579.

Laing, R. A., Parma, P., de Ruiter, H. R., and Fanti, R. (1999). Asymmetries in the jets of weak radio galaxies. *MNRAS*, 306:513–530.

Leahy, J. P. and Perley, R. A. (1991). VLA images of 23 extragalactic radio sources. *AJ*, 102:537–561.

Leipski, C., Antonucci, R., Ogle, P., and Whysong, D. (2009). The Spitzer View of FR I Radio Galaxies: On the Origin of the Nuclear Mid-Infrared Continuum. *ApJ*, 701:891–914.

Leipski, C., Haas, M., Willner, S. P., Ashby, M. L. N., Wilkes, B. J., Fazio, G. G., Antonucci, R., Barthel, P., Chini, R., Siebenmorgen, R., Ogle, P., and Heymann, F. (2010). Mid-infrared Spectroscopy of High-redshift 3CRR Sources. *ApJ*, 717:766–775.

Liang, E. P. T. and Price, R. H. (1977). Accretion disk coronae and Cygnus X-1. *ApJ*, 218:247–252.

Ludke, E., Garrington, S. T., Spencer, R. E., Akujor, C. E., Muxlow, T. W. B., Sanghera, H. S., and Fanti, C. (1998). MERLIN polarization observations of compact steep-spectrum sources at 5 GHz. *MNRAS*, 299:467–478.

Mack, K., Kerp, J., and Klein, U. (1997). The X-ray jet and halo of NGC 6251. *A&A*, 324:870–876.

Marscher, A. P. (1980). Flat-spectrum radio sources: victims of a conspiracy? *Nature*, 288:12–13.

McNamara, B. R. and Nulsen, P. E. J. (2007). Heating Hot Atmospheres with Active Galactic Nuclei. *ARA&A*, 45:117–175.

Middelberg, E., Roy, A. L., Nagar, N. M., Krichbaum, T. P., Norris, R. P., Wilson, A. S., Falcke, H., Colbert, E. J. M., Witzel, A., and Fricke, K. J. (2004). Motion and properties of nuclear radio components in Seyfert galaxies seen with VLBI. *A&A*, 417:925–944.

Moderski, R. and Sikora, M. (1996). On black hole evolution in active galactic nuclei. *MNRAS*, 283:854–864.

Mor, R., Netzer, H., and Elitzur, M. (2009). Dusty Structure Around Type-I Active Galactic Nuclei: Clumpy Torus Narrow-line Region and Near-nucleus Hot Dust. *ApJ*, 705:298–313.

Mukherjee, R., Halpern, J., Mirabal, N., and Gotthelf, E. V. (2002). Is the EGRET Source 3EG J1621+8203 the Radio Galaxy NGC 6251? *ApJ*, 574:693–700.

Murgia, M., Fanti, C., Fanti, R., Gregorini, L., Klein, U., Mack, K., and Vigotti, M. (1999). Synchrotron spectra and ages of compact steep spectrum radio sources. *A&A*, 345:769–777.

Mushotzky, R. F., Done, C., and Pounds, K. A. (1993). X-ray spectra and time variability of active galactic nuclei. *ARA&A*, 31:717–761.

Nan, R., Schilizzi, R. T., Fanti, C., and Fanti, R. (1991). VLBI observations of 24 3CR CSS radio sources at 50 CM. *A&A*, 252:513–527.

Narayan, R. (2002). Why Do AGN Lighthouses Switch Off? In M. Gilfanov, R. Sunyeav, & E. Churazov, editor, *Lighthouses of the Universe: The Most Luminous Celestial Objects and Their Use for Cosmology*, pages 405–+.

Nelder, J. A. and Mead, R. (1965). A simplex method for function minimization. *Computer Journal*, 7:308–313.

Netzer, H., Heller, A., Loinger, F., Alexander, T., Baldwin, J. A., Wills, B. J., Han, M., Frueh, M., and Higdon, J. L. (1996). Optical monitoring of luminous AGN - I. Radio-loud quasars. *MNRAS*, 279:429–446.

O'Dea, C. P. (1998). The Compact Steep-Spectrum and Gigahertz Peaked-Spectrum Radio Sources. *Publ. Astr. Soc. Pac.*, 110:493–532.

Orienti, M. and Dallacasa, D. (2008). Are young radio sources in equipartition? *A&A*, 487:885–894.

Osterbrok, D. E. and Ferland, G. J. (2006). *Astrophysics of Gaseous Nebulae and Active Galactic Nuclei*. University Science Books.

Ostorero, L., Moderski, R., Stawarz, Ł., Diaferio, A., Kowalska, I., Cheung, C. C., Kataoka, J., Begelman, M. C., and Wagner, S. J. (2010). X-ray-emitting GHz-peaked-spectrum Galaxies: Testing a Dynamical-Radiative Model with Broadband Spectra. *ApJ*, 715:1071–1093.

Owen, F. N., Ledlow, M. J., and Keel, W. C. (1996). Optical Spectroscopy of Radio Galaxies in Abell Clusters II. BL Lacs and FR I Unification. *AJ*, 111:53–+.

Owsianik, I. and Conway, J. E. (1998). First detection of hotspot advance in a Compact Symmetric Object. Evidence for a class of very young extragalactic radio sources. *A&A*, 337:69–79.

Pellegrini, S. (2005). The X-ray emission properties and the dichotomy in the central stellar cusp shapes of early-type galaxies. *MNRAS*, 364:169–178.

Perley, R. A., Bridle, A. H., and Willis, A. G. (1984). High-resolution VLA observations of the radio jet in NGC 6251. *ApJS*, 54:291–334.

Polatidis, A. G. and Conway, J. E. (2003). Proper Motions in Compact Symmetric Objects. *Publications of the Astronomical Society of Australia*, 20:69–74.

Prestage, R. M. and Peacock, J. A. (1988). The cluster environments of powerful radio galaxies. *MNRAS*, 230:131–160.

Quillen, A. C., Almog, J., and Yukita, M. (2003). 870 Micron Observations of Nearby 3CRR Radio Galaxies. *AJ*, 126:2677–2686.

Rawlings, S. and Saunders, R. (1991). Evidence for a common central-engine mechanism in all extragalactic radio sources. *Nature*, 349:138–140.

Rees, M. J. (1971). New Interpretation of Extragalactic Radio Sources. *Nature*, 229:312–317.

Rees, M. J. (1984). Black Hole Models for Active Galactic Nuclei. *ARA&A*, 22:471–506.

Reynolds, C. S. and Begelman, M. C. (1997). Intermittant Radio Galaxies and Source Statistics. *ApJL*, 487:L135+.

Reynolds, C. S., Heinz, S., and Begelman, M. C. (2001). Shocks and Sonic Booms in the Intracluster Medium: X-Ray Shells and Radio Galaxy Activity. *ApJL*, 549:L179–L182.

Reynolds, C. S. and Nowak, M. A. (2003). Fluorescent iron lines as a probe of astrophysical black hole systems. *Phys. Rep.*, 377:389–466.

Sambruna, R. M., Gambill, J. K., Maraschi, L., Tavecchio, F., Cerutti, R., Cheung, C. C., Urry, C. M., and Chartas, G. (2004a). A Survey of Extended Radio Jets with Chandra and the Hubble Space Telescope. *ApJ*, 608:698–720.

Sambruna, R. M., Gliozzi, M., Donato, D., Tavecchio, F., Cheung, C. C., and Mushotzky, R. F. (2004b). The XMM-Newton view of the X-ray halo and jet of NGC 6251. *A&A*, 414:885–894.

Sauty, C., Trussoni, E., and Tsinganos, K. (2002). Nonradial and nonpolytropic astrophysical outflows. V. Acceleration and collimation of self-similar winds. *A&A*, 389:1068–1085.

Scarpa, R. and Urry, C. M. (2001). On The Parent Population of Radio Galaxies and the FR I-FR II Dichotomy. *ApJ*, 556:749–755.

Scheuer, P. A. G. (1974). Models of extragalactic radio sources with a continuous energy supply from a central object. *MNRAS*, 166:513–528.

Shakura, N. I. and Sunyaev, R. A. (1973). Black holes in binary systems. Observational appearance. *A&A*, 24:337–355.

Siemiginowska, A., Aldcroft, T. L., Burke, D., Bechtold, J., Cheung, C. C., Lamassa, S., and Worrall, D. M. (2008a). Evolution of a Powerful Radio Loud Quasar 3C 186 and its Impact on the Cluster Environment at z=1. In T. A. Rector & D. S. De Young, editor, *Extragalactic Jets: Theory and Observation from Radio to Gamma Ray*, volume 386 of *Astronomical Society of the Pacific Conference Series*, pages 350–+.

Siemiginowska, A., Burke, D. J., Aldcroft, T. L., Worrall, D. M., Allen, S., Bechtold, J., Clarke, T., and Cheung, C. C. (2010). High redshift X-ray cooling-core cluster associated with the luminous radio loud quasar 3C186. *ArXiv e-prints*.

Siemiginowska, A., Cheung, C. C., LaMassa, S., Burke, D. J., Aldcroft, T. L., Bechtold, J., Elvis, M., and Worrall, D. M. (2005). X-Ray Cluster Associated with the z = 1.063 CSS Quasar 3C 186: The Jet is Not Frustrated. *ApJ*, 632:110–121.

Siemiginowska, A., LaMassa, S., Aldcroft, T. L., Bechtold, J., and Elvis, M. (2008b). X-Ray Properties of the Gigahertz Peaked and Compact Steep Spectrum Sources. *ApJ*, 684:811–821.

Sikora, M., Begelman, M. C., and Rees, M. J. (1994). Comptonization of diffuse ambient radiation by a relativistic jet: The source of gamma rays from blazars? *ApJ*, 421:153–162.

Sikora, M., Błażejowski, M., Moderski, R., and Madejski, G. M. (2002). On the Nature of MeV Blazars. *ApJ*, 577:78–84.

Sikora, M., Sol, H., Begelman, M. C., and Madejski, G. (1996a). Propagation of relativistic jets through dense radiation fields in AGN. *A&A Supp.*, 120:C579+.

Sikora, M., Sol, H., Begelman, M. C., and Madejski, G. M. (1996b). Radiation drag in relativistic active galactic nucleus jets. *MNRAS*, 280:781–796.

Sikora, M., Stawarz, Ł., and Lasota, J. (2007). Radio Loudness of Active Galactic Nuclei: Observational Facts and Theoretical Implications. *ApJ*, 658:815–828.

Simpson, C. and Rawlings, S. (2000). Infrared photometry of z˜1 3C quasars. *MNRAS*, 317:1023–1028.

Sokolovsky, K. V., Kovalev, Y. Y., Lobanov, A. P., Finke, J. D., Savolainen, T., Pushkarev, A. B., Kadler, M., Schinzel, F. K., Chavushyan, V. H., Carrasco, L., Carraminana, A., and Gurwell, M. A. (2010). Constraints on the gamma-ray emitting region in blazars from multi-frequency VLBI measurements. *ArXiv e-prints*.

Spencer, R. E., Schilizzi, R. T., Fanti, C., Fanti, R., Parma, P., van Breugel, W. J. M., Venturi, T., Muxlow, T. W. B., and Rendong, N. (1991). High-resolution observations of eight 3CR compact steep-spectrum radio sources. *MNRAS*, 250:225–240.

Stawarz, Ł., Ostorero, L., Begelman, M. C., Moderski, R., Kataoka, J., and Wagner, S. (2008). Evolution of and High-Energy Emission from GHz-Peaked Spectrum Sources. *ApJ*, 680:911–925.

Stawarz, Ł. and Ostrowski, M. (2002). Radiation from the Relativistic Jet: A Role of the Shear Boundary Layer. *ApJ*, 578:763–774.

Steinle, H., Bennett, K., Bloemen, H., Collmar, W., Diehl, R., Hermsen, W., Lichti, G. G., Morris, D., Schonfelder, V., Strong, A. W., and Williams, O. R. (1998). COMPTEL observations of Centaurus A at MeV energies in the years 1991 to 1995. *A&A*, 330:97–107.

Sudou, H. and Taniguchi, Y. (2000). Large-Scale Regular Morphological Patterns in the Radio Jet of NGC 6251. *AJ*, 120:697–702.

Swain, M. R., Bridle, A. H., and Baum, S. A. (1998). Internal Structure of the Jets in 3C 353. *ApJL*, 507:L29–L33.

Tavecchio, F. and Ghisellini, G. (2008). Structured jets and VHE emission of blazars and radiogalaxies. In F. A. Aharonian, W. Hofmann, & F. Rieger, editor, *American Institute of Physics Conference Series*, volume 1085 of *American Institute of Physics Conference Series*, pages 431–434.

Tavecchio, F., Ghisellini, G., Ghirlanda, G., Foschini, L., and Maraschi, L. (2010). TeV BL Lac objects at the dawn of the Fermi era. *MNRAS*, 401:1570–1586.

Tavecchio, F., Maraschi, L., Sambruna, R. M., and Urry, C. M. (2000). The X-Ray Jet of PKS 0637-752: Inverse Compton Radiation from the Cosmic Microwave Background? *ApJL*, 544:L23–L26.

Tengstrand, O., Guainazzi, M., Siemiginowska, A., Fonseca Bonilla, N., Labiano, A., Worrall, D. M., Grandi, P., and Piconcelli, E. (2009). The X-ray view of giga-hertz peaked spectrum radio galaxies. *A&A*, 501:89–102.

Turner, T. J., George, I. M., Nandra, K., and Mushotzky, R. F. (1997). ASCA Observations of Type 2 Seyfert Galaxies. I. Data Analysis Results. *ApJS*, 113:23–+.

Ulvestad, J. S. (2003). VLBI Imaging of Seyfert Galaxies. In J. A. Zensus, M. H. Cohen, & E. Ros, editor, *Radio Astronomy at the Fringe*, volume 300 of *Astronomical Society of the Pacific Conference Series*, pages 97–+.

Urry, C. M. and Padovani, P. (1995). Unified Schemes for Radio-Loud Active Galactic Nuclei. *Publ. Astr. Soc. Pac.*, 107:803–+.

Urry, C. M. and Shafer, R. A. (1984). Luminosity enhancement in relativistic jets and altered luminosity functions for beamed objects. *ApJ*, 280:569–573.

van Breugel, W., Miley, G., and Heckman, T. (1984). Studies of kiloparsec-scale, steep-spectrum radio cores. I VLA maps. *AJ*, 89:5–22.

van Breugel, W. J. M., Fanti, C., Fanti, R., Stanghellini, C., Schilizzi, R. T., and Spencer, R. E. (1992). Compact steep-spectrum 3 CR sources - VLA observations at 1.5, 15 and 22.5 GHz. *A&A*, 256:56–78.

Verdoes Kleijn, G. A., Baum, S. A., de Zeeuw, P. T., and O'Dea, C. P. (2002). Core Radio and Optical Emission in the Nuclei of nearby FR I Radio Galaxies. *AJ*, 123:1334–1356.

Vink, J., Snellen, I., Mack, K., and Schilizzi, R. (2006). The X-ray properties of young radio-loud AGN. *MNRAS*, 367:928–936.

Waggett, P. C., Warner, P. J., and Baldwin, J. E. (1977). NGC 6251, a very large radio galaxy with an exceptional jet. *MNRAS*, 181:465–474.

Weisskopf, M. C., Brinkman, B., Canizares, C., Garmire, G., Murray, S., and Van Speybroeck, L. P. (2002). An Overview of the Performance and Scientific Results from the Chandra X-Ray Observatory. *Publ. Astr. Soc. Pac.*, 114:1–24.

Willott, C. J., Rawlings, S., Blundell, K. M., and Lacy, M. (1999). The emission line-radio correlation for radio sources using the 7C Redshift Survey. *MNRAS*, 309:1017–1033.

Wilson, A. S. and Colbert, E. J. M. (1995). The difference between radio-loud and radio-quiet active galaxies. *ApJ*, 438:62–71.

Worrall, D. M. (2009). The X-ray jets of active galaxies. *A&A Rev.*, 17:1–46.

Worrall, D. M., Birkinshaw, M., and Cameron, R. A. (1995). The X-Ray Environment of the Dumbbell Radio Galaxy NGC 326. *ApJ*, 449:93–+.

Worrall, D. M., Birkinshaw, M., and Hardcastle, M. J. (2001). Chandra finds that X-ray jets are common in low-power radio galaxies. *MNRAS*, 326:L7–L12.

Worrall, D. M., Hardcastle, M. J., Pearson, T. J., and Readhead, A. C. S. (2004). The relationship between the X-ray and radio components in the compact steep-spectrum quasar 3C 48. *MNRAS*, 347:632–644.

Wright, E. L., Chen, X., Odegard, N., Bennett, C. L., Hill, R. S., Hinshaw, G., Jarosik, N., Komatsu, E., Nolta, M. R., Page, L., Spergel, D. N., Weiland, J. L., Wollack, E., Dunkley, J., Gold, B., Halpern, M., Kogut, A., Larson, D., Limon, M., Meyer, S. S., and Tucker, G. S. (2009). Five-Year Wilkinson Microwave Anisotropy Probe Observations: Source Catalog. *ApJS*, 180:283–295.

Yu, Q. and Tremaine, S. (2002). Observational constraints on growth of massive black holes. *MNRAS*, 335:965–976.

Zirbel, E. L. (1997). The Megaparsec Environments of Radio Galaxies. *ApJ*, 476:489–+.

Part II

Publications and preprints

2007 G. Migliori, et al. *Radio Lobes of Pictor A: an X-ray spatially resolved study*, 2007, ApJ, 668, 203

2010 A. A. Abdo et al. *Fermi Large Area Telescope Observations of Misaligned Active Galactic Nuclei*, 720, 912A

2010 G. Migliori, A. Siemiginowska & A. Celotti *Broad-band jet emission in young and powerful radio sources: the case of the CSS quasar 3C 186*, 2010, in preparation